

# **THE ROLE OF FLUIDS IN GEOLOGICAL PROCESSES**

by  
Tristan Azbej

Dissertation submitted to the faculty of the Virginia Polytechnic Institute and State  
University in partial fulfillment of the requirements for the degree of  
Doctor of Philosophy in Geosciences

Committee Chairman: Robert J. Bodnar  
Committee: James Beard, Erdogan Kiran, Donald Rimstidt, Csaba Szabo,  
Robert Tracy

August 22nd, 2006  
Blacksburg, Virginia

Key words: critical fluids, laser raman spectrometry, melt inclusions, ocelli

## THE ROLE OF FLUIDS IN GEOLOGICAL PROCESSES

Azbej Tristan

(ABSTRACT)

The role and behavior of fluids in hydrothermal and magmatic environments have been studied. Experimental studies have been carried out to determine fluid properties, in natural environments and in both synthetic and natural fluid and melt inclusions.

One of these studies dealt with the effect of composition on the critical P-T-X properties of aqueous salt solutions approximated by the H<sub>2</sub>O-NaCl-KCl-CaCl<sub>2</sub> system. The results indicate a systematic variation in critical properties as a function of composition over the range of P-T-X studied.

A technique for analyzing individual H<sub>2</sub>O-CO<sub>2</sub> inclusions using Raman spectroscopy has also been developed. The resulting empirical equation relating Raman intensities and composition is valid for compositions  $\leq 50$  mol% CO<sub>2</sub>. The technique has been applied to H<sub>2</sub>O-CO<sub>2</sub> inclusions from the Butte, MT Porphyry Cu-Mo deposit and the results agree with compositions estimated from microthermometric and petrographic observations.

The aim of another study was to study water loss from melt inclusions during laboratory heating. Melt inclusions had lost insignificant amounts of water when held at experimental conditions (800°C, 1 kbar) for  $\leq 24$  hours. However, significant water loss was observed for longer duration experiments.

Ocelli, which are globular bodies of felsic minerals are interpreted as products of magmatic melt immiscibility. As such, the carbonate aggregates in Cretaceous lamprophyres from Hungary with similar petrographic characteristics have also generally been interpreted to be products of magmatic immiscibility. Petrographic and geochemic studies have shown three three distinct genetic groups for these aggregates, none of which were consistent with a magmatic origin.

## Table of contents

### Chapter I – Introduction

I.1 Synthetic fluid inclusions XVII: Critical PTX properties of H <sub>2</sub> O-NaCl-KCl solutions.....	1
I.2 In Situ Quantitative Analysis of Individual H <sub>2</sub> O-CO <sub>2</sub> Fluid Inclusions by Laser Raman Spectroscopy.....	2
I.3 Experimental determination of H <sub>2</sub> O loss from melt inclusions during laboratory heating.....	4
I.4 Genesis of carbonate aggregates in lamprophyres from the northeastern Transdanubian Central Range, Hungary: Magmatic or hydrothermal origin?...5	

### CHAPTER 2. – Synthetic fluid inclusions XVII: PTX properties of H<sub>2</sub>O-NaCl-KCl-CaCl<sub>2</sub> solutions in the vicinity of the critical point

II.1. Introduction.....	7
II.2. Phase Equilibria in Aqueous Salt Solutions.....	8
II.3. Experimental Methods.....	14
II.4. Results and Discussion.....	18
II.5. Summary.....	30
II.6. Acknowledgements.....	30
II.7. References.....	31

### CHAPTER 3. - In Situ Quantitative Analysis of Individual H<sub>2</sub>O-CO<sub>2</sub> Fluid Inclusions by Laser Raman Spectroscopy

III.1. Introduction.....	35
III.2. Analytical Methods.....	36
III.3. Results and Discussion.....	40
III.4. Application to Natural Inclusions.....	48
III.5. Conclusions.....	50
III.6. Acknowledgements.....	51
III.7. References.....	51

CHAPTER IV - Experimental determination of H<sub>2</sub>O loss from melt inclusions during laboratory heating

IV.1. Introduction.....	56
IV.2. Raman Spectra of Hydrous Glass.....	57
IV.3. Calibration of the Raman spectra.....	61
IV.4. Water loss from melt inclusions.....	66
IV.5. Conclusions.....	80
IV.6. Acknowledgements.....	81
IV.7. References Cited.....	81

CHAPTER V. - Genesis of carbonate aggregates in lamprophyres from the northeastern Transdanubian Central Range, Hungary: Magmatic or hydrothermal origin?

V.1. Introduction.....	88
V.2. Geological Background and Lamprophyre Petrology.....	89
V.3. Samples Studied and Analytical Methods.....	92
V.4. Petrography.....	93
V.5. Chemical Composition of Carbonate Aggregates.....	95
V.6. Microthermometric Analyses.....	99
V.7. Discussion.....	103
V.8. Conclusions.....	108
V.9. Acknowledgements.....	110
V.10. References.....	110

## List of Figures

Figure 1.1. Critical points of 2 molal H <sub>2</sub> O-NaCl-KCl-CaCl <sub>2</sub> solutions.	2
Figure 1.2. Raman spectrum.	3
Figure 1.3. Relationship between water content of melt inclusions in quartz from the Bishop Tuff and the amount of time held at 800°C and 1 kbar.	5
Figure 1.4. Estimates of P-T formation conditions for carbonate aggregates in the TCR lamprophyres.	6
Figure 2.1. Schematic phase diagram of H <sub>2</sub> O.	9
Figure 2.2. Schematic phase diagram of H <sub>2</sub> O and the critical curves of the H <sub>2</sub> O-NaCl.	10
Figure 2.3. Schematic segment of the phase diagram H <sub>2</sub> O-NaCl phase diagram.	12
Figure 2.4. Enthalpy – temperature diagram of a pure fluid.	13
Figure 2.5. Determination of critical conditions of a solution using the slope-intercept technique.	16
Figure 2.6. Critical temperature curves of H <sub>2</sub> O-KCl-NaCl solutions.	21
Figure 2.7. Critical pressure curves of H <sub>2</sub> O-KCl-NaCl solutions.	26
Figure 2.8. Critical isochore slopes of H <sub>2</sub> O-KCl-NaCl solutions.	27
Figure 2.9. Critical curves of H <sub>2</sub> O-KCl and H <sub>2</sub> O-NaCl solutions.	28
Figure 2.10. Critical points of 2 molal H <sub>2</sub> O-NaCl-KCl-CaCl <sub>2</sub> solutions.	29
Figure 3.1. Raman spectrum (at 350°C) showing the peaks for CO <sub>2</sub> (1388 cm <sup>-1</sup> ) and H <sub>2</sub> O (3600 cm <sup>-1</sup> ).	39
Figure 3.2. Raman linear peak intensity ratios calculated for different acquisition times.	40
Figure 3.3. Relationship between composition of H <sub>2</sub> O-CO <sub>2</sub> inclusions and Raman spectral intensity ratios.	42
Figure 3.4. Raman linear peak intensity ratios of CO <sub>2</sub> -H <sub>2</sub> O inclusions.	44
Figure 3.5. Raman peak area ratios of CO <sub>2</sub> -H <sub>2</sub> O inclusions.	46
Figure 3.6. Relationship between the mole % CO <sub>2</sub> in H <sub>2</sub> O-CO <sub>2</sub> inclusions and Raman peak area ratios.	48

Figure 4.1. Raman spectrum of alkali feldspar glass.	59
Figure 4.2. Comparison of Raman spectra of a melt inclusion (inset) in quartz.	60
Figure 4.3. Summary of the procedures used to treat Raman spectra obtained on hydrous glasses.	63
Figure 4.4. Relationship between the amount of water in hydrous glass and the ratio between the water peak area at $3550\text{ cm}^{-1}$ and the T-O-T peak area band centered at $1050\text{ cm}^{-1}$ .	64
Figure 4.5. Relationship between water content of melt inclusions in quartz from the Bishop Tuff and the amount of time held at $800^{\circ}\text{C}$ and 1 kbar.	73
Figure 4.6. Relationship between ratio of the bubble area to the total area of the melt inclusion and amount of time the inclusion was held at $800^{\circ}\text{C}$ and 1 kbar.	78
Figure 4.7. Comparison between the single-standard technique used by Thomas et al. (2006) & Di Muro et al. (2006), and the multiple standard calibration technique.	79
Figure 5.1. Geological map of the northeastern Transdanubian Central Range (TCR).	91
Figure 5.2. Photomicrographs (A, C, D, E, H) and BSE images (B, F) of carbonate aggregates in the TCR lamprophyres.	94
Figure 5.3. Ternary CaO–MgO–FeO diagrams showing compositions of carbonate phases in aggregates from the TCR lamprophyres.	96
Figure 5.4. Homogenization temperatures of fluid inclusions hosted in carbonate aggregates.	101
Figure 5.5. Estimates of P-T formation conditions for carbonate aggregates in the TCR lamprophyres.	106

## List of Tables

Table 2.1. Homogenization temperatures of and behavior of synthetic H <sub>2</sub> O–KCl inclusions	19
Table 2.2. Homogenization temperatures of and behavior of synthetic H <sub>2</sub> O–NaCl–KCl inclusions (mNaCl:mKCl = 1:1)	23
Table 2.3. Homogenization temperatures of and behavior of synthetic H <sub>2</sub> O–NaCl–KCl inclusions (mNaCl:mKCl = 3:1 and 1:3)	25
Table 3.1. Raman linear peak intensity ratios of H <sub>2</sub> O–CO <sub>2</sub> synthetic fluid inclusion standards.	42
Table 3.2. Raman spectral linear peak intensity ratios of H <sub>2</sub> O–CO <sub>2</sub> synthetic fluid inclusion standards collected at various temperatures	44
Table 3.3. Raman spectral peak area ratios of H <sub>2</sub> O–CO <sub>2</sub> synthetic fluid inclusion standards collected at various temperatures.	47
Table 3.4. Raman spectral peak area ratios of H <sub>2</sub> O–CO <sub>2</sub> synthetic fluid inclusion standards.	47
Table 3.5. Compositions of H <sub>2</sub> O–CO <sub>2</sub> inclusions from Butte, Montana	49
Table 4.1. Description of Glass Standards used for Raman Calibration	67
Table 4.2. Results of Raman analysis of melt inclusions in early-erupted Bishop Tuff quartz	69
Table 5.1a. Table 1a. Average composition of carbonate minerals in Type-I aggregates from the TCR lamprophyres.	97
Table 5.1b. Table 1b. Average composition of carbonate minerals in Type-II and -III aggregates from the TCR lamprophyres.	98
Table 5.1c. Table 1c. Average composition of carbonate minerals in veins from the TCR lamprophyres.	99
Table 5.2. Average ice-melting temperatures and salinities of fluid inclusions in carbonate aggregates from the TCR lamprophyres.	102
Table 5.3. Summary of petrographic, geochemical and microthermometric characteristics of different carbonate aggregate types in the TCR lamprophyres.	109

## **CHAPTER I. - Introduction**

This dissertation includes, in addition to this introductory chapter, four chapters each describing a different project. The overriding theme that ties all of these studies together is the role and behavior of fluids in hydrothermal and magmatic environments. These projects include experimental studies to determine fluid properties, as well as studies of fluids in both synthetic and natural fluid and melt inclusions.

### **I.1. Critical PTX properties of H<sub>2</sub>O-NaCl-KCl solutions**

Hydrothermal fluids in their critical or near-critical states exhibit anomalous physical and thermodynamic properties that affect mass and energy transport in hydrothermal systems. This project investigated the effect of composition on the critical P-T-X properties of aqueous salt solutions. Fluids approximated by the H<sub>2</sub>O-NaCl-KCl-CaCl<sub>2</sub> system are common in many geologic environments including submarine hydrothermal environments and other hydrothermal ore-forming systems. In this study, P-T location of the critical point and the projection of the critical isochore have been determined for various compositions in the H<sub>2</sub>O-NaCl-KCl-CaCl<sub>2</sub> system, for salinities  $\leq 3$  molal. The results indicate a systematic variation in critical properties as a function of composition over the range of P-T-X studied (Fig 1.1.).

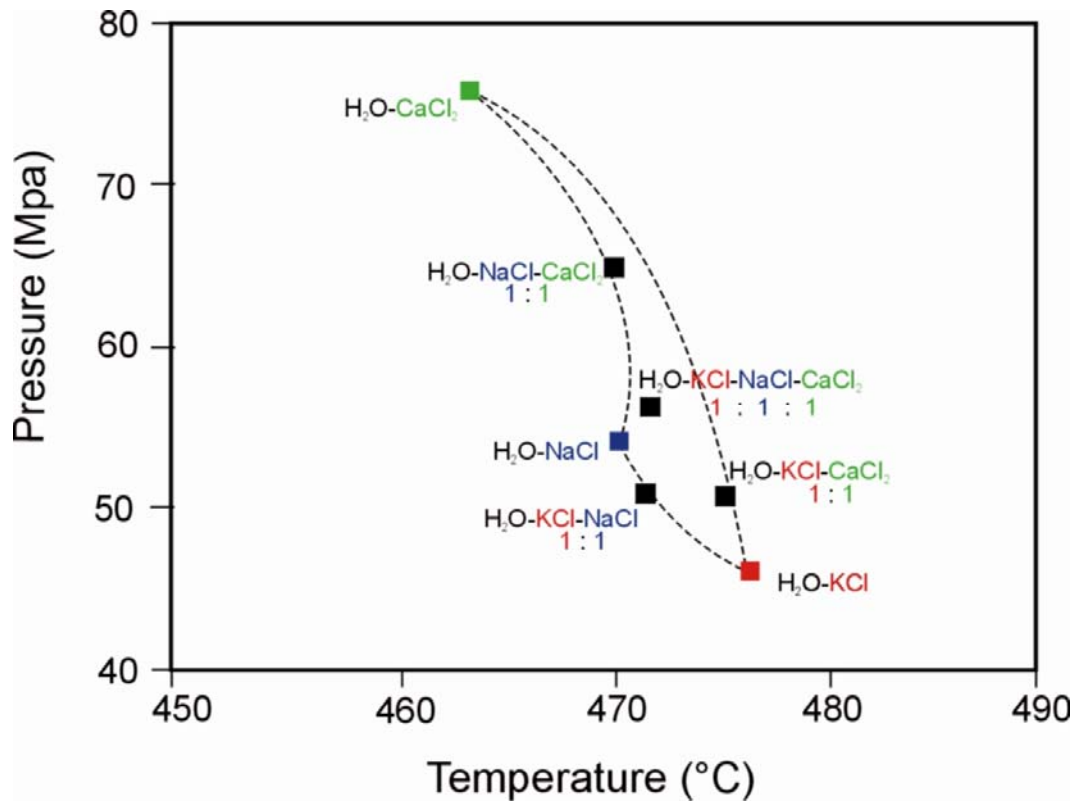


Figure 1.1. Critical points of 2 molal H<sub>2</sub>O-NaCl-KCl-CaCl<sub>2</sub> solutions. Dashed lines represent projected mixing curves between the binary end-member solutions. Ratios represent the molar ratio of solutes in ternary and quaternary solutions.

## I.2. In Situ Quantitative Analysis of Individual H<sub>2</sub>O-CO<sub>2</sub> Fluid Inclusions by Laser Raman Spectroscopy

Fluids approximated by the H<sub>2</sub>O-CO<sub>2</sub>±salt system are common in hydrothermal ore deposits and in medium- to high-grade metamorphic rocks. Interpretation of fluid inclusions from these environments requires information on the H<sub>2</sub>O-CO<sub>2</sub> ratio of the fluids because the isochores and metamorphic phase equilibria vary with fluid composition. In this study a technique for analyzing individual H<sub>2</sub>O-CO<sub>2</sub> inclusions using Raman spectroscopy is described (Fig. 1.2.). This technique eliminates the need to know the geometry of the inclusions and the host sample as required for quantitative FTIR analysis and allows much smaller inclusions to be analyzed. The resulting empirical equation relating Raman intensities and composition is valid for compositions

$\leq 50\text{mol}\%$   $\text{CO}_2$ . The technique has been applied to  $\text{H}_2\text{O}-\text{CO}_2$  inclusions from the Butte, MT Porphyry Cu-Mo deposit and the results agree with compositions estimated from microthermometric and petrographic observations.

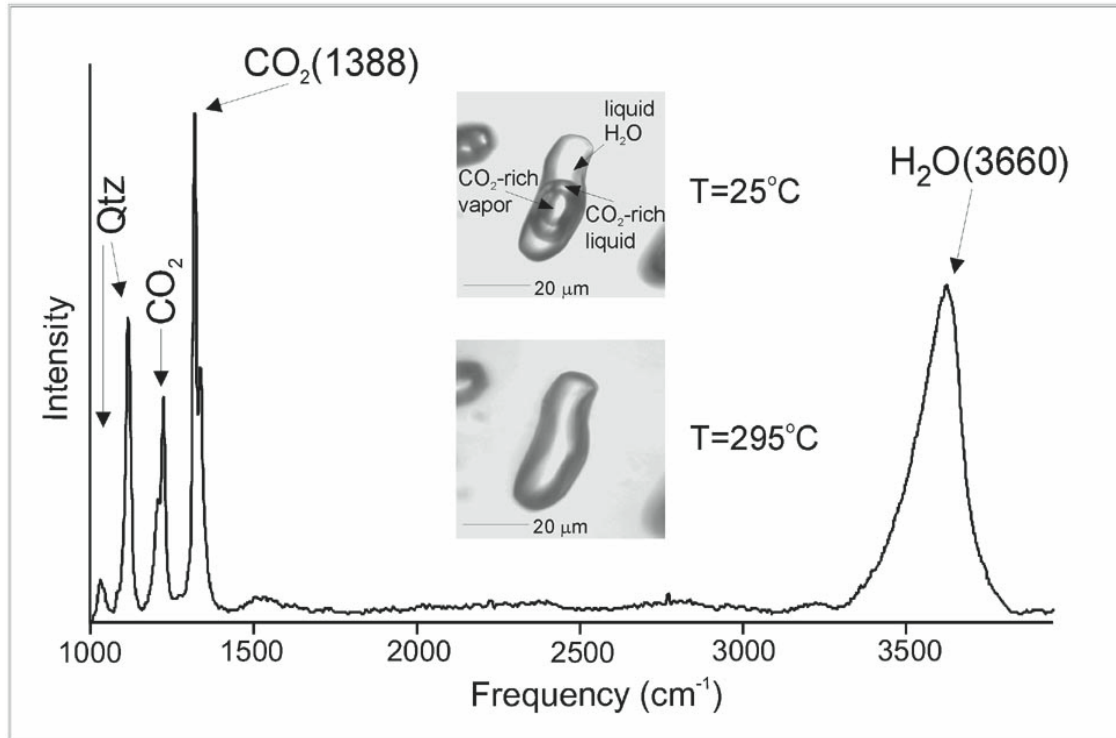


Figure 1.2. Raman spectrum (at  $350^\circ\text{C}$ ) showing the peaks for  $\text{CO}_2$  ( $1388\text{ cm}^{-1}$ ) and  $\text{H}_2\text{O}$  ( $3600\text{ cm}^{-1}$ ) that were used for calibration, as well as the lower member of the  $\text{CO}_2$  Fermi diad (labeled  $\text{CO}_2$ ) the bending mode of  $\text{H}_2\text{O}$  ( $1594\text{ cm}^{-1}$ ) and two quartz peaks (labeled Qtz). The photomicrograph shows an  $\text{H}_2\text{O}-\text{CO}_2$  inclusion containing 25 mole %  $\text{CO}_2$  at  $25^\circ\text{C}$  and at the homogenization temperature ( $295^\circ\text{C}$ ).

### **I.3. Experimental determination of H<sub>2</sub>O loss from melt inclusions during laboratory heating**

The volatile contents of magmas affect crystallization behavior and eruption dynamics in volcanic systems. A common source of information on the volatile content of magmas is melt inclusions trapped in igneous phenocrysts. Often melt inclusions are partially to completely crystallized as found, and must be reheated in the laboratory before they can be analyzed by Raman spectroscopy or Secondary Ion Mass Spectrometry to determine the water content. There has been considerable discussion in the literature concerning the effect of heating on the water content of the melt inclusions, and some have suggested that water diffuses out of the inclusions during heating. The goal of this study was to investigate the loss of water from melt inclusions during laboratory heating. The first step was to develop an empirical relationship between Raman peak intensities and water content using synthetic glasses with known water contents. Then, melt inclusions with known water content hosted in quartz crystals from the Bishop Tuff Rhyolite Formation were heated to 800°C, 1 kbar for periods of time ranging between 4 hours and 63 days. The results showed that melt inclusions had lost insignificant amounts of water when held at experimental conditions  $\leq 24$  hours (Fig. 1.3.). However, significant water loss was observed for longer duration experiments.

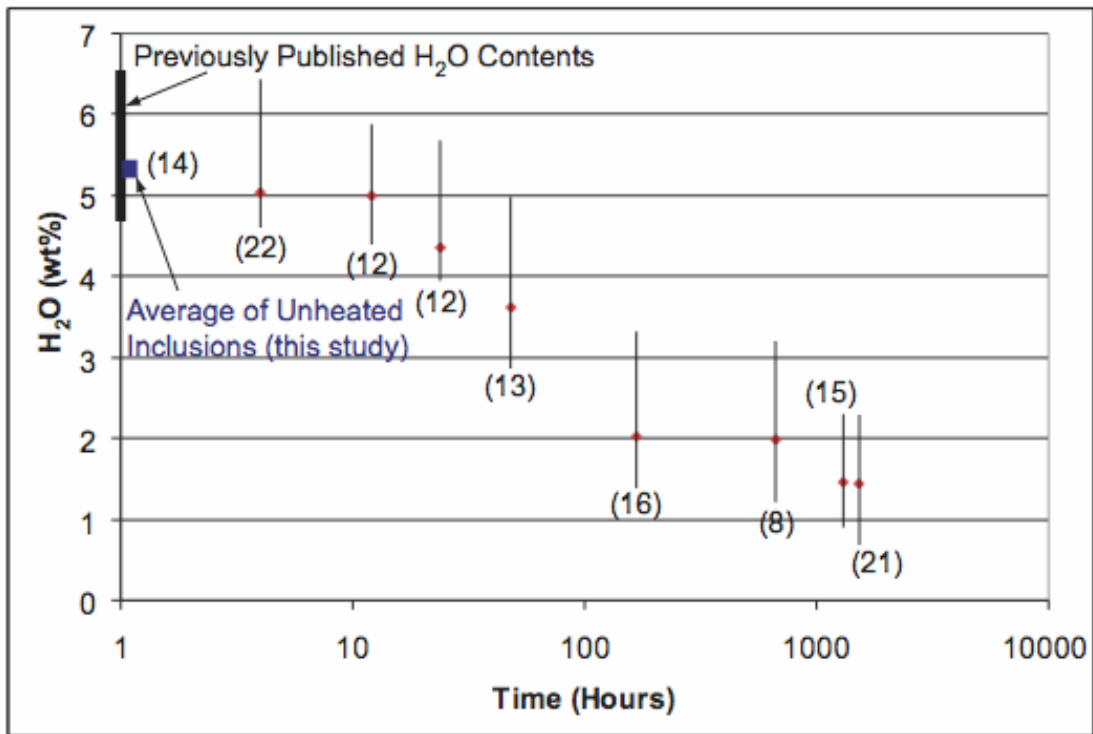


Figure 1.3. Relationship between water content of melt inclusions in quartz from the Bishop Tuff and the amount of time held at 800°C and 1 kbar. Each point represents the average of at least 10 measurements in a sample set and the bars surrounding it reach the minimum and maximum values measured in that set.

#### **I.4. Genesis of carbonate aggregates in lamprophyres from the northeastern Transdanubian Central Range, Hungary: Magmatic or hydrothermal origin?**

Lamprophyres are alkaline, mafic, igneous rocks that form in extensional tectonic environments. These rocks sometimes contain up to a few weight percent of carbonate minerals that appear to be similar to ocelli, which are globular bodies of felsic minerals that are products of magmatic melt immiscibility. As such, the carbonate aggregates have also generally been interpreted to be products of magmatic immiscibility. In this study carbonate aggregates in Cretaceous lamprophyre dike rocks that are intruded into the ALPACA (ALpine-PAnnonian-CARpathian) tectonic block (Western Hungary) were examined (Fig 1.4.). Using petrography, microthermometry, major element composition,

cathodoluminescence microscopy and thermobarometric calculations, we distinguished three genetic groups for these aggregates, none of which were consistent with a magmatic origin. Results of fluid inclusion and other geochemical studies are consistent with a subsolidus hydrothermal origin for the carbonate aggregates in the lamprophyres (Fig 1.4.).

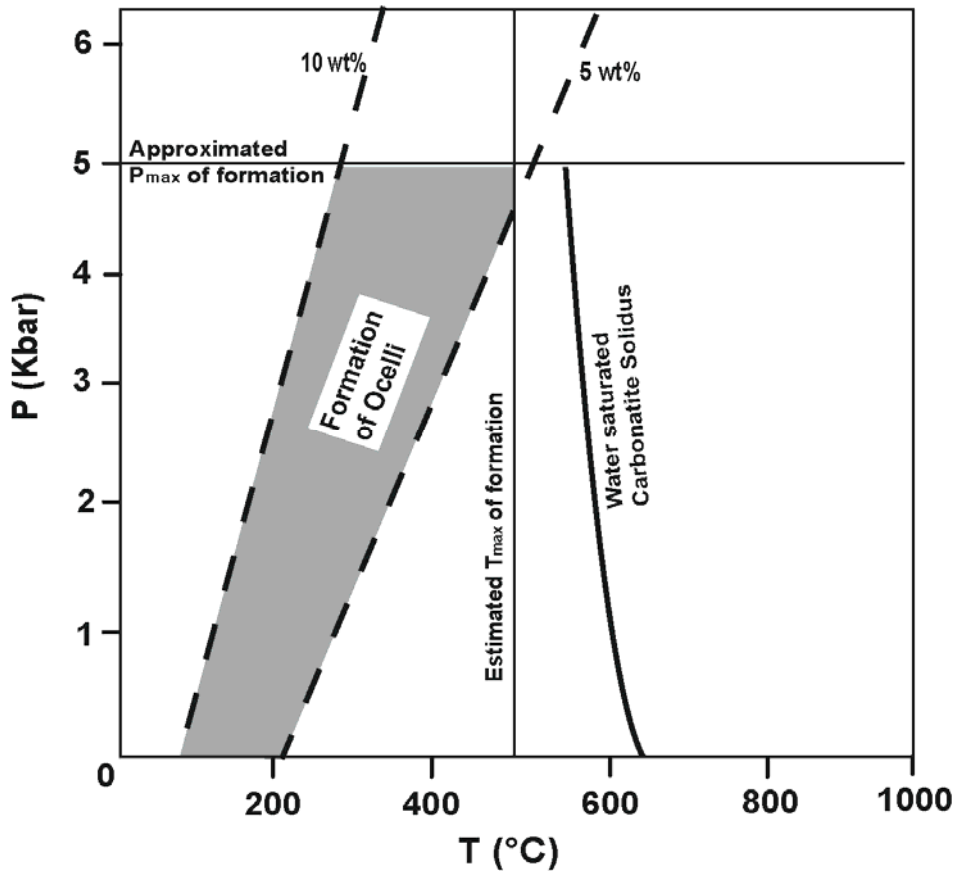


Figure 1.4. Estimates of P-T formation conditions for carbonate aggregates in the TCR lamprophyres. The shaded field shows the pressure-temperature field for formation of Type-I carbonate aggregates, defined by the isochores (dashed lines) for lowest and highest measured homogenization temperatures and lowest and highest calculated salinity. The vertical solid line shows the estimated maximum temperature of formation and the horizontal line shows the assumed maximum pressure of formation. Also shown the water-saturated carbonatite solidus from Boettcher et al. (1980).

## **CHAPTER 2. PTX properties of H<sub>2</sub>O-NaCl-KCl-CaCl<sub>2</sub> solutions in the vicinity of the critical point**

### **II.1. Introduction**

The physical, thermodynamic and transport properties of H<sub>2</sub>O and aqueous solutions vary systematically with changing temperature and pressure and affect the ability of aqueous fluids to transfer mass and heat in hydrothermal environments (Bodnar and Costain, 1991). Over most of crustal P-T space, fluid properties such as density, heat capacity, viscosity, etc., change relatively little in response to small to moderate temperature and/or pressure fluctuations. However, in the vicinity of the critical point, relatively small changes in temperature and/or pressure can significantly affect fluid properties and the ability of fluids to transfer mass and energy (Johnson and Norton, 1991). For example, studies have shown that temperatures at submarine black smokers are often within fifty degrees Celsius of the critical temperature for the corresponding fluid composition (Von Damm et al. 1992; Baker, 1995). Similarly, various models and observations at seafloor vents suggest that hydrothermal fluids attain fluid flow and convective thermal energy transfer maxima in these near-critical fluids (e.g., Bischoff and Rosenbauer, 1985; Baker, 1995; Jupp and Schultz, 2000). The unique properties of supercritical fluids have also led to their application as high efficiency solvents for contaminant removal in industrial processes because critical and near-critical aqueous fluids behave as "nonaqueous solvents" and have the ability to dissolve many nonpolar organic compounds (e.g., Tester et al., 1993; Savage et al., 1995). Such fluids are also miscible with O<sub>2</sub> and provide an excellent medium for toxic waste oxidation to produce harmless molecules (such as CO<sub>2</sub> and N<sub>2</sub>) that can be segregated and collected through fluid-phase separation upon cooling (e.g., Tester et al., 1993; Savage et al., 1995; Brunner et al., 2001; Savage and Oh, 2001).

In order to better understand the evolution of hydrothermal systems and to further develop industrial applications of supercritical fluids requires information on the physical and chemical properties of aqueous fluids in the vicinity of the critical point. More specifically, many fluid inclusions are trapped in hydrothermal environments at near-

critical conditions and our ability to interpret microthermometric data from these inclusions is limited by the paucity of data in the vicinity of the critical point. A first step in this process is to determine the P-T location of the critical point as a function of composition. The critical point of pure H<sub>2</sub>O is well-constrained experimentally (IAPWS, 1991), and the critical points of some simple two-component aqueous systems over a limited range of composition have been determined (Sourirajan and Kennedy, 1962; Khaibullin and Borisov, 1966; Potter et al., 1976; Bodnar et al., 1985; Knight and Bodnar, 1989; Oakes et al., 1994). However, studies to determine the critical points of more complex multi-component compositions similar to those that occur in nature are rare, thus limiting our ability to interpret fluid inclusions that contain such fluids. In this paper we describe results of an experimental study to determine the P-T location of the critical points of low to moderate salinity fluids in the H<sub>2</sub>O-NaCl-KCl-CaCl<sub>2</sub> system as well as the P-T location of the critical isochore for these compositions.

## II.2. Phase Equilibria in Aqueous Salt Solutions

Phase relations of the one component system H<sub>2</sub>O are shown schematically in Figure 2.1. The Gibbs' Phase Rule defines the number of phases that can coexist in equilibrium for a given number of components in a closed system according to:

$$F = C - P + 2 \quad (2.1)$$

where  $C$  represents the number of components,  $P$  is the number of phases and  $F$  represents the number of degrees of freedom. Thus, in the one-component pure H<sub>2</sub>O system three phases coexist in equilibrium at a point (zero degrees of freedom), two phases coexist along a line (one degree of freedom) and one phase exists in an area (two degrees of freedom).

Of particular interest here is the two-phase (liquid + vapor) coexistence curve that extends from the triple point (TP; Fig. 2.1.; T= 0.01°C, P=611.657 Pa) to the critical point (CP; Fig. 2.1.; T=374.1°C, P=22.064 MPa) (IAPWS, 1991). With increasing

temperature along the liquid + vapor curve, the density of the liquid phase decreases and the density of the vapor phase increases until they become identical at the critical point. Thus, the critical point is defined as the temperature and pressure, at which the properties of the liquid and vapor phases become identical, i.e., there is no distinction between liquid and vapor. In a one-component system such as H<sub>2</sub>O, the critical point represents a critical endpoint – two phases may not coexist in equilibrium at temperatures above the critical endpoint. In a one-component system, fluids at temperatures above the critical temperature are referred to as supercritical fluids (Fig. 2.1.).

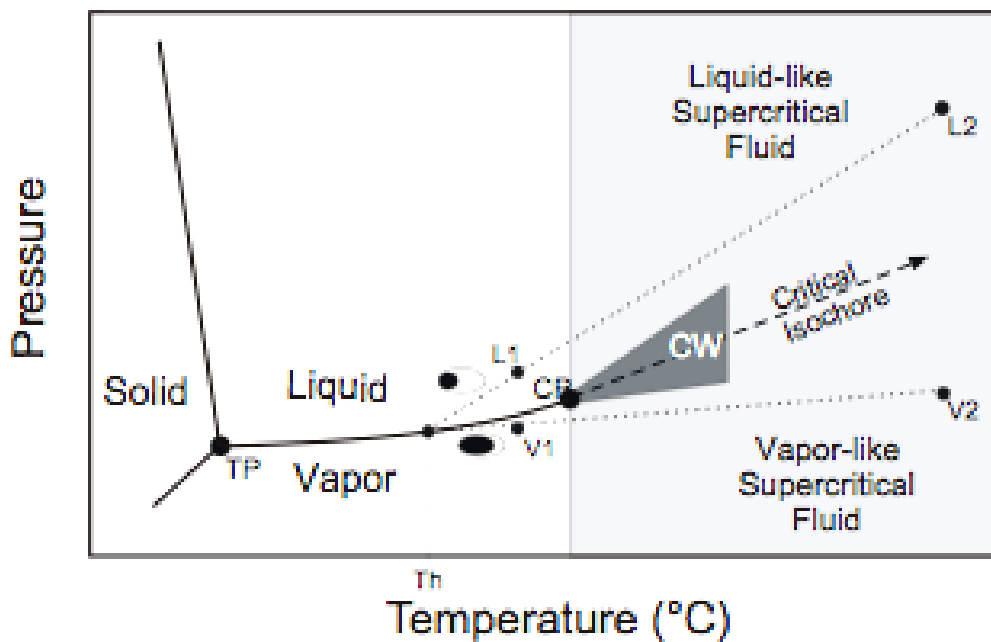


Figure 2.1. Schematic phase diagram of H<sub>2</sub>O. Light grey area represent the supercritical P-T conditions; CW and dark grey area represents the critical wedge. TP is the triple point and CP is the critical point. Dotted lines are isochores that originate from one common point on the liquid-vapor boundary ( $T_h$ ) but reflect vapor (V1, V2) and liquid (L1, L2) densities. H<sub>2</sub>O inclusions that homogenize at  $T_h$  by the disappearance of the vapor phase could have trapped a liquid (L1), a supercritical 'liquid' (L2). Fluid inclusions that homogenize to the vapor phase could have formed in the vapor field (V1) or the supercritical 'vapor' field (V2).

The addition of a second component to the pure H<sub>2</sub>O system affects the topology and phase relations in a predictable manner. Thus, the addition of CO<sub>2</sub> causes the critical curve to move to lower temperatures and higher pressures, whereas the addition of NaCl causes the critical curve to migrate to higher temperatures and only slightly higher

pressures (Fig. 2.2.). According to the Gibb's Phase Rule, four phases now coexist in equilibrium at a point (zero degrees of freedom), three phases coexist along a line (one degree of freedom), two phases coexist in an area (two degrees of freedom), and one phase exists in a volume (three degrees of freedom).

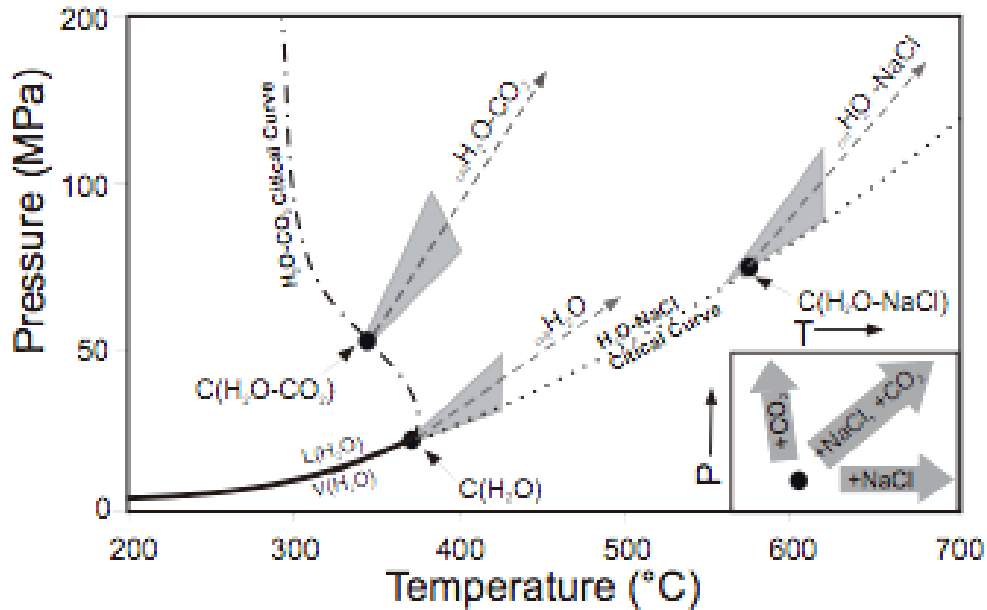


Figure 2.2. Schematic phase diagram of  $\text{H}_2\text{O}$  and the critical curves of the  $\text{H}_2\text{O}$ - $\text{NaCl}$  (dotted line) and of the  $\text{H}_2\text{O}$ - $\text{CO}_2$  systems (dotted/dashed line). Solid line represents the liquid-vapor boundary of pure  $\text{H}_2\text{O}$ . Dashed arrows are critical isochores and grey areas are critical wedges. C refers to a specific critical point on the critical curves. Insert shows that general direction of critical point in P-T space for different solutes constituents in aqueous solutions.

Abundant experimental data and theoretical models describing the critical PVTX properties of aqueous salt solutions have been published. The best-characterized two-component system is  $\text{H}_2\text{O}$ - $\text{NaCl}$  (Sourirajan and Kennedy, 1962; Marshall and Jones, 1974; Urusova 1974; Pitzer, 1984; Bischoff et al., 1986; Bodnar et al., 1985; Knight and Bodnar, 1989; Tanger and Pitzer, 1989 Anderko and Pitzer 1993a; Shmulovich et al, 1995; Povodyrev et al, 1999; Driesner and Heinrich, 2002). Experimental data and theoretical models are in good agreement on the general topology of the critical curve of  $\text{NaCl}$ - $\text{H}_2\text{O}$  solutions; however, significant differences in critical pressures and smaller differences in critical temperatures have been observed above 2.5 molal (Driesner and

Heinrich, 2002). Critical pressures of H<sub>2</sub>O-NaCl solutions >2.5 molal measured by Knight and Bodnar (1989) and correlated by Povodyrev et al. (1999) are significantly lower than other experimental data (Sourirajan and Kennedy, 1962; Shmulovich et al., 1995) and theoretical calculations (Tanger and Pitzer, 1989). Critical properties of dilute H<sub>2</sub>O-KCl solutions (Khaibullin and Borisov, 1966; Potter et al., 1976) and of H<sub>2</sub>O-CaCl<sub>2</sub> solutions up to 3 molal have also been determined (Oakes et al., 1994).

We use the schematic H<sub>2</sub>O-NaCl phase diagram after Bodnar and co-workers (1985) to describe the high pressure and temperature phase behavior of a two-component H<sub>2</sub>O-salt system (Fig. 2.3.). The H<sub>2</sub>O-NaCl system also serves as a good model for the general topology of phase relations of other alkali metal and alkaline earth metal chlorides (Valyashko, 2004). Figure 3 is a pressure – temperature projection of a three-dimensional pressure – temperature – composition (P-T-X) diagram. Addition of NaCl to H<sub>2</sub>O results in the migration of the critical point from the critical point of H<sub>2</sub>O (C<sub>H<sub>2</sub>O</sub>; Fig. 2.3.) to higher temperatures and slightly higher pressures (Fig. 2.3.). The critical curve reaches a maximum pressure at some as yet undetermined temperature and salinity (Fig. 2.3.). The critical pressure then decreases with further increase in salinity until the critical point of pure NaCl is reached (C<sub>NaCl</sub>; Fig. 2.3.). Unlike one-component systems in which the critical point represents the end of a liquid + vapor coexistence curve, the critical point in a two-component system such as H<sub>2</sub>O-NaCl represents a point on a continuous phase boundary defined as the liquid-vapor (or dew-point – bubble-point) curve. Thus, a moderate salinity solution has a critical point (C<sub>1H<sub>2</sub>O-NaCl</sub>; Fig. 2.3.) along the phase boundary that separates the one-phase region from the two-phase liquid + vapor region (L+V; Fig. 2.3.). Similarly, a higher salinity composition will have its critical point further along the locus of critical points (C<sub>2H<sub>2</sub>O-NaCl</sub>; Fig. 2.3.).

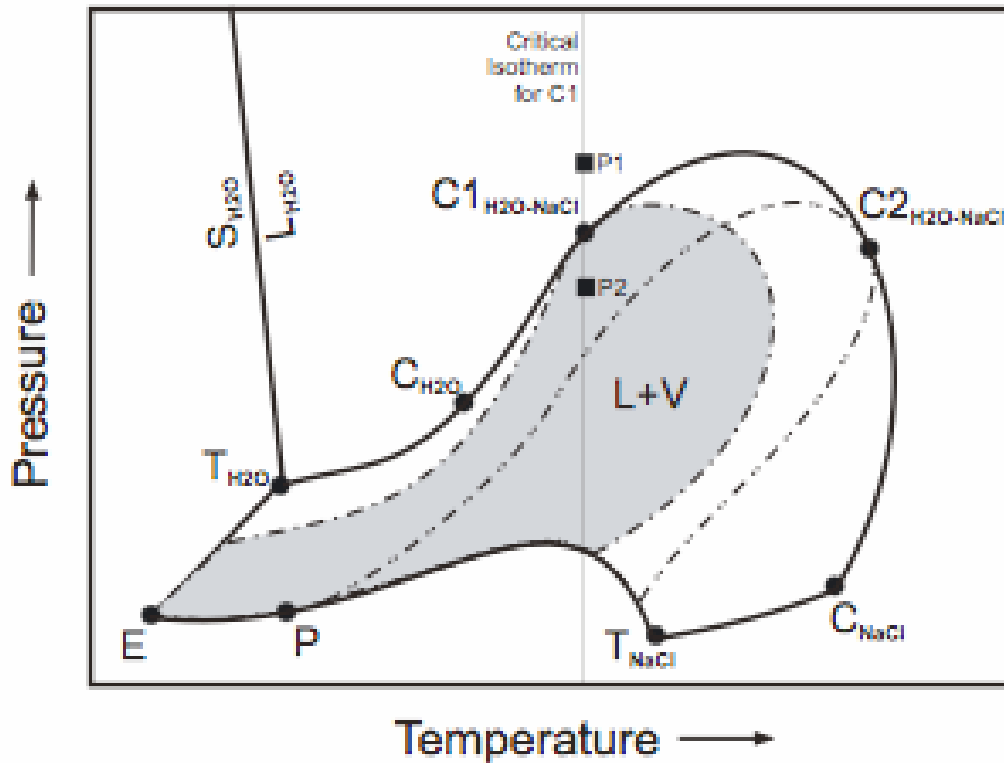


Figure 2.3. Schematic segment of the phase diagram H<sub>2</sub>O-NaCl phase diagram. T represents triple points, C the critical points, E the eutectic point and P the peritectic point. Dotted/dashed lines border the fields of immiscibility for C1 and C2 compositions. P1 represents the formation conditions of a fluid inclusion formed in the single (liquid) phase field, and P2 represents the formation conditions of a fluid inclusion formed in the two-phase field at C1 composition.

As noted above, critical and near-critical fluids exhibit anomalous physical and chemical properties. Such anomalies reflect the fact that several thermodynamic functions and their higher order derivatives diverge to reach extrema at criticality (e.g. Johnson and Norton, 1991; Levelt Sengers, 1994; Levelt Sengers, 1998). One representative example of anomalous behavior in the vicinity of the critical point is enthalpy. The temperature derivative of enthalpy is zero along the critical isobar ( $(\partial H / \partial T)_P = 0$ ) (Pc on Fig. 2.4.). As a result the isobaric heat capacity approaches infinity at the critical point. Thermodynamic relationships also require that at critical conditions, isothermal expansivity, compressibility, and diffusivity are at their maxima while the viscosity: density ratio and the Born coefficients reach their minimum values (e.g.

Gammon, 1987; Johnson and Norton, 1991; Levelt Sengers, 1994; Levelt Sengers, 1998). Anomalous fluid behavior is most evident along the critical isochore within a few tens of degrees of the critical temperature. This region is referred to as the *critical wedge* (Figs. 2.1., 2.2.). Within this region, the mass and energy transport properties of fluids can change by a large amount with small variations in pressure and temperatures (e.g. Bodnar and Costain, 1991; Johnson and Norton, 1991).

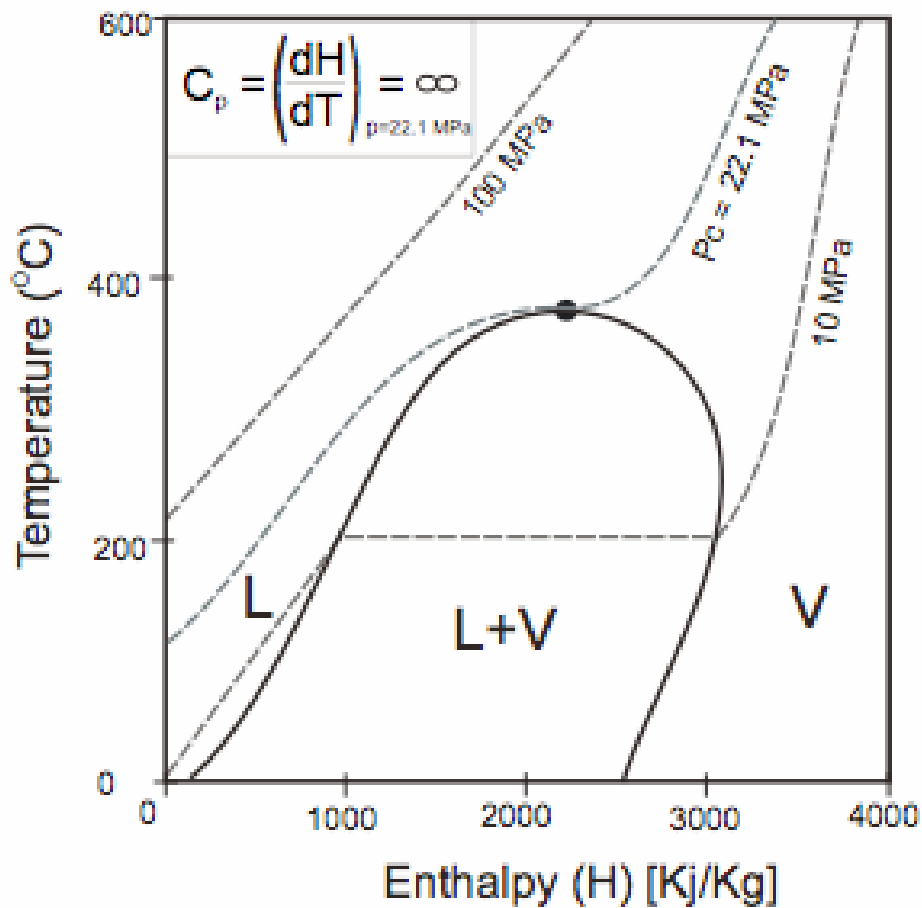


Figure 2.4. Enthalpy – temperature diagram of a pure fluid. On the diagram a subcritical-, a critical- ( $P_c$ ), and a supercritical isobar is plotted. Black dot represents the critical point. Insert shows equation for the critical isobaric heat capacity of the fluid.

### II.3. Experimental Methods

Synthetic fluid inclusions were produced following techniques described by Sterner and Bodnar (1984) and Bodnar and Sterner (1987). A series of experiments were conducted to identify P-T formation conditions that result in homogenization of fluid inclusions by critical behavior as described by Knight and Bodnar (1989). Thermally-fractured Brazilian quartz prisms and 60 to 120 $\mu$ l salt solution of known composition were loaded into platinum capsules. After the capsules were sealed and weighed, the capsules were heated to 120°C in a vacuum oven and then re-weighed to check for leaks. The capsules are then placed into cold-seal pressure vessels. Run durations were typically between four and ten days, depending on the experimental conditions: longer runs were needed for those experiments at lower pressure and temperature to produce usable fluid inclusions. Formation pressure is assumed to be accurate to  $\pm 25$  bars, and temperatures to  $\pm 2$  degrees Celsius. These values were confirmed by trapping pure H<sub>2</sub>O inclusions at the same P-T conditions that H<sub>2</sub>O-salt inclusions were trapped at, and interpreted using the equation of state for H<sub>2</sub>O of Haar et al. (1984).

During the runs, fractures in the quartz prisms are healed, entrapping droplets of fluids to form inclusions. Samples were quenched and depressurized at the end of the experiments and the vessels were removed from the furnaces. Capsules were examined and weighed after cleaning to check for leakage or rupture during the runs. Quartz prisms were then sliced to 1mm thick chips and polished for petrographic and microthermometric analyses. Microthermometric data were obtained using Linkam 600 and 1500°C heating/freezing stages mounted on an Olympus petrographic microscope and with a Fluid Inc. USGS-type gas flow heating/freezing stage mounted on a Leitz petrographic microscope. All stages were calibrated using synthetic fluid inclusion standards.

To determine the critical temperature, fluid inclusions were trapped along an isobar over a range of temperatures (Fig. 2.5.). The inclusions were heated in a fluid inclusion stage to determine the mode and temperature of homogenization. During heating some inclusions homogenize to the liquid phase (Fig. 2.5A), others to the vapor phase (Fig. 2.5B) and some by critical behavior (Fig. 2.5C). Critical homogenization

occurs when the meniscus between the liquid and vapor phases gradually fades and disappears, without expansion or shrinking of the vapor bubble. Homogenization to the liquid phase indicates that the trapping temperature was in the liquid field, i.e., at a temperature *below* the temperature on the critical isochore along the studied isobar. Similarly, homogenization to the vapor phase indicates that the trapping temperature was in the vapor field, i.e., at a temperature *above* the temperature on the critical isochore along the studied isobar. The maximum formation temperature at which inclusions that homogenize to the liquid phase were trapped, and the minimum formation temperature at which inclusions that homogenize to the vapor phase were trapped bracket the temperature of the critical isochore on the isobar. Generally, a second set of experiments was required using smaller formation temperature increments to produce inclusions that homogenized by critical behavior (Fig. 2.5.). The critical temperature is defined as the homogenization temperature of fluid inclusions that homogenize by critical behavior, and this temperature must lie on the critical isochore. The pressure and temperature at which the inclusion was synthesized also defines a point on the critical isochore. To determine the slope of the isochore, this same procedure was repeated along a second isobar to determine a second point on the critical isochore. A straight line connecting these two pressures and temperatures of formation and extrapolated to the measured critical temperature defines the critical pressure (Fig. 2.5.).

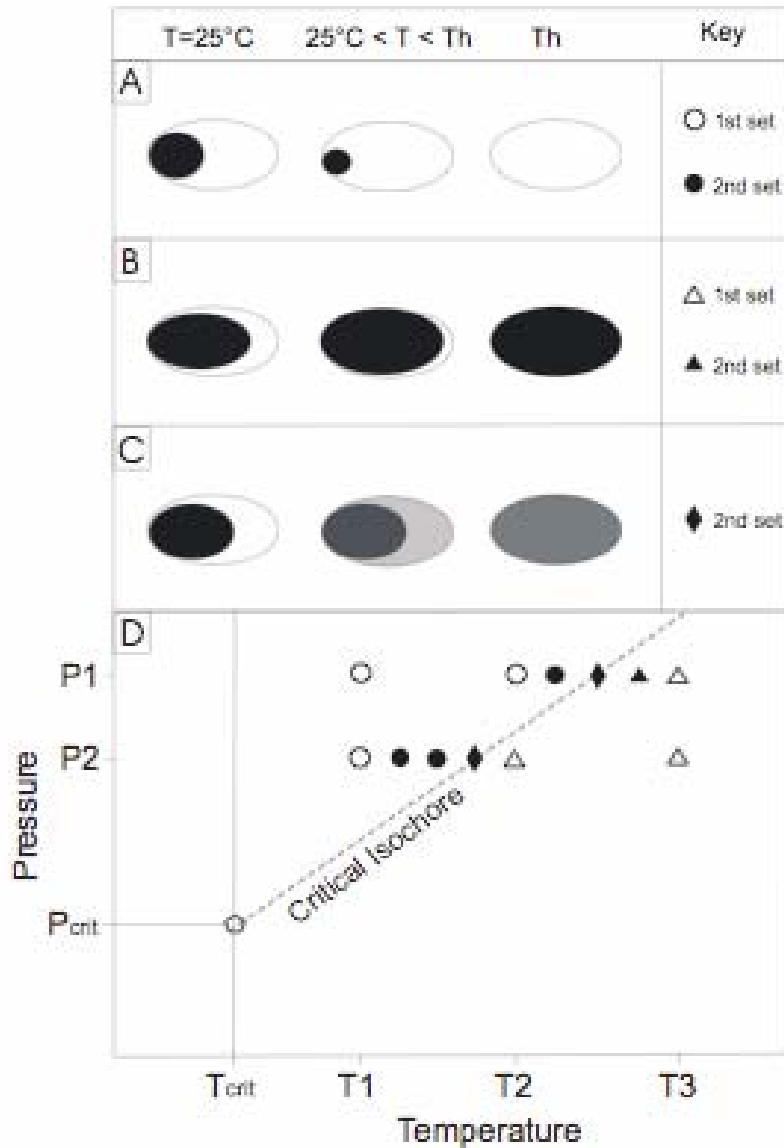


Figure 2.5. Determination of critical conditions of a solution using the slope-intercept technique. First set of experiments is shown by empty symbols; circles represent inclusions homogenized to the liquid phase, triangles represent inclusions homogenized the vapor phase. Second set of experiments is shown by full symbols; dots represent inclusions homogenized to the liquid phase, triangles represent inclusions homogenized the vapor phase, diamonds represent inclusions homogenized by critical behavior.  $T_1$  through  $T_3$  are the experimental (formation) temperatures of the first set,  $P_1$  to  $P_2$  are the experimental pressures. A-C) Drawings of inclusion homogenizing to the liquid, vapor phase and by criticality (respectively through A to C). Dark parts represent the vapor field, light parts represent the liquid phase. D) Pressure-temperature plot of a critical isochore for sample solution. The pentagon represents the critical point;  $T_{\text{crit}}$  is the critical temperature,  $P_{\text{crit}}$  is the critical pressure.

Critical pressures estimated from the slope-intercept technique described above were confirmed with a different series of experiments. Once the critical temperature was determined (following the procedure described above) fluid inclusions are synthesized along the critical isotherm and over a range of pressures (Fig. 2.3.). Phase relations of salt solutions require that, since the critical point falls on the one-phase field – two-phase field boundary, fluid inclusions trapped at the critical temperature and pressures greater than the critical pressure (P1; Fig. 2.3.) are in the one-phase field, while those trapped at pressures less than the critical pressure (P2; Fig. 2.3.) are in the two-phase (liquid + vapor) field. Fluid inclusions trapped in the two-phase field (P2; Fig. 2.3.) show a bimodal distribution of phase relations when observed at room temperature, with liquid-rich inclusions and vapor-rich inclusions. These inclusions may also show a wide range in homogenization temperatures if they trapped mixtures of liquid and vapor (Bodnar et al., 1985). In contrast, inclusions trapped in the one-phase field (P1; Fig. 2.3.) exhibit uniform phase relations and homogenization behavior throughout an individual sample. As with experiments along isobars described earlier, repeating the experiment at smaller pressure increments along the isotherm leads to the generation of fluid inclusions that homogenize by critical behavior. The formation pressure of these inclusions should be identical (within experimental error) to the critical pressures estimated by the extrapolation of the critical isochore to the critical temperature. Fluid compositions were determined from freezing point depressions to confirm that the inclusions were trapped in the one-phase field using the computer program SALTYP developed by Bodnar and coworkers (1989).

## II.4. Results and Discussion

Synthetic inclusions from 120 experiments have been analyzed. One to three quartz chips were examined from every sample; on average five microthermometric measurements were carried out on every chip. Results from this study were combined with data from the literature to estimate the critical curves for H<sub>2</sub>O-KCl and for H<sub>2</sub>O-NaCl-KCl solutions (1:1 atomic molal ratio) up to 3 molal. Additionally, the critical temperature and pressure for 3 molal H<sub>2</sub>O-NaCl-KCl solutions (with 1:3 and 3:1 atomic molal ratios of solutes) and for 2 molal H<sub>2</sub>O-NaCl-KCl-CaCl<sub>2</sub> solutions (with 1:0:1, 0:1:1 and 1:1:1 atomic molal ratios of solutes) were determined. No experiments were conducted for concentrations less than 1.5 molal because previous studies showed that critical temperatures of low salinity H<sub>2</sub>O-KCl solutions were very similar to H<sub>2</sub>O-NaCl solutions of the same salinity (e.g. Khaibullin and Borisov, 1966; Knight and Bodnar, 1989). These differences were too small to be resolved using the synthetic fluid inclusion technique. Therefore, previously published data have been combined with our results to describe the low salinity (<1.5 molal) segments of the critical curves.

Table 2.1. Homogenization temperatures of and behavior of synthetic H<sub>2</sub>O–KCl inclusions.

Sample	Composition (molal)	Tform (°C)	Pform (°C)	Thom (°C)	Homogenization Behavior
011806-VI	1.5	1000	550	412	L
011806-VII	1.5	1000	570	422	L
011806-VIII	1.5	1000	590	428	L
050106-IV	1.5	1000	610	451	Cr
031606-I	1.5	1000	615	454	V>Cr
031606-II	1.5	1000	625	478	V
011806-IX	1.5	1150	590	414	L
011806-X	1.5	1150	615	425	L
031606-III	1.5	1150	645	430	L
050106-II	1.5	1150	660	453	V>Cr
112504-VI	2.0	1100	625	446	L
032105-I	2.0	1100	632	478	Cr
020805-I	2.0	1100	640	490	V
020805-II	2.0	1100	660	528	V
112504-VII	2.0	1200	650	430	L
051506-VI	2.0	1200	664	489	V
032105-II	2.0	1250	670	473	L
020805-XII	2.0	1250	685	492	V
041406-IV	2.0	1250	687	502	V
050603-I	2.0	1250	690	513	V
120204-X	2.0	1300	690	476	Cr>L
050605-III	2.5	1100	630	495	Cr
032105-IV	2.5	1100	645	500	V>Cr
050605-II	2.5	1250	680	495	Cr>V
032105-V	2.5	1250	690	563	V
010106-IX	3.0	1000	605	498	L
010106-VIII	3.0	1000	615	508	L
010106-X	3.0	1000	625	521	L
032506-IV	3.0	1000	640	553	V
110904-I	3.0	1100	600	470	L
110904-II	3.0	1100	650	525	L
112504-I	3.0	1100	655	548	Cr>L
050605-IV	3.0	1100	660	552	Cr
112504-II	3.0	1100	665	577	V
032105-III	3.0	1100	670	579	V
110904-III	3.0	1100	675	600	V
110904-V	3.0	1200	675	533	L
112504-IV	3.0	1250	735	>600	V
010105-V	3.0	1300	715	571	V

In dilute (<2 molal) H<sub>2</sub>O-KCl-NaCl solutions, the  $m_{\text{KCl}}/m_{\text{NaCl}}$  ratio has a negligible effect on the critical temperature (Fig 2.6.). The  $m_{\text{KCl}}/m_{\text{NaCl}}$  ratio becomes increasingly important at higher concentrations: the critical temperature of a 3 molal H<sub>2</sub>O-KCl solution is 42 degrees Celsius higher (552°C vs. 510°C) than that of an H<sub>2</sub>O-NaCl solution of the same salinity, and the critical temperature increases systematically with increasing  $m_{\text{KCl}}/m_{\text{NaCl}}$  ratio (Fig. 2.6.; Table 1). According to Knight and Bodnar (1989) the critical temperature of H<sub>2</sub>O-NaCl solutions as a function of composition is described by the empirical polynomial:

$$T_{\text{crit}} = 374.1 + 53.671\varphi - 2.265\varphi^2 - 0.1739\varphi^3 \quad (2.2)$$

Where  $T_{\text{crit}}$  is the critical temperature in Celsius degrees, and  $\varphi$  is the molal concentration of the salt. Critical temperatures of H<sub>2</sub>O-KCl solutions determined in this study are described by the relationship:

$$T_{\text{crit}} = 374.1 + 82.532\varphi - 33.656\varphi^2 + 8.6608\varphi^3 \quad (2.3)$$

Data included in the regression analysis for Equation (2.3) include those of Khaibullin and Borisov (1966) for dilute solutions ( $\varphi \leq 1$ ) and data from the present study for more saline solutions ( $1.5 \leq \varphi \leq 3$ ).

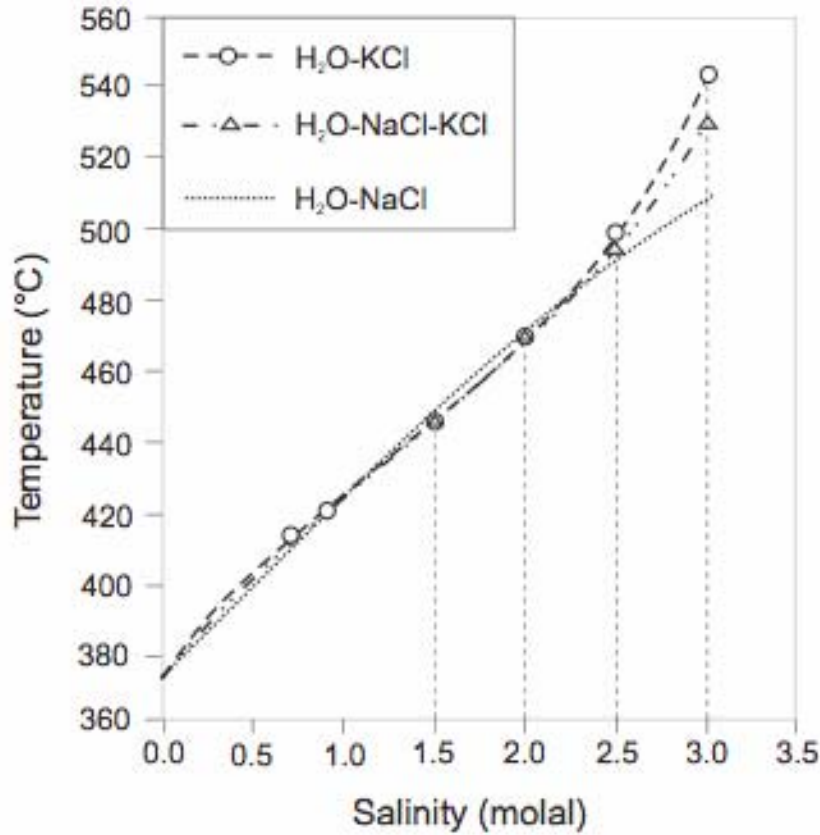


Figure 2.6. Critical temperature curves of H<sub>2</sub>O-KCl-NaCl solutions.

The only ternary composition that was studied over a significant range of salinities is H<sub>2</sub>O-NaCl-KCl with  $m_{\text{KCl}}/m_{\text{NaCl}} = 1$ . The relationship between salinity and the critical temperature for this composition is described by:

$$T_{\text{crit}} = 374.1 + 46.149 \phi + 1.4796\phi^2 \quad (2.4)$$

Equation (2.4) is valid for salinities up to 3 molal ( $0 \leq \phi \leq 3$ ).

The critical temperature of 3 molal solutions in the H<sub>2</sub>O-NaCl-KCl system increases systematically with increasing ( $m_{\text{KCl}}/m_{\text{NaCl}}$ ) according to:

$$T_{\text{crit}} = 1.8065x^2 + 41.561x + 510 \quad (2.5)$$

where  $T_{\text{crit}}$  is the critical temperature of a 3 molal H<sub>2</sub>O-NaCl-KCl solution and  $x$  is the molar ratio of KCl to NaCl (Table 2.3).

Critical pressures were determined by graphical projection of the critical isochore to the critical isotherm as described above. Small deviations in the estimated slope of the critical isochore on the calculated pressure result in an estimated error of  $\pm 2.5$  MPa.

Taking this uncertainty into account, our results show that high salinity H<sub>2</sub>O-KCl fluids have a higher critical pressure than H<sub>2</sub>O-NaCl solutions of matching molality, and that the critical pressure increases systematically with increasing  $m_{\text{KCl}}/m_{\text{NaCl}}$  (Fig 2.7; Tables 2.1, 2.2). This relationship was also confirmed by data from fluid inclusions that were trapped on critical isotherms as described above.

Table 2.2. Homogenization temperatures of and behavior of synthetic H<sub>2</sub>O–NaCl–KCl inclusions (mNaCl:mKCl = 1:1)

Sample	Composition (molal)	T <sub>form</sub> (°C)	P <sub>form</sub> (°C)	Thom (°C)	Homogenization Behavior
<i>H<sub>2</sub>O–NaCl–KCl (mNaCl:mKCl = 1:1)</i>					
011806-II	1.5	1000	600	443	L>Cr
031606-IV	1.5	1000	610	454	Cr>V
031606-V	1.5	1000	615	442	L
060505-I	1.5	1100	622	442	L
041906-VI	1.5	1100	635	449	Cr
011806-IV	1.5	1250	650	431	L
060505-II	1.5	1250	665	438	L
011806-XI	1.5	1250	685	458	V
082404-I	2.0	1000	570	452	L
082404-II	2.0	1000	600	460	L
010106-I	2.0	1000	610	474	Cr>L
010106-II	2.0	1000	630	525	V
071905-I	2.0	1100	625	407	L
120204-I	2.0	1100	635	472	Cr
022205-II	2.0	1100	640	482	V
120204-II	2.0	1100	645	488	V
120204-III	2.0	1100	660	558	V
082404-V	2.0	1150	670	570	V
071905-II	2.0	1200	665	473	V>Cr
071905-IV	2.0	1200	673	489	V
120204-VI	2.0	1250	700	506	V
071905-VI	2.0	1250	715	514	V
052505-IV	2.0	1400	740	513	V
020706-I	2.5	1000	600	489	L
020706-II	2.5	1000	612	492	Cr
020706-III	2.5	1000	625	537	V
051506-VIII	2.5	1020	620	516	V
032506-VIII	2.5	1100	630	490	L
050605-III	2.5	1100	635	491	Cr
032506-VII	2.5	1100	640	515	V
032105-IV	2.5	1100	645	532	V
051506-IX	2.5	1450	740	510	V
031606-VIII	3.0	1000	615	505	L
010106-IV	3.0	1000	625	545	V
110904-VII	3.0	1100	600	465	L
120204-I	3.0	1100	635	520	L>Cr
120204-II	3.0	1100	645	528	Cr
110904-VIII	3.0	1100	650	537	V
110904-IX	3.0	1100	700	600	V
110904-X	3.0	1250	650	488	L
120204-IV	3.0	1250	665	504	L
120204-VI	3.0	1250	680	530	Cr
110904-XI	3.0	1250	700	597	V
052505-VII	3.0	1400	710	459	L
041604-IV	3.0	1400	737	569	V

The compositional dependence of critical pressure in the H<sub>2</sub>O-NaCl system was described by Knight and Bodnar (1989) as:

$$P_{\text{crit}} = 22.1 + 12.951\phi - 0.30476\phi^2 + 0.04444\phi^3 \quad (2.6)$$

where  $P_{\text{crit}}$  is the critical pressure in MPa and  $\phi$  is the salinity (molal). Figure 2.7. shows critical pressures as a function of salinity in the H<sub>2</sub>O-NaCl, H<sub>2</sub>O-KCl and H<sub>2</sub>O-NaCl-KCl systems. The relationship between the salinity (0-3 m) and critical pressure in the H<sub>2</sub>O-KCl system based on results from this study is given by:

$$P_{\text{crit}} = 15.732 \phi + 22.1 \quad (2.7)$$

The relationship between critical pressure and composition in the H<sub>2</sub>O-KCl-NaCl system ( $m_{\text{KCl}}/m_{\text{NaCl}} = 1:1$ ) is given by the empirical equation:

$$P_{\text{crit}} = 13.744\phi + 22.1 \quad (2.8)$$

Equations (2.7) and (2.8) are valid from 0 to 3 molal and are based on data from Khaibullin and Borisov (1966) and data from this study. The relationship between critical pressure and composition for a 3 molal solution in the H<sub>2</sub>O-NaCl-KCl is given by:

$$P_{\text{crit}} = -2.8387x^2 + 13.832x + 59 \quad (2.9)$$

where  $P_{\text{crit}}$  is the critical pressure and  $x$  is the molar ratio of KCl to NaCl ( $m_{\text{KCl}}/m_{\text{NaCl}}$ ) (Table 2.3.).

Table 2.3. Homogenization temperatures of and behavior of synthetic H<sub>2</sub>O–NaCl–KCl inclusions (mNaCl:mKCl = 3:1 and 1:3).

Sample	Composition (molal)	T <sub>form</sub> (°C)	P <sub>form</sub> (°C)	Thom (°C)	Homogenization Behavior
<i>H<sub>2</sub>O-NaCl-KCl (mNaCl:mKCl = 3:1)</i>					
011406-I	3.0	1000	600	520	L
030306-VI	3.0	1000	615	532	Cr
011406-III	3.0	1000	620	537	Cr>V
011406-IV	3.0	1100	650	540	V
011406-VI	3.0	1250	670	521	L
030306-VII	3.0	1250	680	531	Cr
<i>H<sub>2</sub>O-NaCl-KCl (mNaCl:mKCl = 1:3)</i>					
011406-VIII	3.0	1050	635	542	L>Cr
030306-III	3.0	1050	645	546	Cr
011406-IX	3.0	1050	650	560	V
011406-XI	3.0	1050	665	595	V
050106-V	3.0	1200	690	546	Cr>L

In fluid inclusion studies, knowing the P-T projection of the critical isochore can provide useful constraints on inclusion formation conditions. Thus, inclusions that were trapped in the one-phase field and which homogenize to the liquid phase must have been trapped at P-T conditions above the critical isochore. Slopes of critical isochores were determined from the formation conditions of fluid inclusions that homogenize by critical behavior, as described above (Fig. 2.8.). The slope of the critical isochore for H<sub>2</sub>O–KCl solutions is less steep than those for H<sub>2</sub>O–NaCl solutions of the same salinity (Fig.2.8.).

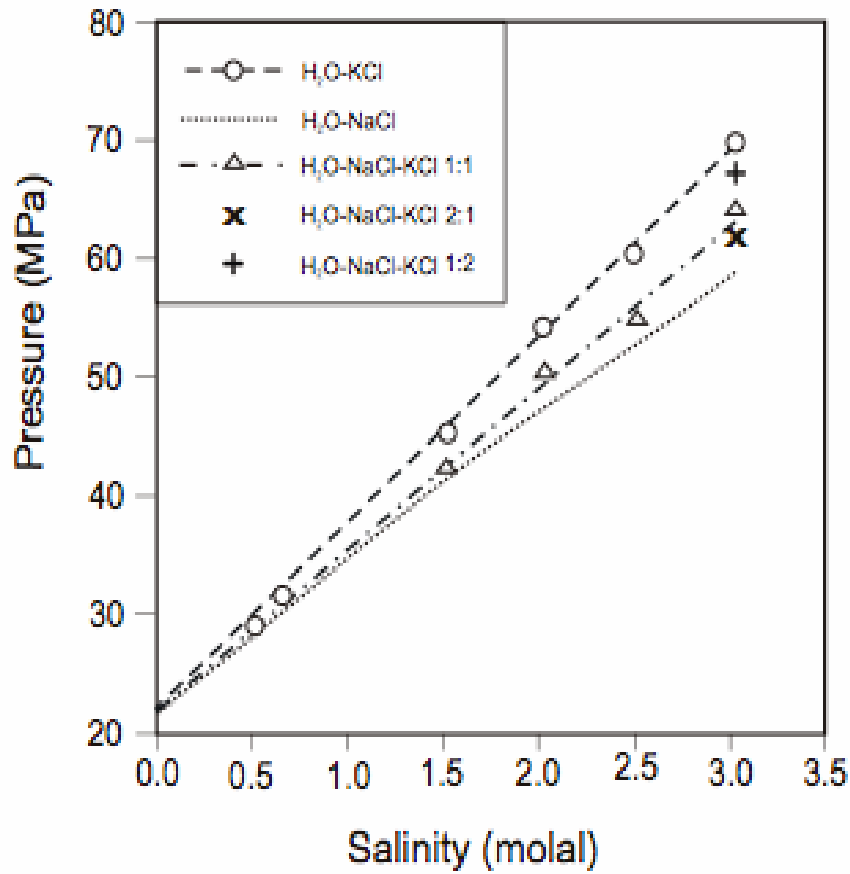


Figure 2.7. Critical pressure curves of H<sub>2</sub>O-KCl-NaCl solutions.

This suggests that H<sub>2</sub>O-KCl critical fluids are less compressible than those of H<sub>2</sub>O-NaCl solutions of similar salinity.

Knight and Bodnar (1988) reported the following relationship between critical temperature and pressure in the H<sub>2</sub>O-NaCl system:

$$P = 209.4 - 205.6T + 0.006896T^2 - 8.903 \times 10^{-6}T^3 + 4.214 \times 10^{-9}T^4 \quad (2.10)$$

Where P is the critical pressure and T is the critical temperature. The relationship between critical temperature and pressure for H<sub>2</sub>O-KCl, based on results of this study, is:

$$P = 729.64 - 5.3276T + 0.01276T^2 - 1 \times 10^{-5}T^3 \quad (2.11)$$

As shown on Figure 2.9., the P-T projections of the H<sub>2</sub>O-NaCl and H<sub>2</sub>O-KCl curves appear similar, but note the significant and increasing difference in salinity for the two systems.

A few preliminary measurements were conducted on 2 m H<sub>2</sub>O-NaCl-KCl-CaCl<sub>2</sub> solutions to investigate the effect of CaCl<sub>2</sub> compared to NaCl and KCl. Our results, combined with data from Oakes and co-workers (1994) demonstrate that H<sub>2</sub>O-CaCl<sub>2</sub> solutions have significantly higher critical pressures and somewhat lower critical temperatures compared to 2 m KCl and NaCl solutions (Fig. 2.10.).

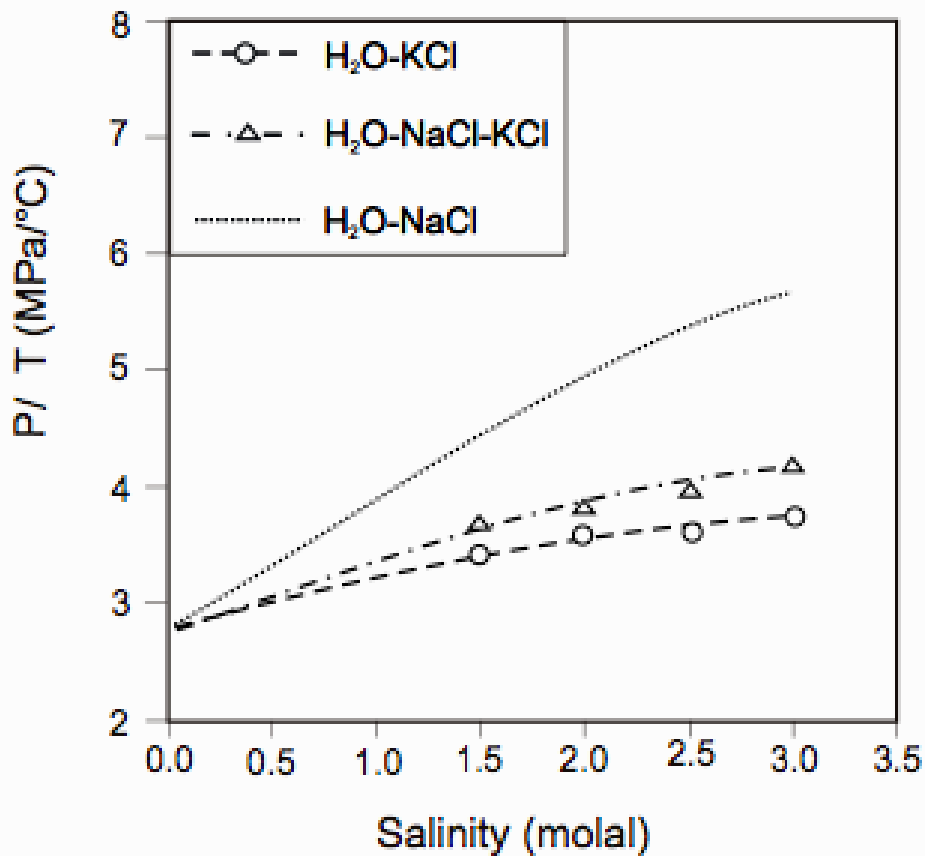


Figure 2.8. Critical isochore slopes of H<sub>2</sub>O-KCl-NaCl solutions.

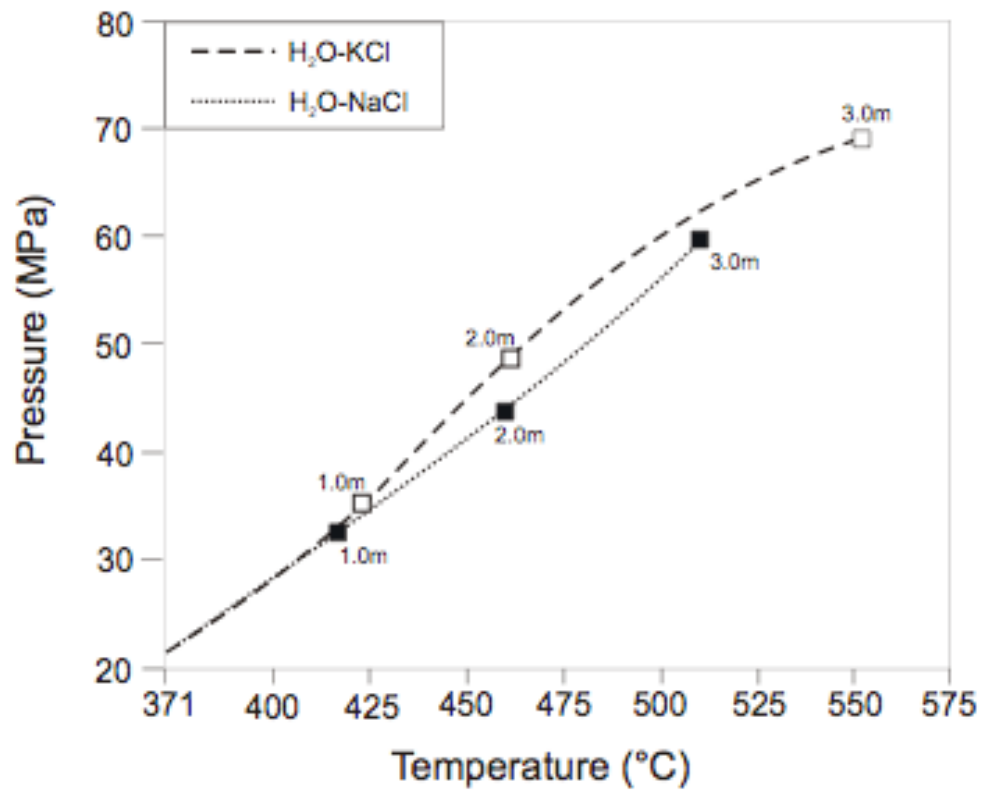


Figure 2.9. Critical curves of H<sub>2</sub>O-KCl and H<sub>2</sub>O-NaCl solutions.

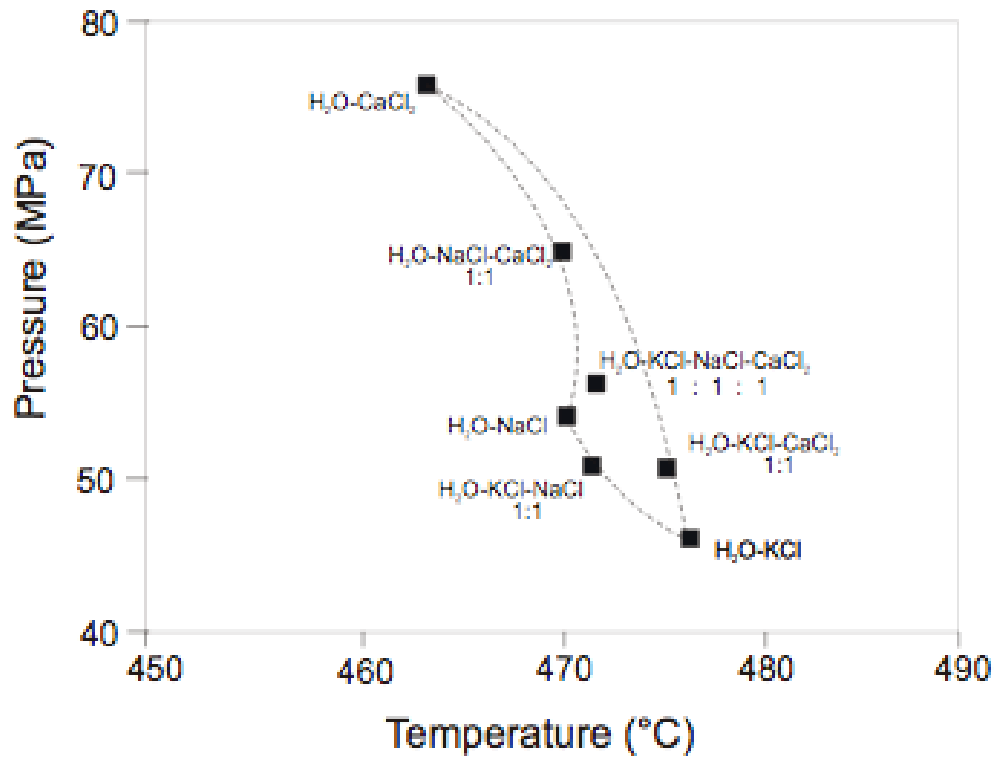


Figure 2.10. Critical points of 2 molal H<sub>2</sub>O-NaCl-KCl-CaCl<sub>2</sub> solutions. Dashed lines represent projected mixing curves between the binary end-member solutions. Ratios represent the molar ratio of solutes in ternary and quaternary solutions.

## **II.5. Summary**

Experimental results show that the critical temperature and pressure of H<sub>2</sub>O-NaCl-KCl solutions varies systematically with composition. Compared to H<sub>2</sub>O-NaCl, the critical temperature and pressure of H<sub>2</sub>O-KCl for a solution of the same salinity is higher, and this difference increases with increasing salinity. Results of this study suggest that the PTX properties of H<sub>2</sub>O-NaCl may be appropriate to model the behavior of low salinity fluids, but that significant errors may result for salinities greater than 3 molal.

Results of this study may be used to predict the mass and energy transport behavior of convecting hydrothermal systems. Fluids have very different transport properties, depending on whether they are in a supercritical, critical, subcritical one-phase or subcritical multi-phase state. This has a great effect on their mass and energy transport capabilities in hydrothermal environments. Of special interest is the P-T region in the vicinity of the critical point and along the critical isochore, where most fluid transport properties show extrema (either maxima or minima). Results from this study provide information on the P-T conditions at which this region of extrema should occur for different fluid compositions.

The locus of critical points in a given fluid system defines the boundaries of the P-T field in which an immiscible liquid and vapor can coexist. Knowing the location of this boundary between one-phase and two-phase conditions thus provides constraints on conditions associated with postmagmatic processes such as late stage crystallization and hydrothermal ore deposition.

## **II.6. Acknowledgements**

The authors would like to express their sincere thanks to Csaba Szabó for his continuous support and for providing equipment for some of the fluid inclusion analysis. The authors also thank Charles Farley for technical assistance with sample preparation. Andras Fall, Claudia Cannatelli and Bebe Oh provided valuable technical and editorial suggestions. Funding for this project was provided by NSF grant EAR-0125918 to R. J. Bodnar.

## II.7. References

- Anderko, A., Pitzer, K. S., (1993a): Equation-of-state representation of phase equilibria and volumetric properties of the system NaCl-H<sub>2</sub>O above 573K. *Geochim. Cosmochim. Acta.* 57, 1657-1680.
- Anderko, A., Pitzer, K. S., (1993b): Phase equilibria and volumetric properties of the systems KCl-H<sub>2</sub>O and NaCl-KCl-H<sub>2</sub>O above 573 K: Equation of state representation. *Geochim. Cosmochim. Acta.* 57, 4885-4897.
- Baker, E. T., (1995): Characteristics of hydrothermal discharge following magmatic intrusion. *In Hydrothermal Vents and Processes.* Parson, L. M., Walker, C. L., Dixon, D. R., eds. The Geological Society, London. 411 pgs.
- Bischoff, J. L., Rosenbauer, R. J., (1985): An empirical equation of state for hydrothermal seawater (3.2 percent NaCl). *Amer. J. Sci.* 285, 725-763.
- Bischoff, J. L., Rosenbauer, R. J., Pitzer, K. S., (1986): The system NaCl-H<sub>2</sub>O: relations of vapor-liquid near the critical temperature of water and of vapor-liquid-halite from 300°C to 500°C. *Geochim. Et Cosmochim. Acta.* 50, 1437-1444.
- Bodnar, R. J., Burnham, C. W., Sterner, S. M., (1985): Synthetic fluid inclusions in natural quartz; III, Determination of phase equilibrium properties in the system H<sub>2</sub>O-NaCl to 1000 degrees C and 1500 bars. *Geochim. Cosmochim. Acta.* 49, 9, 1861-1873.
- Bodnar, R. J., Sterner, S. M., Hall, D. L., (1989): SALTY; a Fortran program to calculate compositions of fluid inclusions in the system NaCl-KCl-H<sub>2</sub>O. *Computers and Geosciences.* 15, 1, 19-41.
- Bodnar, R. J., Costain, J. K., (1991): Effect of Varying Fluid Compositions on Mass and Energy Transport in the Earth's Crust. *Geophysical Research Letters.* 18, 5, 983-986.
- Bodnar, R. J., Sterner, M. S., (1987): Synthetic fluid inclusions. Hydrothermal experimental techniques. John Wiley and Sons, New York. 423-457.
- Brunner, G., Misch, B., Firus, A., Nowak, K., (2001): Supercritical water and supercritical carbon dioxide for cleaning of soil material, in *Treatment of*

- contaminated soil; fundamentals, analysis, applications.* Springer, Berlin, Germany.
- Cathles, L. M., (1997): Thermal aspects of ore formation, in *Geochemistry of hydrothermal ore deposits*. John Wiley and Sons, New York, NY, United States.
- Cline, J. S., Bodnar, R. J., (1994): Direct evolution of brine from a crystallizing silicic melt at the Questa, New Mexico, Molybdenum Deposit. *Economic Geology*. 89, 1780-1802.
- Driesner, T., Heinrich, C. A., (2002): Revised critical curve for the system H<sub>2</sub>O-NaCl, *Geochim. Et Cosmochim. Acta*. 66, 15a, a196.
- Gammon, R.W., (1987): Critical Fluid Light Scattering, in *The Nation's Future Material Needs*, T. Lynch, J. Persh, T. Wolf, and N. Rupert, eds. (Soc. Adv. Mater. and Process Eng., Covina, CA, 1987), Proceedings of the 19th International Technical Conference of the Society for the Advancement of Material and Process Engineering (SAMPE), Oct. 13--15, 1987.
- Haar, L., Gallagher, J. S., Kell, G. S., (1984): NBS/NRC Steam tables: Thermodynamic and transport properties and computer programs for vapor and liquid states of water in SI units. Hemisphere. 320 pgs.
- Johnson, J. W., Norton, D., (1991): Critical phenomena in hydrothermal systems; state, thermodynamic, electrostatic, and transport properties of H<sub>2</sub>O in the critical region. *American Journal of Science*. 291, 6, 541-648.
- Jupp, T., Schultz, A., (2000): A thermodynamic explanation for black smoker temperatures. *Nature*. 403, 880-883.
- Khaibullin, I. Kh., Borisov, N. M., (1966): Experimental investigation of the thermal properties of aqueous and vapor solutions of sodium and potassium chlorides at phase equilibrium. *In Russian*. *Teplofizika vysokikh temperatur*. 4, 4, 518-523.
- Knight, C. L., Bodnar, R. J. (1989): Synthetic fluid inclusions: IX. Critical PVTX properties of NaCl-H<sub>2</sub>O solutions. *Geochim. et Cosmochim. Acta* 53, 3-8.
- Levelt Sengers, J. M. H. (1994): Critical behavior of fluids: concepts and applications, in Kiran, E. and Levelt Sengers, J. M. H. (eds) *Supercritical Fluids: Fundamentals for Applications*. Kluwer Academic Publishers. 1-38.

- Levelt Sengers, J. M. H. (1998): Supercritical Fluids: Their Properties and Applications, in *Supercritical Fluids: Fundamentals and Applications*, Kiran, E., Debenedetti, P. G., Peters, C. J., eds. (Kluwer Academic Publishers, 1998), Proceedings of the NATO. Advanced Study Institute, Antalya, Turkey, July 12-24, 1998.
- Marshall, W. L., Jones, E. V., (1974): Liquid-vapor critical temperatures of aqueous electrolyte solutions. *J. Inorganic nuclear Chem.* 36, 2313-2318.
- Oakes, C. S., Bodnar, R. J., Simonson, J. M., Pitzer, K. S., (1994): Critical and supercritical properties for 0.3 to 3.0 mol · kg<sup>-1</sup> CaCl<sub>2</sub>(aq). *Geochim. Cosmochim. Acta.* 58, 11, 2421-2431.
- Pitzer, K. S., (1984): Critical point and vapor pressure of ionic fluids including NaCl and KCl. *Chem. Phys. Letters.* 105, 484-489.
- Potter, R. W., Babcock, R. S., Czamanske, G. K., (1976): An investigation of the critical liquid-vapor properties of dilute KCl solutions. *Journal of Solution Chemistry.* 5, 3, 223-230.
- Povodyrev, A. A., Anisimov, M. A., Sengers, J. V., Marshall W. L., Levelt Sengers J. M. H., (1999): Critical Locus of Aqueous Solutions of Sodium Chloride. *Int. J. Thermophys.* 20 1529.
- Roedder, E., Ingram, B., Hall, W. E., (1963): Studies of fluid inclusions III: Extraction and quantitative analysis of inclusions in the milligram range. *Econ. Geol.*, 58, 353-374.
- Roedder, E., (1984): Fluid inclusions. *Reviews in Mineralogy.* 12, 664p.
- Savage, P. E., Gopalan, S., Mizan, T. I., Martino, C. J., Brock, E. E., (1995): Reactions at supercritical conditions: Applications and Fundamentals. *AICHE Journal.* 41, 1723-1778.
- Savage, P. E., Oh, C. H., (2001): Supercritical Water Oxidation. In *Hazardous and Radioactive Waste Treatment Technologies Handbook*. Chang, H. O. ed. CRC Press.
- Shmulovich, K.I., Tkachenko, S.I., Plyasunova, N.V., (1995): Fluids in the crust. Chapman and Hall, 193-214.
- Sourirajan, S; Kennedy, G C, (1962): The system H<sub>2</sub>O- NaCl at elevated temperatures and pressures. *Am. J. Sci.* 260, 1616.

- Sterner, S. M., Bodnar, R. J., (1984): Synthesis of fluid inclusions in natural quartz. *Eos, Transactions, American Geophysical Union.* 65, 16, 292.
- Tanger, J. C., Pitzer, K. S., (1989): Thermodynamics of NaCl-H<sub>2</sub>O; a new equation of state for the near-critical region and comparisons with other equations for adjoining regions. *Geochim. Cosmochim. Acta.* 53, 973-987.
- Tester, J.W., Holgate, H. R., Armellini, F. J., Webley, P. A., Killilea, W. R., Hong, G. T., Barner, H. E., (1993): Supercritical Water Oxidation Technology: Process Development and Fundamental Research. In *Hazardous Waste Management III.* Tedder, D. W., Pohland, F. G., eds. Maple Press, York. 466 pgs.
- Urusova, M. A., (1974): *Russ. J. Inorg. Chem.* 19, 450-454.
- Valyashko, V. M., (2004): Phase equilibria properties of water – salt systems at high temperatures and pressures. In *Aqueous systems at elevated temperatures and pressures: Physical chemistry in water, steam and hydrothermal solutions.* Palmer, D. A., Fernandez-Prini, D., Harvey, A. H., eds. Elsevier. 754 pgs.
- Von Damm, K. L., Colander, D. C., Edmonds, H. N., (1992): Hydrothermal fluid chemistry at 9°-10°N EPR '92: big changes and still changes. *Eos, Transactions of the American Geophysical Union.* 73, 524.
- Zhang, Y., Frantz, J. D., (1987): Determination of the homogenization temperatures and densities of supercritical fluids in the system NaCl-KCl-CaCl<sub>2</sub>-H<sub>2</sub>O using synthetic fluid inclusions. *Chem. Geol.* 64, 335-350.

## **CHAPTER 3. In Situ Quantitative Analysis of Individual H<sub>2</sub>O-CO<sub>2</sub> Fluid Inclusions by Laser Raman Spectroscopy**

*Co-authored chapter: Tristan Azbej, Matthew J. Severs*

### **III.1. Introduction**

Fluid inclusions with compositions approximated by the H<sub>2</sub>O + CO<sub>2</sub> ± NaCl system are common in many geologic environments, including hydrothermal ore deposits and medium- to high-grade metamorphic rocks (e.g. Roedder, 1984). The presence of even small amounts of CO<sub>2</sub> can significantly affect phase equilibrium and PVT properties of the inclusion fluids, compared to CO<sub>2</sub>-free fluids (Bodnar et al., 1985; Diamond, 2003). Therefore, accurate interpretation of microthermometric data from CO<sub>2</sub>-bearing inclusions requires information on the CO<sub>2</sub> concentration of the inclusion fluids. This study describes a technique to determine the CO<sub>2</sub> concentration, based on Raman spectroscopic analysis of individual inclusions. This method builds upon earlier studies in which Laser Raman Spectroscopy (LRS) (e.g. Seitz et al. 1992; 1993; 1996; Leng et al., 1998; Dubessy et al., 1999; 2001; Pironon et al., 2003) and Fourier Transform Infrared Spectroscopy (FTIR) (e.g., Linnen et al., 2004) were used for quantitative analysis of volatile-bearing inclusions.

Several previous studies have described the application of Raman spectroscopy for quantitative analysis of H<sub>2</sub>O-CH<sub>4</sub> fluid inclusions. These workers calibrated the technique using synthetic inclusions of known composition (Leng et al., 1998; Dubessy et al, 1999), and the results have been applied to determine compositions of natural H<sub>2</sub>O-CH<sub>4</sub> inclusions containing <10.4 mol% CH<sub>4</sub> (Dubessy et al, 2001). Pironon et al. (2003) observed an increase in the CH<sub>4</sub>/H<sub>2</sub>O peak intensity ratio at temperatures at >175°C. They related this increase to decomposition of the water stretching band and discussed the implications for quantitative applications. Seitz and coworkers (1992; 1993; 1996) developed a technique to determine the composition and pressure in CO<sub>2</sub>-CH<sub>4</sub> and CH<sub>4</sub>-N<sub>2</sub> inclusions based on relative LRS peak height (intensity), peak area (integrated intensity) and peak width at half maximum intensity.

Rosso and Bodnar (1995) combined Raman spectrometry with microthermometry to determine the minimum detection limits for CO<sub>2</sub> in H<sub>2</sub>O-CO<sub>2</sub> inclusions, and used Raman spectra to determine the density of the homogenous CO<sub>2</sub> phase in inclusions. Bodnar et al. (1996) presented a preliminary calibration equation relating CO<sub>2</sub> concentrations to the Raman peak intensities. Shuling (1998) observed a linear relationship between the CO<sub>2</sub> peak intensity and CO<sub>2</sub> concentration in the gas phase of H<sub>2</sub>O-CO<sub>2</sub> inclusions at room temperature. However, he did not observe a simple relationship between CO<sub>2</sub> concentration in the liquid phase and CO<sub>2</sub> peak intensity. Nambu et al. (1990) used FTIR to analyze powdered quartz containing synthetic H<sub>2</sub>O-CO<sub>2</sub> fluid inclusions. Linnen et al. (2004) analyzed homogenized, H<sub>2</sub>O-CO<sub>2</sub> synthetic fluid inclusions containing 12.5 to 62.5 mole % CO<sub>2</sub> using FTIR. While both LRS and FTIR have been applied to the quantitative analysis of H<sub>2</sub>O-CO<sub>2</sub> inclusions, LRS is the preferred technique because inclusions as small as 1 μm can be analyzed (compared to a minimum of about 25 μm with FTIR) and knowledge of the thickness of the host is not required for quantitative LRS analysis, unlike FTIR (Wopenka and Pasteris, 1986; Pasteris et al., 1988).

### III.2. Analytical Methods

The synthetic fluid inclusion technique (Sterner and Bodnar, 1984; Bodnar and Sterner, 1987) was used to produce H<sub>2</sub>O-CO<sub>2</sub> standards for calibration. Oxalic acid and H<sub>2</sub>O were loaded into platinum capsules (5 mm OD x 2.5 cm long) to form fluid inclusions with compositions ≤50 mole % CO<sub>2</sub>. Oxalic acid decomposes explosively at 157°C to produce equimolar concentrations of CO<sub>2</sub> and H<sub>2</sub>O, as well as H<sub>2</sub>, according to the reaction (Sterner and Bodnar, 1991):



As shown by equation (1), one mole of H<sub>2</sub> is generated for every two moles of CO<sub>2</sub> and H<sub>2</sub>O by decomposition of oxalic acid. Owing to the stoichiometry of Equation

1, inclusions containing >50 mol% CO<sub>2</sub> cannot be synthesized using this method. Representative inclusions were analyzed by Raman to test for the presence of H<sub>2</sub> (major peak at 4156 cm<sup>-1</sup>), but none was found. The lack of H<sub>2</sub> in the inclusions is consistent with previous studies by Mavrogenes and Bodnar (1994) who documented the rapid loss of H<sub>2</sub> from inclusions at elevated temperature by diffusion through quartz, and is also consistent with the high permeability of platinum to hydrogen at elevated temperatures (Chou, 1986). The redox gradient between the initial hydrogen-bearing fluid in the capsule and the more oxidizing Ni-NiO buffer environment outside of the capsule (controlled by Ni-bearing stainless steel of the pressure vessel) serves as the driving force for hydrogen diffusion.

Known amounts of liquid water and oxalic acid were added to the capsule along with thermally-fractured and (virtually) inclusion-free 'Brazilian quartz' cores or prisms to serve as the host for the inclusions. After sealing, the capsules were weighed, maintained at 120°C in a vacuum oven for several hours, and weighed again to assure the quality of the seal. If no leakage occurred, the capsules were loaded into externally-heated, cold-seal pressure vessels, pressurized, and heated to the desired experimental conditions, typically 3 kbars and 600°C, to assure that the inclusions are trapped in the single-phase fluid field. During the experiment, fractures in the quartz heal and trap the homogenous solution to produce synthetic fluid inclusions. After 7 to 10 days, the vessels were removed from the furnaces and quenched. The capsules were cleaned and weighed to check for leakage during the runs. Quartz cores were sliced into 1mm thick disks and polished for petrographic and microthermometric analyses.

In order to determine the bulk composition by LRS, the inclusions must contain a homogeneous fluid at the time they are analyzed. Additionally, all analyses should be conducted at the same temperature to minimize variations in the Raman spectra as a function of temperature, as discussed in more detail below. In the pure H<sub>2</sub>O-CO<sub>2</sub> system, the maximum temperature at which two phases (H<sub>2</sub>O-rich and CO<sub>2</sub>-rich) may coexist is the critical temperature of H<sub>2</sub>O, as addition of CO<sub>2</sub> results in a shift in the critical temperature to lower temperatures and higher pressures (Franck and Todheide, 1959; Takenouchi and Kennedy, 1964; Bodnar and Costain, 1991; Sterner and Bodnar, 1991; Diamond, 2003). Thus, ideally, the calibration and analysis of H<sub>2</sub>O-CO<sub>2</sub> inclusions

should be conducted at 374.1°C (or higher) to assure that all inclusions, regardless of composition or density, are homogeneous. However, H<sub>2</sub>O-CO<sub>2</sub> inclusions generate significant internal pressures during heating (especially after they homogenize), and may leak or decrepitate if the internal pressure approaches 1 kbar (Leroy, 1979; Bodnar et al., 1989; Bodnar, 2003). This often precludes heating of the inclusions significantly beyond the homogenization temperature. As a compromise, the synthetic inclusion calibration was conducted at 350°C. This temperature is sufficiently high that, except for inclusions representing a narrow range in composition and density, all H<sub>2</sub>O-CO<sub>2</sub> inclusions should be homogeneous at 350°C, yet this temperature is sufficiently low that most inclusions have not leaked or decrepitated. In this study, the H<sub>2</sub>O-CO<sub>2</sub> synthetic fluid inclusions homogenized between 292 and 339°C, and decrepitation was only rarely observed during heating to the analytical temperature (350°C). In fact, one sample containing 12.5 mole % CO<sub>2</sub> inclusions that homogenized at 307°C was heated to 450°C with no evidence of leakage or decrepitation. However, high density natural inclusions may stretch or decrepitate before homogenization is achieved. Stretching of inclusions does not change the composition of the trapped fluid (Bodnar, 2003), and analysis of such inclusions should provide reliable compositions.

Analyses of homogenized inclusions were carried out using a Jobin Yvon Horiba HR 800 LabRAM Raman microprobe equipped with an Olympus BX 41 petrographic microscope and a Linkam THMSG 600 heating stage that was calibrated using synthetic fluid inclusion standards (Sterner and Bodnar, 1984). The microprobe was equipped with an Ancor electronically cooled charge-coupled device (CCD) detector and analyses were carried out using a 514.57 nm Ar-ion laser operated in confocal mode with the slit width set to 150 µm and confocal aperture set to 400 µm. A 40x microscope objective with a cover glass correction was used to improve signal throughout following the method of Adar et al. (2004). Spectra were collected in two windows (1000 - 2500 cm<sup>-1</sup> and 2360 - 3860 cm<sup>-1</sup>) covering the range from 1000 to 3860 cm<sup>-1</sup>, which includes the Fermi diad peaks of CO<sub>2</sub> and the O-H stretching band of H<sub>2</sub>O (Fig. 3.1). Spectral resolution (related to one pixel of the detector) was approximately 1.4 cm<sup>-1</sup>.

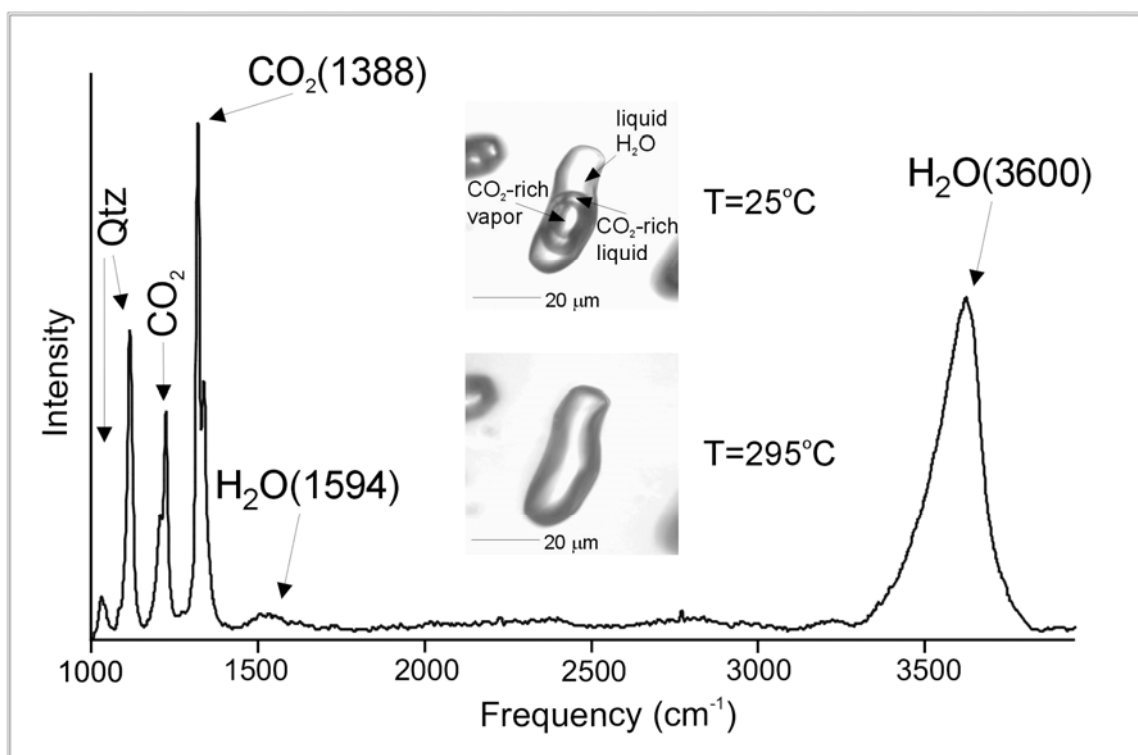


Figure 3.1. Raman spectrum (at 350°C) showing the peaks for CO<sub>2</sub> (1388 cm<sup>-1</sup>) and H<sub>2</sub>O (3600 cm<sup>-1</sup>) that were used for calibration, as well as the lower member of the CO<sub>2</sub> Fermi diad (labeled CO<sub>2</sub>) the bending mode of H<sub>2</sub>O (1594 cm<sup>-1</sup>) and two quartz peaks (labeled Qtz). The photomicrograph shows an H<sub>2</sub>O-CO<sub>2</sub> inclusion containing 25 mole % CO<sub>2</sub> at 25°C and at the homogenization temperature (295°C).

During the initial stages of this study, data collection and interpretation parameters were varied to determine the best compromise between acquisition time and data reproducibility. Spectra were interpreted after manual baseline correction to eliminate background noise using the Labspec software. These tests showed that H<sub>2</sub>O and CO<sub>2</sub> peak area ratios show little variation after about 5 60-second accumulations (300 seconds total acquisition time) (Fig. 3.2). Thus, all spectra reported here represent 5 accumulations of 60 seconds each and, on average, ten fluid inclusions were analyzed for each composition. Several previous workers showed that both peak area and peak intensity are proportional to the number of target molecules in the analytical volume and that either could be used to determine compositions of fluid inclusions (e.g. Schrötter and

Klößner, 1979; Dubessy et al., 1989; Seitz et al., 1996). In this study we confirm these earlier findings and also document that while the linear peak intensity ratio varies as a function of temperature, the peak area ratio remains fairly constant. The implications of this result for fluid inclusion analysis are considered below.

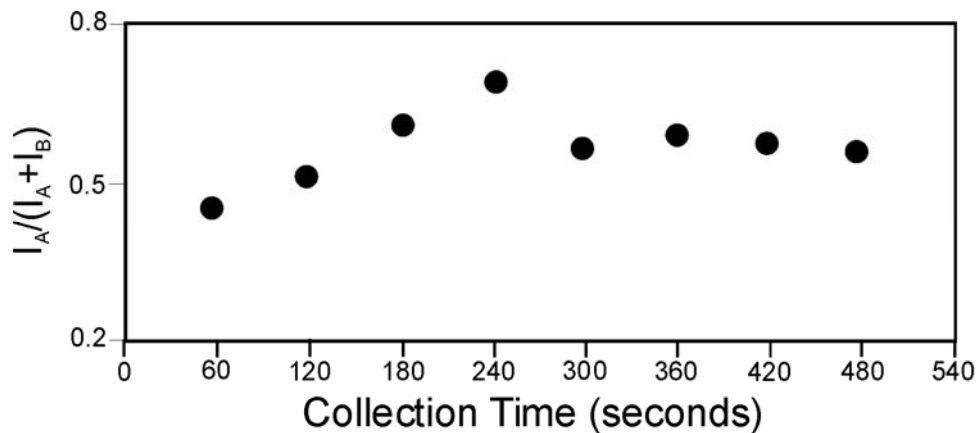


Figure 3.2. Raman linear peak intensity ratios calculated for different acquisition times from a 25 mole % H<sub>2</sub>O-CO<sub>2</sub> inclusion. I<sub>A</sub> represents the CO<sub>2</sub> linear peak intensity at 1388 cm<sup>-1</sup> and I<sub>B</sub> represents the H<sub>2</sub>O linear peak intensity at 3600cm<sup>-1</sup>.

### III.3. Results and Discussion

A typical Raman spectrum of an H<sub>2</sub>O-CO<sub>2</sub> fluid inclusion is shown on Figure 1, and includes the Fermi diad for CO<sub>2</sub> (2ν<sub>2</sub> at 1388 cm<sup>-1</sup> and ν<sub>1</sub> at 1285 cm<sup>-1</sup>, as reported by many workers including Dickinson et al. (1929), Herzberg (1945), Davis and Oliver (1972) and Anderson (1977)), the bending mode band of H<sub>2</sub>O at 1594 cm<sup>-1</sup> and the broad H<sub>2</sub>O band between approximately 3200 and 3750 cm<sup>-1</sup>. For the sake of simplicity we refer to this last band as the ‘H<sub>2</sub>O peak at 3600 cm<sup>-1</sup>’.

Previous workers have described variation in the Fermi diad that reflects changes in the vibrations of CO<sub>2</sub> molecules in an aqueous environment (Davis & Oliver, 1972; Anderson, 1976). According to these reports the diad peaks included shift from 1388 cm<sup>-1</sup> and 1285 cm<sup>-1</sup> to 1383 cm<sup>-1</sup> and 1274 cm<sup>-1</sup>, respectively, when CO<sub>2</sub> is dissolved in H<sub>2</sub>O. This shift reflects the formation of bonds between CO<sub>2</sub> and H<sub>2</sub>O molecules (Davis & Oliver, 1972; Anderson, 1976). The most common CO<sub>2</sub> aqueous species under the

studied conditions is CO<sub>2</sub>(aq). The fact that the general symmetry of the Fermi diad for pure gaseous CO<sub>2</sub> is similar to that of CO<sub>2</sub>(aq) suggests that the average symmetry of the molecule does not change significantly during solution (Davis & Oliver, 1972; Anderson, 1976). Spectra collected from H<sub>2</sub>O-CO<sub>2</sub> solutions in this study also show a Fermi diad symmetry that is similar to that of pure CO<sub>2</sub>. However, the peaks do not shift to lower frequencies as expected. The reason for this is not fully understood, and the effect of temperature on the spectrum of CO<sub>2</sub> is not well known.

Several combinations of CO<sub>2</sub> and H<sub>2</sub>O peak area and intensity ratios were analyzed statistically to determine the combination that gave the most consistent results. The linear peak intensity ratio (IR) of the higher energy-state member of the CO<sub>2</sub> Fermi diad (2ν<sub>2</sub>) at 1388 cm<sup>-1</sup> divided by the sum of the intensities of the 2ν<sub>2</sub> component of the Fermi diad at 1388 cm<sup>-1</sup> and the O-H stretching vibration band of H<sub>2</sub>O at around 3600 cm<sup>-1</sup> provided the smallest statistical error throughout the studied compositional range. Using these parameters, the relationship between linear peak intensity ratio (IR) and fluid composition at 350°C is given by:

$$\text{Mole \% CO}_2 = e^{-3.959 \text{ IR}^2 + 8.0734 \text{ IR}} \quad (3.2)$$

where IR is the intensity ratio defined above (Fig. 3.3, Table 3.1). Equation (3.2) is valid for compositions between 0 and 50 mole % CO<sub>2</sub> in the H<sub>2</sub>O–CO<sub>2</sub> binary system. The R-squared value of the regression curve is R<sup>2</sup> = 0.9894 and standard errors are the same magnitude as those reported by Linnen et al. (2004) for FTIR analysis of H<sub>2</sub>O-CO<sub>2</sub> fluid inclusions. The standard error is lower for compositions less than 25 mole% CO<sub>2</sub> and higher for the 25 and 50 mole % CO<sub>2</sub> compositions (Table 3.1.).

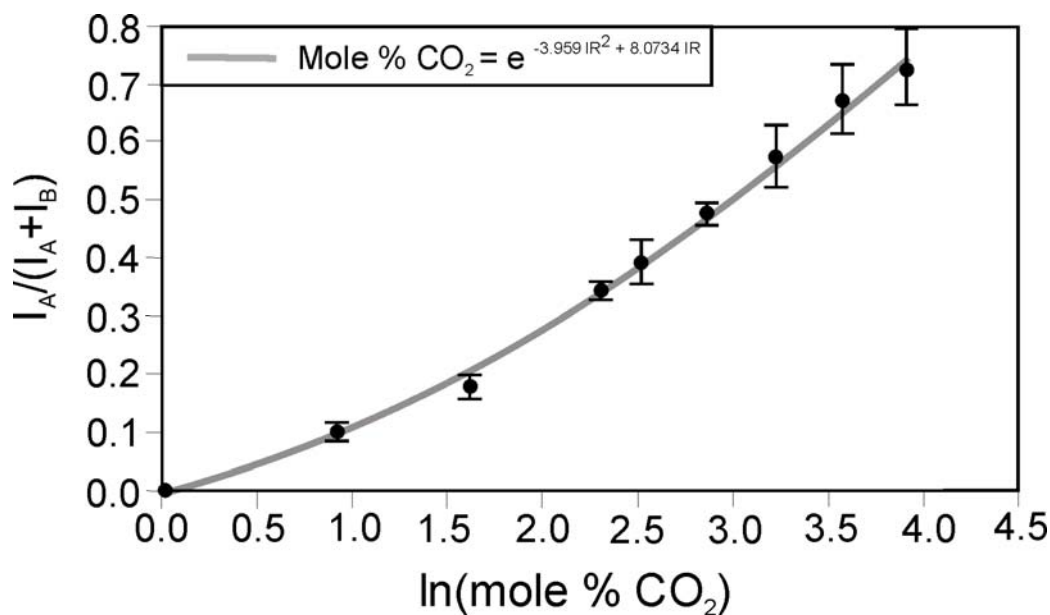


Figure 3.3. Relationship between composition of H<sub>2</sub>O-CO<sub>2</sub> inclusions and Raman spectral intensity ratios. I<sub>A</sub> represents the CO<sub>2</sub> linear peak intensity at 1388 cm<sup>-1</sup>, I<sub>B</sub> represents the H<sub>2</sub>O linear peak intensity at 3600cm<sup>-1</sup> and ln(mole % CO<sub>2</sub>) is the natural logarithm of the CO<sub>2</sub> concentration in mole %. The calibration curve is extrapolated to 0 mole % CO<sub>2</sub>, however the lowest CO<sub>2</sub> concentration analyzed was 2.5 mole %

Table 3.1. Raman linear peak intensity ratios of H<sub>2</sub>O-CO<sub>2</sub> synthetic fluid inclusion standards.

<u>Mole % CO<sub>2</sub></u>	<u>Th (°C)</u>	<u>IR</u>	<u>Std Dev %</u>	<u># Spectra</u>
2.5	305	0.10	3.31	12
5	302	0.19	6.94	12
10	302	0.35	3.87	14
12.5	305	0.39	8.06	6
17.5	309	0.48	2.21	9
25	293	0.58	8.90	8
40	310	0.68	6.22	10
50	316	0.73	11.7	12

*Th* is the average homogenization temperature of inclusions within the sample;  
*IR* is the intensity ratio of the 1388 cm<sup>-1</sup> CO<sub>2</sub> peak divided by its sum with the intensity of the 3600 cm<sup>-1</sup> H<sub>2</sub>O band;  
*Std Dev* represents the standard deviation in percent;  
*# Spectra* is the number of spectra acquired for each sample.

Calibration equation (3.2.) describes the relationship between the intensity ratio and composition at 350°C. However, it may not always be possible to analyze natural H<sub>2</sub>O-CO<sub>2</sub> fluid inclusions at 350°C as they may decrepitate during heating to that temperature (Bodnar et al., 1989; Bodnar, 2003), or they may have a homogenization temperature in excess of 350°C. To examine the effect of temperature on the relationship between the Raman intensity ratio and composition described by equation (3.2), six inclusions containing 12.5 mole % CO<sub>2</sub> were analyzed at several temperatures ranging from the homogenization temperature (307°C) to 450°C. Results show that the intensity ratio (IR = I<sub>CO<sub>2</sub></sub> / (I<sub>CO<sub>2</sub></sub> + I<sub>H<sub>2</sub>O</sub>)) decreases with increasing temperature (Fig 3.4., Table 3.2.). This relationship between temperature and IR is the opposite of that described by Pironon et al. (2003) for the CH<sub>4</sub>-H<sub>2</sub>O system. The deviation of the IR from that obtained at 350°C and predicted by equation (3.2) is given by the relationship:

$$\Delta IR = IR^* - IR \quad (3.3)$$

where  $\Delta IR$  is the intensity ratio difference, and IR and IR\* describe the CO<sub>2</sub> and H<sub>2</sub>O linear peak intensity ratios (= I<sub>CO<sub>2</sub></sub> / (I<sub>CO<sub>2</sub></sub> + I<sub>H<sub>2</sub>O</sub>)) at 350°C and at the analytical temperature, respectively. Based on our results, IR\* for a 12.5 mole % CO<sub>2</sub> inclusion is described by the relationship:

$$IR^* = -0.0009 T + 0.7131 \quad (3.4)$$

where T is the analytical temperature in degrees Celsius (Fig. 3.4). Equation (3.4) is valid from 307°C to 450°C.

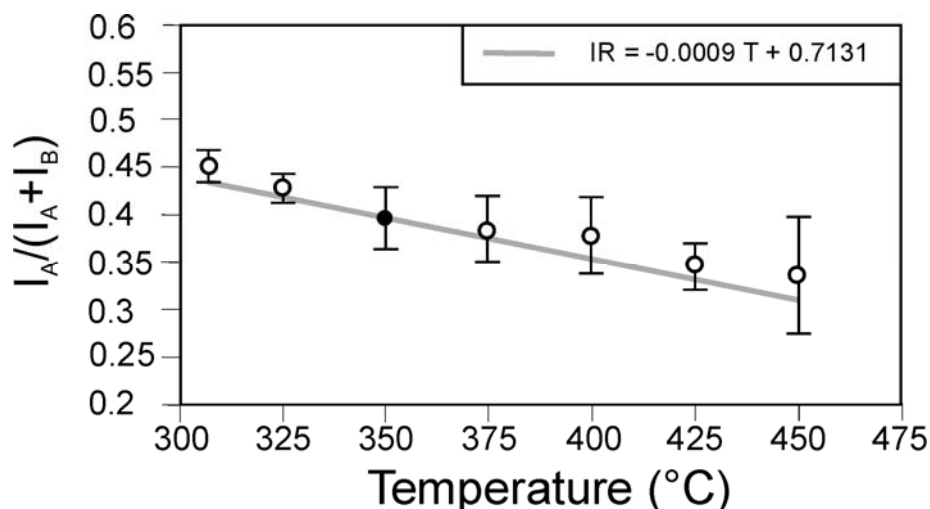


Figure 3.4. Raman linear peak intensity ratios of CO<sub>2</sub>-H<sub>2</sub>O inclusions containing 12.5 mole % CO<sub>2</sub> acquired at temperatures between 307°C and 450°C. Filled symbol at 350°C represents the intensity ratio used in equation (2). Grey line represents a linear regression of the data that is constrained to pass through the data point at 350°C. I<sub>A</sub> represents the CO<sub>2</sub> linear peak intensity at 1388 cm<sup>-1</sup>, I<sub>B</sub> represents the H<sub>2</sub>O linear peak intensity at 3600cm<sup>-1</sup>.

Table 3.2. Raman spectral linear peak intensity ratios of H<sub>2</sub>O-CO<sub>2</sub> synthetic fluid inclusion standards collected at various temperatures.

<u>T(°C)</u>	<u>IR</u>	<u>Std Dev %</u>	<u># Spectra</u>
307	0.45	3.72	6
325	0.43	3.64	6
350	0.40	8.27	6
375	0.39	8.86	6
400	0.38	10.6	5
425	0.35	7.19	5
450	0.34	18.4	4

*IR* is the intensity ratio of the 1388 cm<sup>-1</sup> CO<sub>2</sub> peak divided by its sum with the intensity of the 3600 cm<sup>-1</sup> H<sub>2</sub>O band;

*T(°C)* is the analytical temperature;

*Std Dev* represents the standard deviation in percent

*# Spectra* is the number of spectra acquired at each analytical temperature.

As noted above, during the initial stages of this study various spectral parameters were tested to describe the relationship between fluid composition and Raman spectra. The intensity ratio determined at 350°C and described by equation (3.2) offered the best

reproducibility (smallest standard deviation) of all the parameters tested. However, as shown in Figure 3.4., this relationship should only be used if the inclusions are analyzed at 350°C. Conversely, the peak area ratio (AR), defined as the ratio of the area under the CO<sub>2</sub> Fermi diad (2ν<sub>2</sub>) peak at 1388 cm<sup>-1</sup> divided by the sum of the areas of the the 2ν<sub>2</sub> component of the Fermi diad and the O-H stretching vibration band of H<sub>2</sub>O at around 3600 cm<sup>-1</sup> (AR = A<sub>CO<sub>2</sub></sub> / (A<sub>CO<sub>2</sub></sub> + A<sub>H<sub>2</sub>O</sub>)) is independent of temperature over the range 307°C to 450°C (Fig. 3.5., Table 3.3). The peak area ratio has been calculated for each of the inclusions used in the calibration, and the results indicate the following linear relationship between peak area ratio and composition:

$$\text{Mole \% CO}_2 = 312.5 \text{ AR} \quad (3.5)$$

where AR is the peak area (integrated intensity) ratio defined above (Fig. 3.6, Table 3.4). Equation (3.5) is independent of temperature over the range from about 300°C to 450°C. However, the standard deviation is significantly larger (Fig. 3.6, Table 3.4) than that for equation (3.2), which describes the relationship between linear peak intensity and composition. We recommend that the linear peak intensity ratio and equation (3.2) be used to determine the compositions of H<sub>2</sub>O-CO<sub>2</sub> fluid inclusions if they can be analyzed at 350°C. If the analyses are conducted at some other temperature, equation (3.5) should be used, recognizing that the error in composition is likely to be greater than that obtained with equation (3.2). Also note that equation (3.5), relating peak area ratio and composition, should not be used for compositions greater than about 25 mole % CO<sub>2</sub> because the error becomes significant for higher CO<sub>2</sub> concentrations. Finally, we note that Burke (1994) suggests that CO<sub>2</sub> concentrations in fluid inclusions should be calculated based on the sum of the peak areas for both peaks of the CO<sub>2</sub> Fermi diad (2ν<sub>2</sub> at 1388 cm<sup>-1</sup> and ν<sub>1</sub> at 1285 cm<sup>-1</sup>). However, when both peaks of the Fermi diad were used here, the standard deviation was somewhat larger than that obtained using only the higher wave number peak at 1388 cm<sup>-1</sup>. That can be explained by the lower linear peak intensity of the ν<sub>1</sub> member of the Fermi diad and interference by the quartz peak at around 1160 cm<sup>-1</sup> which partially overlaps the 1265 cm<sup>-1</sup> gas phase ‘hot’ band attached to

the  $\nu_1$  member of the  $\text{CO}_2$  Fermi diad. For this reason, the calibration presented here includes only the area for the  $1388\text{ cm}^{-1}$  peak.

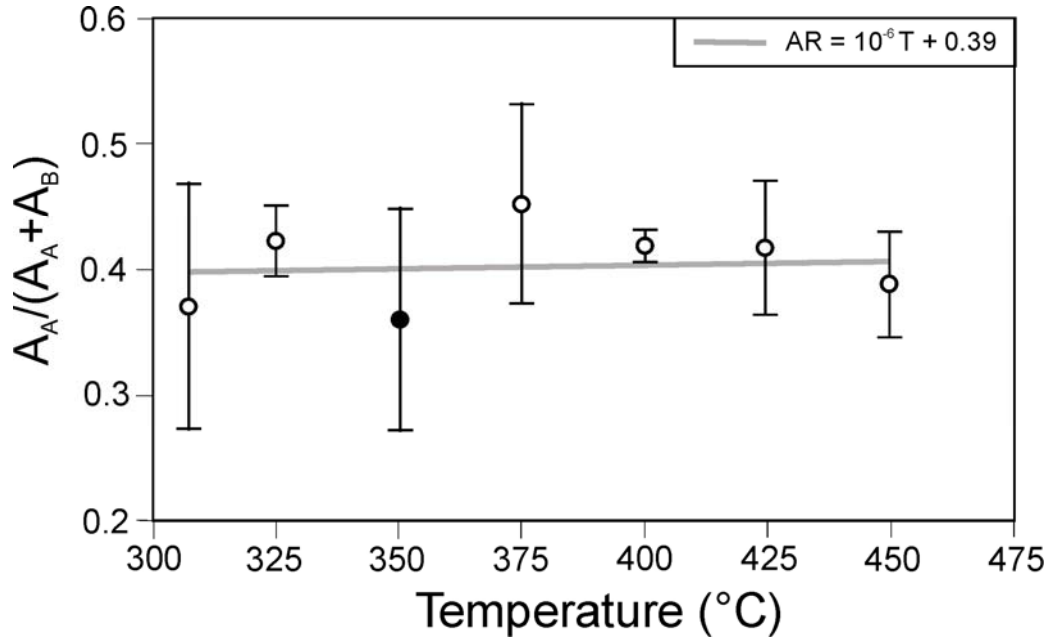


Figure 3.5. Raman peak area ratios of  $\text{CO}_2$ - $\text{H}_2\text{O}$  inclusions containing 12.5 mole %  $\text{CO}_2$  acquired at temperatures between  $307^\circ\text{C}$  and  $450^\circ\text{C}$ . Filled symbol at  $350^\circ\text{C}$  represents the integrated area ratio used in equation (5).  $A_A$  represents the  $\text{CO}_2$  peak area at  $1388\text{ cm}^{-1}$ ,  $A_B$  represents the  $\text{H}_2\text{O}$  peak area at  $3600\text{ cm}^{-1}$ .

In this study we have not included the effect of salinity in the calibration scheme. Our preliminary data obtained from synthetic fluid inclusions containing less than 5 wt% NaCl indicate that equations (3.2) and (3.5) are valid for low salinity inclusions (less than about 5 wt.% NaCl equivalent), and this is supported by the good agreement between  $\text{CO}_2$  concentrations of natural inclusions obtained with equation (3.2) and those determined independently based on microthermometric and petrographic observations (see below) (Table 3.5). A future study will investigate the relationship between salinity and Raman spectral parameters for  $\text{H}_2\text{O}$ - $\text{CO}_2$  “salt” fluid inclusions.

Table 3.3. Raman spectral peak area ratios of H<sub>2</sub>O-CO<sub>2</sub> synthetic fluid inclusion standards collected at various temperatures.

<u>T(°C)</u>	<u>AR</u>	<u>Std Dev %</u>	<u># Spectra</u>
307	0.0372	26.2	6
325	0.0423	6.51	6
350	0.0361	24.4	6
375	0.0452	17.6	6
400	0.0419	1.80	5
425	0.0418	12.8	5
450	0.0389	10.7	4

*AR* is the peak area ratio of the 1388 cm<sup>-1</sup> CO<sub>2</sub> peak divided by its sum with the intensity of the 3600 cm<sup>-1</sup> H<sub>2</sub>O band;

*T(°C)* is the analytical temperature;

*Std Dev* represents the standard deviation in percent

*# Spectra* is the number of spectra acquired at each analytical temperature.

Table 3.4. Raman spectral peak area ratios of H<sub>2</sub>O-CO<sub>2</sub> synthetic fluid inclusion standards.

<u>Mole % CO2</u>	<u>Th(°C)</u>	<u>AR</u>	<u>Std Dev %</u>	<u># Spectra</u>
2.5	305	0.0086	10.3	12
5	302	0.0166	10.6	12
10	302	0.0357	8.24	14
12.5	305	0.0409	21.0	6
17.5	309	0.0510	15.6	9
25	293	0.0842	22.5	8

*Th* is the average homogenization temperature of inclusions within a sample;

*AR* is the area ratio of the 1388 cm<sup>-1</sup> CO<sub>2</sub> peak divided by its sum with the intensity of the 3600 cm<sup>-1</sup> H<sub>2</sub>O band;

*Std Dev* represents the standard deviation in percent

*# Spectra* is the number of spectra acquired from each sample.

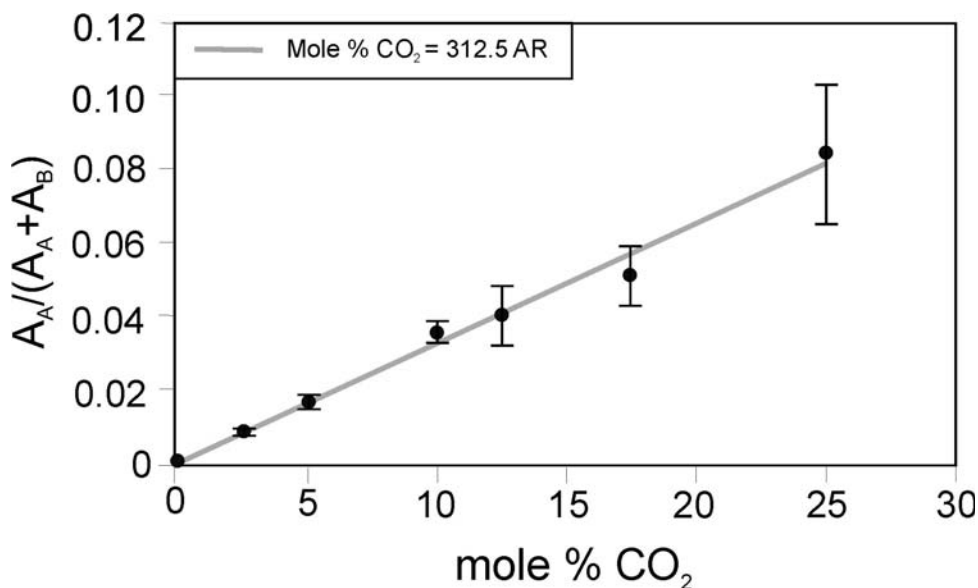


Figure 3.6. Relationship between the mole % CO<sub>2</sub> in H<sub>2</sub>O-CO<sub>2</sub> inclusions and Raman peak area ratios. A<sub>A</sub> represents the CO<sub>2</sub> linear peak intensity at 1388 cm<sup>-1</sup> and A<sub>B</sub> represents the H<sub>2</sub>O linear peak intensity at 3600cm<sup>-1</sup>. The calibration curve is extrapolated to 0 mole % CO<sub>2</sub>, however the lowest CO<sub>2</sub> concentration analyzed was 2.5 mole %.

#### III.4. Application to Natural Inclusions

The LRS method for estimating compositions of H<sub>2</sub>O-CO<sub>2</sub> inclusions has been applied to natural inclusions hosted in vein quartz from the Butte, Montana, porphyry copper-molybdenum deposit. Microthermometric data show that the inclusions trapped low salinity, magmatically derived CO<sub>2</sub>-bearing aqueous fluids (Rusk, 2003; Rusk et al., 2004). The CO<sub>2</sub> concentration of the inclusions (3.6 to 6.8 mole % CO<sub>2</sub>) was previously estimated by Rusk (2003) using the computer program ICE (Bakker, 1997) which calculates CO<sub>2</sub> content based on clathrate dissolution temperature and an estimate of vapor bubble volume. Low salinity (<5 wt.% NaCl equiv.), low homogenization temperature (<400°C) inclusions were selected for Raman analysis. Homogenization temperatures were measured before and after LRS analysis to test if leaking occurred during heating. The analyzed inclusions showed various modes of homogenization, with some homogenizing to liquid, others to vapor and some by critical behavior, suggesting

that the inclusions were trapped in the one-phase field at P-T conditions near the critical isochore (Cline and Bodnar, 1994).

Before heating, the vapor bubble in the inclusions was analyzed at room temperature to test for the presence of other volatiles. Over the range 1000-3860  $\text{cm}^{-1}$ , the only peaks that were observed (other than those for the host quartz) were those for  $\text{CO}_2$  at 1285  $\text{cm}^{-1}$  and 1388  $\text{cm}^{-1}$ . Fifteen homogenized fluid inclusions were analyzed at 350°C using the same instrumental settings as were used for calibration. The calculated  $\text{CO}_2$  contents of the inclusions range from below the detection limit (~1 mole %  $\text{CO}_2$ ) to 4.2 mole %  $\text{CO}_2$  (Table 3.5). These results are consistent with results presented previously by Rusk (2003) and suggest that the calibration equation obtained for pure  $\text{H}_2\text{O}-\text{CO}_2$  inclusions can be applied to inclusions with salinities less than 5 wt.% NaCl equivalent.

Table 3.5. Compositions of  $\text{H}_2\text{O}-\text{CO}_2$  inclusions from Butte, Montana.

<u>Sample</u>	<u>Th(°C)</u>	<u>IR</u>	<u>Mole % CO2</u>
11172-4187	338	0.11	2.50
	319	0.16	3.89
	342	0.07	1.93
	348	0.16	4.23
	320	0.14	3.63
	347	0.13	3.23
	347	0.09	2.30
	335	0.06	1.77

*Th* is the homogenization temperature of individual inclusions;  
*IR* is the intensity ratio of the 1388  $\text{cm}^{-1}$   $\text{CO}_2$  peak divided by its sum with the intensity of the 3600  $\text{cm}^{-1}$   $\text{H}_2\text{O}$  band.

### III.5. Conclusions

A Laser Raman Spectroscopic technique has been developed for quantitative analysis of H<sub>2</sub>O-CO<sub>2</sub> fluid inclusions. Calibration was based on the relationship between the known CO<sub>2</sub> concentration in the inclusions and the intensity of the 1388 cm<sup>-1</sup> CO<sub>2</sub> peak divided by its sum with the intensity of the 3600 cm<sup>-1</sup> H<sub>2</sub>O peak. The relationship is valid for compositions ranging from 2.5 to 50 mole % CO<sub>2</sub>. The intensity ratio (IR) is a negative function of temperature – thus the equation is only valid at 350°C.

The relationship between composition of H<sub>2</sub>O-CO<sub>2</sub> inclusions and peak area ratios has also been tested. Results show a positive linear relationship between the peak area ratio and composition. The standard deviation of the peak area ratio – composition relationship is larger than that based on intensity ratios and increases with increasing CO<sub>2</sub> content. Thus, it should only be applied to inclusions containing  $\leq 25$  mole % CO<sub>2</sub>. Based on preliminary results, the peak area relationship is independent of temperature over the range 307°C to 450°C, and can be used to determine compositions of inclusions that homogenize (without decrepitating) below 450°C.

The technique has not been tested for inclusions containing >50 mole% CO<sub>2</sub> but there is no reason to expect that the technique could not be applied to extend the calibration equation to more CO<sub>2</sub>-rich compositions. One should also note that the quantitative relations presented in this study are only valid for low salinity (< 5 weight percent) inclusions. Understanding the effect of salt on the relationship between CO<sub>2</sub> content and Raman spectra is the topic of an ongoing study.

The quantitative LRS method has been applied to natural low salinity H<sub>2</sub>O-CO<sub>2</sub> inclusions from the Butte porphyry copper-molybdenum deposit. The estimated compositions, ranging from 0 to 4.2 mole % CO<sub>2</sub>, are consistent with CO<sub>2</sub> concentrations based on microthermometric and petrographic analyses.

### III.6. Acknowledgements

The authors thank Charles Farley for technical assistance with Raman analyses. Andras Fall, Claudia Cannatelli and Bebe Oh provided valuable technical and editorial suggestions. Reviews of an earlier version of this paper by Fons Van den Kerkhof and Jean Dubessy highlighted several inconsistencies and significantly improved the final product. Funding for this project was provided by NSF grants EAR0125918 and EAR-0322119 to R. J. Bodnar.

Sample preparation and calibration of the analytical instrument has been carried out by Tristan Azbej. Laser Raman spectra were collected, processed and interpreted by Matthew Severs and Tristan Azbej.

### III.7. References

- Adar, F., Naudin, C., Whitley, A., Bodnar, R.J., 2004. Use of a microscope objective corrected for a cover glass to improve confocal spatial resolution inside a sample with a finite index of refraction. *Appl. Spectrosc.* 58, 1136-1137.
- Anderson, G.R., The Raman spectra of carbon dioxide in liquid H<sub>2</sub>O and D<sub>2</sub>O. *J. Phys. Chem.* 81, 3, 273-276.
- Bakker, R.J., 1997. Clathrates: Computer programs to calculate fluid inclusion V-X properties using clathrate melting temperatures: *Computers and Geosciences* 23, 1, 1-18.
- Bodnar, R.J., 2003. Reequilibration of fluid inclusions. *In* I. Samson, A. Anderson, and D. Marshall, eds. *Fluid Inclusions: Analysis and Interpretation. Mineral. Assoc. Canada, Short Course* 32, 213-230.
- Bodnar, R.J., Binns, P.R., Hall, D.L., 1989. Synthetic fluid inclusions VI. Quantitative evaluation of the decrepitation behavior of fluid inclusions in quartz at one atmosphere confining pressure. *Journal of Metamorphic Geology*, 7, 229-242.
- Bodnar, R.J., Costain, J.K., 1991. Effect of fluid composition on mass and energy transport in the earth's crust. *Geophys. Res. Letters*, 18, 983-986.

- Bodnar, R.J., Reynolds, T.J., Kuehn, C.A., 1985. Fluid inclusion systematics in epithermal systems. *in* Society of Economic Geologists, Reviews in Economic Geology, 2, Geology and Geochemistry of Epithermal Systems, B.R. Berger and P.M. Bethke, (Eds.), 73-98.
- Bodnar, R.J., Sterner, S.M., 1987. Synthetic fluid inclusions. *in* Hydrothermal Experimental Techniques, G.C. Ulmer and H.L. Barnes, (Eds.), Wiley-Interscience, New York. p.423-457.
- Bodnar, R.J., Szabo, Cs., Shilobreeva, S.N., Newman, S., 1996. Quantitative Analysis of H<sub>2</sub>O-CO<sub>2</sub> Fluid Inclusions by Raman Spectroscopy. Program and Abstracts, Sixth biennial Pan American Conference on Research on Fluid Inclusions. 14.
- Burke, E.A.J., 1994. Raman microspectrometry of fluid inclusions: The daily practice. *in* Fluid Inclusions in Minerals, Methods and Applications, B. De Vivo and M. L. Frezzotti, eds., pub. by Virginia Tech, Blacksburg, VA, p. 25-44.
- Chou, I., 1986. Permeability of precious metals to hydrogen at 2 kb total pressure and elevated temperatures. *Amer. J. Sci.* 286, 8, 638-658.
- Cline, J.S., Bodnar, R.J., 1994. Direct evolution of a brine from a crystallizing silicic melt at the Questa, New Mexico, molybdenum deposit. *Econ. Geol.* 89, 1780-1802.
- Davis, A.R., Oliver, B.G., 1972. A vibrational-spectroscopic study of the species present in the CO<sub>2</sub>-H<sub>2</sub>O system. *J. Sol. Chem.* 1, 4, 329-339.
- Diamond, L.W., 2003. Introduction to gas-bearing aqueous fluid inclusions. *In* I. Samson, A. Anderson, and D. Marshall, eds. Fluid Inclusions: Analysis and Interpretation. *Mineral. Assoc. Canada, Short Course* 32, 101-159.
- Dickinson, R.G., Dillon R.T., Rasetti, F., 1929. Raman spectra of polyatomic gases. *Phys. Rev.* 24, 582-589.
- Dubessy, J., Poty, B., Ramboz, C., 1989. Advances in C-O-H-N-S fluid geochemistry based on micro-Raman spectrometric analysis of fluid inclusions. *Eur. J. Miner.* 1, 517-534.
- Dubessy, J., Moissette, A., Bakker, R.J., Frantz, J.D., Zhang, Y.G., 1999. High temperature Raman spectroscopic study of H<sub>2</sub>O-CO<sub>2</sub>-CH<sub>4</sub> mixtures in synthetic fluid inclusions; first insights on molecular interactions and analytical implications. *Eur. J. Miner.* 11, 1, 23-32.

- Dubessy, J., Buschaert, S., Lamb, W., Pironon, J., Thiery, R., 2001. Methane-bearing aqueous fluid inclusions: Raman analysis, thermodynamic modeling and applications to petroleum basins. *Chem. Geol.* 173, 193-205.
- Franck, E.V., Todheide, K., 1959. Thermal properties of super critical mixtures of CO<sub>2</sub> and H<sub>2</sub>O to 750 and 2000 atm. *Zeits. Phys. Chem. Neue Folge.* 22, 232-245.
- Herzberg, G., 1945. *Infrared and Raman Spectra.* Van Nostrand-Reinhold, New York, NY. p. 272.
- Leng, J., Sharma, A., Bodnar, R.J., Pottorf, R.J., Vityk, M.O., 1998. Quantitative analysis of synthetic fluid inclusions in the H<sub>2</sub>O-CH<sub>4</sub> system using Raman spectroscopy. PACROFI VII; Pan-American conference on Research on fluid inclusions; program and abstracts. 7, 44.
- Leroy, J., 1979. Contribution a l'etalonnage de la pression interne des inclusions fluides lors de leur decrepitation. Gauging the internal pressure of fluid inclusions during decrepitation. *Bull. de Min.* 102, 5-6, 584-593.
- Linnen, R.L., Keppler, H., Sterner, S.M., 2004. In situ measurements of the H<sub>2</sub>O:CO<sub>2</sub> ratio in fluid inclusions by infrared spectroscopy. *Canadian Mineralogist*, 42, 1275-12828.
- Mavrogenes, J.A., Bodnar, R.J., 1994. Hydrogen movement into and out of fluid inclusions in quartz; experimental evidence and geologic implications. *Geochim. Cosmochim.* 58, 1, 141-148.
- Nambu, M., Takeshi, M., Nakatsuko, K., 1990. Quantitative analysis of CO<sub>2</sub> / H<sub>2</sub>O ratios in fluid inclusions using FTIR. Program and Abstracts; Biennial Pan American conference on Research on fluid inclusions. 3, 64.
- Pasteris, J.D., Wopenka, B., Seitz, J.C., 1988. Practical aspects of quantitative laser Raman microprobe spectroscopy for the study of fluid inclusions. *Geochim. Cosmochim.* 52, 5, 979-998.
- Pironon, J., Grimmer, J.O.W., Teinturier, S., Guillaume, D., Dubessy, J., 2003. Dissolved methane in water; temperature effect on Raman quantification in fluid inclusions. *J. Geochemical Exploration*, 78-79, 2003, 111-115.
- Roedder, E., 1984. Fluid inclusions. *Reviews in Mineralogy.* 12, 664pp.

- Rosso, K.M., Bodnar, R.J., 1995. Detection limits of CO<sub>2</sub> in fluid inclusions using microthermometry and laser Raman spectroscopy and the spectroscopic characterization of CO<sub>2</sub>. *Geochim. Cosmochim.* 59, 19, 3961-3975.
- Rusk, B.G., 2003. Cathodoluminescent quartz textures and fluid inclusions in veins of the porphyry copper-molybdenum deposit in Butte, Montana: Constraints on physical and chemical evolution of the hydrothermal system. PhD Dissertation. University of Oregon. 235 pp.
- Rusk, B.G., Reed, M.H., Dilles, J.H., Klemm, L.M., Heinrich, C.A., 2004. Compositions of magmatic hydrothermal fluids determined by LA-ICP-MS of fluid inclusions from the porphyry copper-molybdenum deposit at Butte, MT. *Chem. Geol.* 210, 173-199.
- Schröter, H.W., Kienner, H.W., 1979. Raman scattering cross-sections in gases and liquids. *In* Weber, A., ed., *Raman spectroscopy of gases and liquids*. Berlin, Springer-Verlag, 123-166.
- Seitz, J.C., Pasteris, J.D., Morgan, G.B., 1992. Cautionary note on analytical methodology for quantitative analysis of CO<sub>2</sub>-CH<sub>4</sub>-N<sub>2</sub>-H<sub>2</sub> fluids by microsampling Raman spectroscopy. Program and Abstracts; Biennial PanAmerican conference on Research on fluid inclusions. 4, 72.
- Seitz, J.C., Pasteris, J.D., Chou, I.M., 1993. Raman spectroscopic characterization of gas mixtures; I. Quantitative composition and pressure determination of CH<sub>4</sub>, N<sub>2</sub> and their mixtures. *Am. J. Sci.* 293, 4, 297-321.
- Seitz, J.C., Pasteris, J.D., Chou, I.M., 1996. Raman spectroscopic characterization of gas mixtures; II. Quantitative composition and pressure determination of the CO<sub>2</sub>-CH<sub>4</sub> system. *Am. J. Sci.* 296, 6, 577-600.
- Shuling, L., 1998. Study on Raman spectroscopy of CO<sub>2</sub>-H<sub>2</sub>O system. *Yankuang Ceshi = Rock and Mineral Analysis.* 17, 3, 177-180.
- Sterner, S.M., Bodnar, R.J., 1984. Synthetic fluid inclusions in natural quartz. I. Compositional types synthesized and applications to experimental geochemistry. *Geochim. Cosmochim. Acta*, 48, 2659-2668.

- Sterner, S.M., Bodnar, R.J., 1991. Synthetic fluid inclusions; X, Experimental determination of P-V-T-X properties in the CO<sub>2</sub>-H<sub>2</sub>O system to 6 kb and 700 degrees C. *Am. J. Sci.* 291, 1, 1-54.
- Takenouchi, S., Kennedy, G.C., 1964. The binary system H<sub>2</sub>O-CO<sub>2</sub> at high temperatures and pressures. *Am. J. Sci.* 262, 1055-1074.
- Wopenka, B., Pasteris, J.D., 1986. Limitations to quantitative analysis of fluid inclusions in geological samples by laser Raman microprobe spectroscopy. *Appl. Spectrosc.* 24, 2, 144-151.

## **CHAPTER IV. Experimental determination of H<sub>2</sub>O loss from melt inclusions during laboratory heating**

*Co-authored chapter: Matthew J. Severs, Tristan Azbej*

### **IV.1. Introduction**

Volatile components play an important role in eruptive behavior of volcanic systems (Sparks et al., 1994) and formation of magmatic-hydrothermal ore deposits (Burnham, 1979; 1997; Bodnar, 1995). Water is usually the most abundant volatile in silicic magmas (McMillan, 1994), and influences the location of the liquidus and solidus as well as the viscosity and density of the melt (Lange, 1994). As such, a complete understanding of the evolution of a magmatic system requires information on the H<sub>2</sub>O content of the melt during crystallization. Melt inclusions provide the best samples for determining pre-eruptive volatile contents in silicate melts (i.e., Lowenstern, 1995; Student and Bodnar, 1996; 2004).

The use of melt inclusions to study magmatic processes is based on the assumption that the inclusions represent the melt present at the time of trapping, and that nothing has been added to or lost from the inclusion since trapping (Roedder, 1984; Bodnar, 2003a; Bodnar & Student, 2006). However, several authors have suggested that H<sub>2</sub>O may diffuse out of melt inclusions if the sample is maintained at elevated temperatures for extended periods of time during homogenization experiments in the lab (Qin et al., 1992; Massare et al., 1998; Massare et al., 2002), similar to observations associated with aqueous inclusions (Vityk et al., 2000; Bodnar, 2003b). Other workers have documented the reequilibration of melt inclusions in olivine by loss of iron during prolonged heating in the laboratory (Danyushevsky et al., 2000). In this study, the loss of H<sub>2</sub>O from melt inclusions during laboratory heating was investigated using quartz-hosted melt inclusions from the early-erupted plinian phase of the Bishop Tuff. Inclusions with “known” H<sub>2</sub>O contents were maintained at 800°C and 1 kbar for varying lengths of time, and the H<sub>2</sub>O content of the inclusions after heating was determined by Raman spectroscopy. To minimize analytical problems associated with fluorescence, the

inclusions were analyzed using UV excitation (244 nm), and the results were compared to analyses using visible (514 nm) excitation.

## **IV.2. Raman Spectra of Hydrous Glass**

Raman spectroscopy has recently been applied to determine H<sub>2</sub>O contents of glasses and melt inclusions (Thomas, 2000; Thomas et al., 2002; Chabiron et al., 2004; Zajacz et al., 2005; Thomas et al., 2006; Di Muro et al., 2006). Raman spectroscopy is non-destructive, requires minimal sample preparation, and can be used to analyze both exposed and unexposed inclusions as small as 5  $\mu\text{m}$ . The intensity of the Raman peak is directly proportional to H<sub>2</sub>O concentration and is independent of the composition of the glass (Thomas, 2000). The Raman spectrum of silicate glass shows two major bands in the low-wavenumber region, at approximately 490  $\text{cm}^{-1}$  and 1050  $\text{cm}^{-1}$  when analyzed with visible (488 nm or 514 nm) excitation (Fig. 4.1A). The broad band at 490  $\text{cm}^{-1}$  is attributed to symmetric stretching of the oxygen bond in the tetrahedra-oxygen-tetrahedra (T-O-T) structure (Matson et al., 1983; Sharma et al., 1997). In completely polymerized alkali-feldspar melts (i.e., containing no non-bridging oxygens) the broad band at 1050  $\text{cm}^{-1}$  represents an asymmetric stretching vibration in the T-O-T links that produces a doublet with distinct bands at 1020  $\text{cm}^{-1}$  and 1105  $\text{cm}^{-1}$  (McMillan et al., 1982; McMillan et al., 1992; Mysen, 1997; Sharma et al., 1997; Mysen, 1999). A decrease in the degree of polymerization, or the addition of Fe, results in the appearance of new Raman bands which represent stretching modes between the different structural species present (McMillan et al., 1982; Wang et al., 1993; Mysen, 1997; 1999; Sharma et al., 1997). The 586  $\text{cm}^{-1}$  band is attributed to defects (Seifert et al., 1981; McMillan and Wolf, 1995) while the 776  $\text{cm}^{-1}$  band has been assigned to T-O-T bending vibrations (Chabiron et al., 2004).

Thomas (2000), Thomas et al. (2002) and Chabiron et al. (2004) derived linear correlations between the total H<sub>2</sub>O content of feldspar glasses and the ratio relating the integrated sum of the H<sub>2</sub>O-OH band at around 3550  $\text{cm}^{-1}$  and the integral area of the asymmetric T-O band at about 490  $\text{cm}^{-1}$ . Integrated ratios are used rather than peak intensities because this method eliminates short time fluctuations and the need for

multiple calibrations due to long-term instability of the laser (Thomas, 2000). Thomas (2002a) expanded the compositional range to include basaltic, andesitic, and phonolitic compositions. Zajacz et al. (2005) used a slightly different method and related the H<sub>2</sub>O content to the ratio of the 3550 cm<sup>-1</sup> peak area and the area under the broad T-O and T-O-T vibrational bands between 850 cm<sup>-1</sup> and 1250 cm<sup>-1</sup>.

All of the above mentioned studies used a visible wavelength laser (either 514 nm or 488 nm) as the excitation source. While these are the most commonly available laser sources for Raman analysis, visible excitation wavelengths limit the applicability of the Raman technique to determine H<sub>2</sub>O contents of glasses and melt inclusions because many samples fluoresce when excited at these wavelengths (Fig. 4.2). Some samples only fluoresce after heating in the laboratory (R. Thomas, pers. comm.) while others such as the Macusani glass fluoresce naturally. Fluorescence following heating is thought to be the result of changes in the oxidation state of trace elements present in the melt (Thomas, 2000). The fluorescence intensity generally increases with increasing distance from the Rayleigh line (i.e., at higher wavenumbers) and precludes an accurate determination of peak areas, especially the H<sub>2</sub>O peak located near 3550 cm<sup>-1</sup>. The fluorescence is likely caused by trace elements in the glass or by defects in the crystal lattice (Chabiron et al., 2004). To minimize fluorescence interference in the present study, the relationship between H<sub>2</sub>O content and Raman signal was determined using a 224 nm (ultraviolet) laser. This new calibration relationship was then used to monitor H<sub>2</sub>O loss from melt inclusions during laboratory heating.

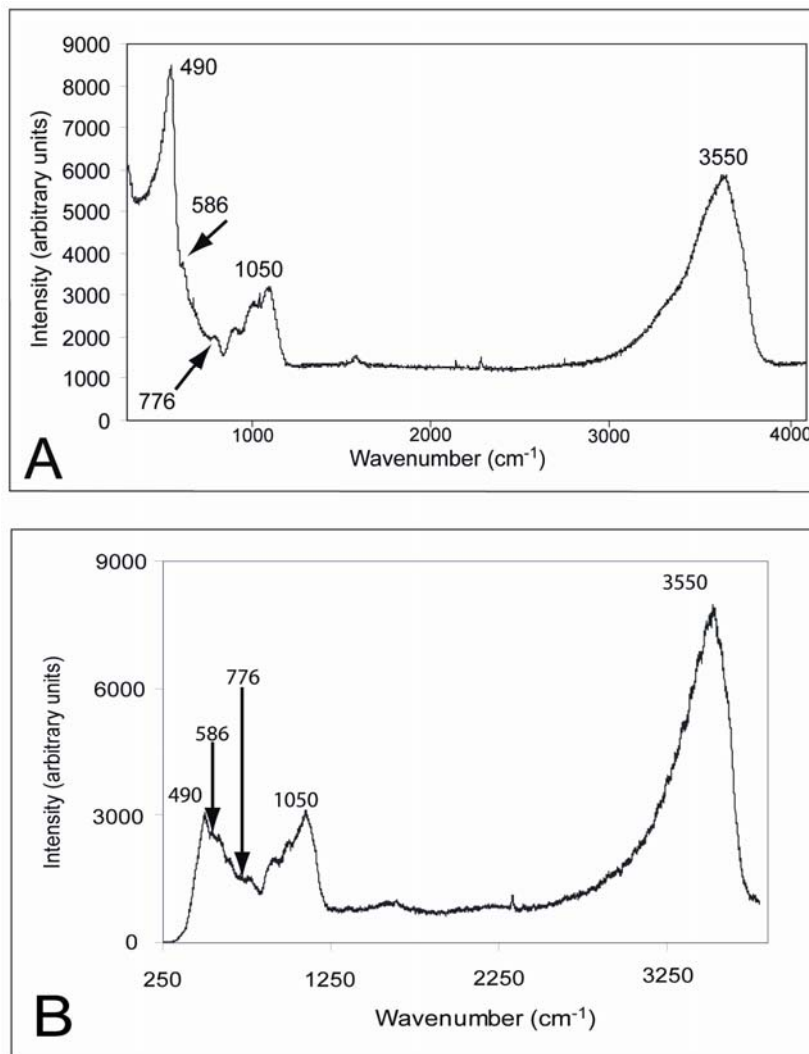


Figure 4.1. A) Raman spectrum (after frequency-temperature correction) of alkali feldspar glass containing 4.93 wt% H<sub>2</sub>O produced using 514nm (green) excitation. Labeled bands are the T-O-T bending vibrational mode (490 cm<sup>-1</sup>), glass defect peak (586 cm<sup>-1</sup>), T-O-T bending mode (776 cm<sup>-1</sup>) and a broad peak from 850-1250 cm<sup>-1</sup> and centered at about 1050 cm<sup>-1</sup> that represents T-O and T-O-T bending and stretching modes. The 3550 cm<sup>-1</sup> band represents molecular water and hydroxyl groups in the glass. B) Raman spectrum (after frequency-temperature correction) of alkali feldspar glass standard containing 4.93 wt% water analyzed with 244nm ultraviolet excitation. Note the relative intensities of the 490 cm<sup>-1</sup>, 586 cm<sup>-1</sup>, and 776 cm<sup>-1</sup> bands differ from those produced using visible excitation. The broad T-O-T band centered at 1050 cm<sup>-1</sup> and the water band at 3550 cm<sup>-1</sup> are similar to bands in the visible spectrum (Fig.4.1A).

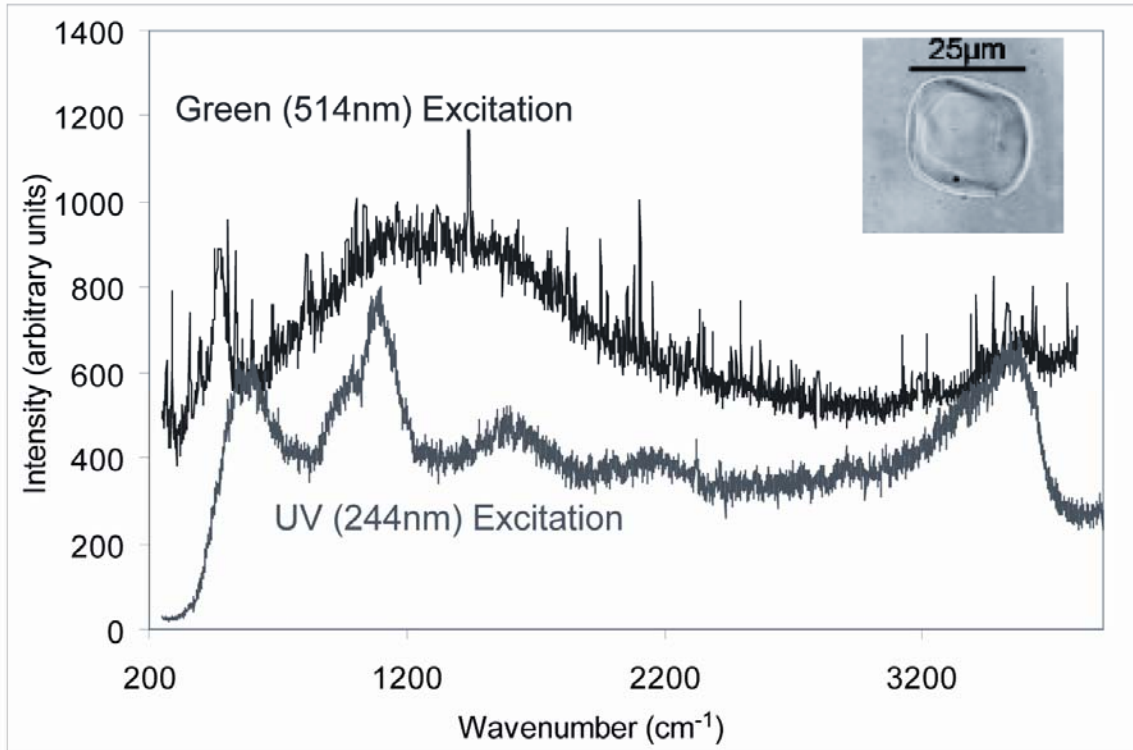


Figure 4.2. Comparison of Raman spectra of a melt inclusion (inset) in quartz from the Bishop Tuff obtained using visible (514nm) and ultraviolet (244nm) excitation. The fluorescence intensity in the spectrum obtained with visible excitation masks several of the Raman bands and precludes an accurate determination of the peak areas.

Spectra generated with UV excitation are similar to those obtained with visible (green) excitation, with a few significant exceptions (Fig. 4.1B). The  $490\text{ cm}^{-1}$  band becomes broader and less distinct, compared to the sharp, narrow band produced using visible excitation wavelengths. The broadening suggests that UV excitation results in stronger T-O-T bending signals at  $586\text{ cm}^{-1}$  and  $776\text{ cm}^{-1}$  that interfere with the  $490\text{ cm}^{-1}$  signal. Similar differences between UV-excitation spectra and those generated by visible wavelength lasers have been noted for biological samples (Smith and Dent, 2005).

### IV.3. Calibration of the Raman spectra

#### IV.3.1. Calibration standards and instrumentation

Many unheated melt inclusions in the Bishop Tuff fluoresce under visible wavelength excitation (Fig. 4.2). As such, the first step in this study to examine H<sub>2</sub>O loss from the melt inclusions during laboratory heating was to calibrate the Raman microprobe using UV (244 nm) excitation to minimize fluorescence interference.

Synthetic glasses containing between 0.95 and 9.5 wt% H<sub>2</sub>O were used for the calibration. Twelve of the standards have compositions in the (Na,K)AlSi<sub>3</sub>O<sub>8</sub> system and were prepared to determine the solubility of H<sub>2</sub>O in alkali feldspar melts at 900°C and 5 kbars (Voigt et al., 1981). Four additional samples with andesitic composition were also used (Mandeville et al., 2002). The H<sub>2</sub>O contents of these latter samples were confirmed through Karl-Fisher titration and FTIR analysis.

Raman spectra were collected on a JY Horiba Labram HR800UV confocal Raman microprobe equipped with a 2400 groove/mm grating, and an Olympus optical microscope and a 40X UV-specific objective. Raman scattering is detected with a Symphony liquid-nitrogen cooled CCD detector. A Lexel-85 244 nm UV laser excited the sample. Acquisition times of 60 seconds were used for glass standards containing >2 wt% H<sub>2</sub>O, and acquisition time was increased to 180 seconds for samples containing less than 2 wt% to improve the signal-to-background ratios. Three accumulations were obtained for each analysis to identify and eliminate cosmic spikes. The lower wavenumber region ( $\approx 200 - 1750 \text{ cm}^{-1}$ ) was analyzed first, followed by the higher wavenumber region ( $\approx 1750 - 3900 \text{ cm}^{-1}$ ). The maximum intensity was obtained when the laser was focused approximately 10  $\mu\text{m}$  below the surface of the sample. The confocal hole was set at 400  $\mu\text{m}$  for the glass standard analysis.

For comparison, the standards were also analyzed using a JY Horiba Labram HR800 confocal Raman microprobe equipped with a 514.57 nm Laserphysics Reliant laser, an Olympus microscope with a 50X objective, and an Andor electronically cooled CCD detector. Acquisition times and number of accumulations were the same as for the ultraviolet excitation reported above.

### IV.3.2 Spectral treatment

Raman spectra obtained using visible and UV excitation were treated in three steps using Labspec and Origin 7.5 software, as suggested by Zajacz et al. (2005). The first step involved baseline removal, followed by a frequency-temperature correction and, finally, band integration (Fig. 4.4.). Linear baseline corrections were applied to the 3550  $\text{cm}^{-1}$  band and the broad 1050  $\text{cm}^{-1}$  band. The 3550  $\text{cm}^{-1}$  baseline extended from approximately 3900 to 1250  $\text{cm}^{-1}$ , and the 1050  $\text{cm}^{-1}$  baseline extended from approximately 1250 to 850  $\text{cm}^{-1}$  (Fig. 3A). A third baseline correction was applied from 850  $\text{cm}^{-1}$  to the lowest wavenumbers recorded ( $\approx 200 \text{ cm}^{-1}$ ). The high shoulder that appears on the 490  $\text{cm}^{-1}$  band obtained with the visible excitation (Fig. 4.1A) and the less-well defined 490  $\text{cm}^{-1}$  band obtained with the UV excitation result in a less precise baseline correction at lower wavenumbers compared to higher wavenumbers.

After the baseline correction to eliminate background noise, a frequency-temperature intensity correction was applied (McMillan and Wolf, 1995; Keresztury, 2002; Long, 2002; Zajacz et al., 2005), as given by the equation:

$$I_{corr}^{Stokes} = I_{obs}^{Stokes} \frac{\nu(1 - e^{-\frac{h\nu}{kT}})}{\nu^* - \nu^4}$$

where  $\nu^*$  is the frequency of the incident laser light [either  $7.31512 \times 10^{19} \text{ Hz}$  (244 nm) or  $1.54097 \times 10^{20} \text{ Hz}$  (514 nm)],  $\nu$  is the frequency of the Raman-scattered light,  $h$  is Planck's constant,  $k$  is the Boltzmann constant, and  $T$  is the temperature of the analysis in Kelvin. The correction accounts for the decreasing efficiency of Raman scattering with higher wavenumbers and eliminates the shoulder on the 490  $\text{cm}^{-1}$  peak. This correction produces spectra that are less compositionally dependent (Zajacz et al., 2005). A separate frequency-temperature intensity correction was required for the visible and UV spectra because the magnitude of the correction is excitation wavelength-dependent.

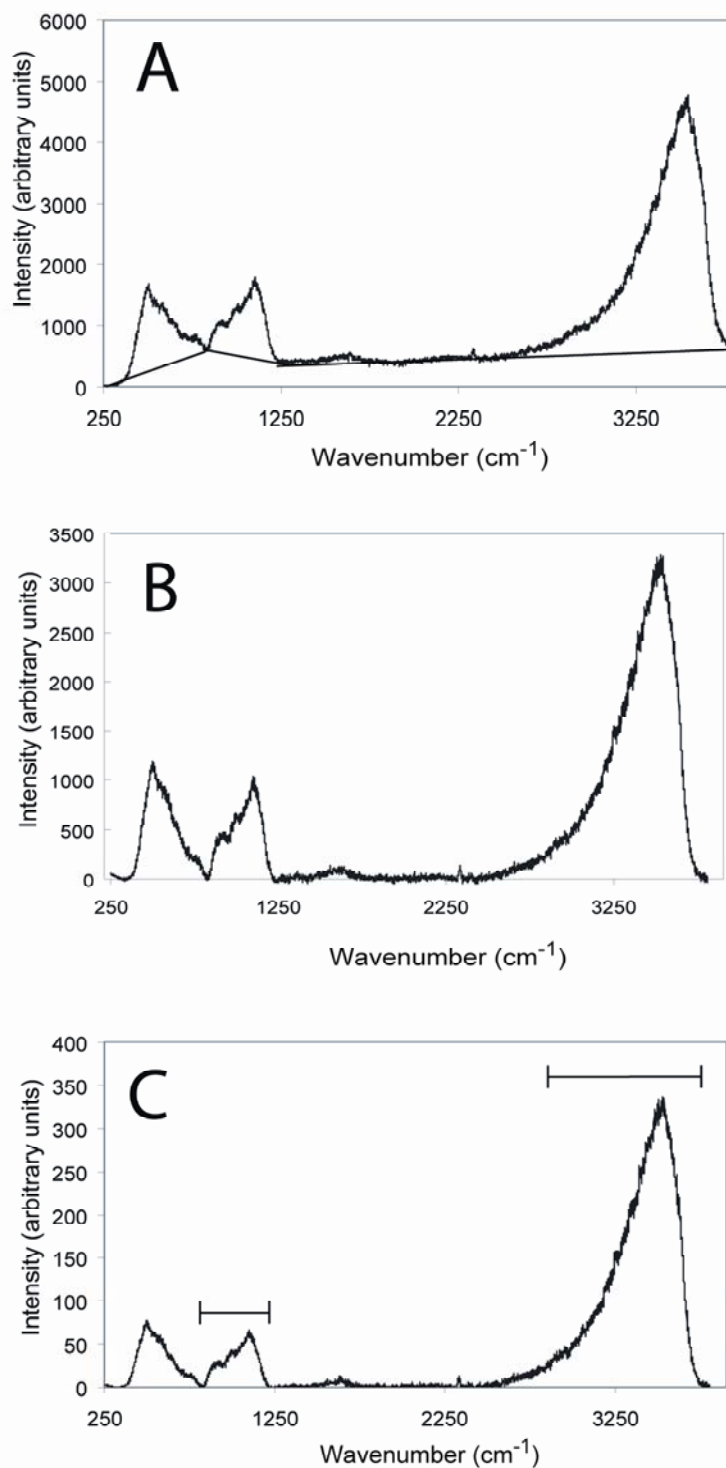


Figure 4.3. Summary of the procedures used to treat Raman spectra obtained on hydrous glasses. A) The original spectrum showing the baseline correction. B) Spectrum after the baseline has been removed. C) The spectrum after the frequency-temperature correction was applied. The horizontal lines in (C) indicate the range of wavenumbers over which peak area integrations were performed.

Following the baseline and frequency-temperature corrections, the areas under the 1050  $\text{cm}^{-1}$  and at 3550  $\text{cm}^{-1}$  peaks were determined. The first peak was integrated from 835 to 1225  $\text{cm}^{-1}$ , and the second peak was integrated from 2850 to 3750  $\text{cm}^{-1}$  (Fig 4.3C). The peak area ratio was determined by dividing the total  $\text{H}_2\text{O}$  peak area at 3550  $\text{cm}^{-1}$  by the T-O-T 1050  $\text{cm}^{-1}$  peak area. Some caution must be used when using the T-O-T 1050  $\text{cm}^{-1}$  peak area because this band can contain important hydroxyl components, such as B-OH, Al-OH, and Si-OH (Holtz et al., 1996; Thomas, 2002b). However, for simple compositions (such as the Bishop Tuff melt inclusions; Dunbar and Hervig, 1992; Anderson et al, 2000) and low total  $\text{H}_2\text{O}$  concentrations, ignoring these contributions introduces minimal errors. The T-O 490  $\text{cm}^{-1}$  peak was not used for the UV calibration because the goal was to compare the calibration results for visible and UV, and the 490  $\text{cm}^{-1}$  peak becomes broader and less distinct and more difficult to quantify when UV excitation is used. For each set of calibration data, the 3550  $\text{cm}^{-1}$ /1050  $\text{cm}^{-1}$  peak area ratio was related to the  $\text{H}_2\text{O}$  content (Fig. 4.4.).

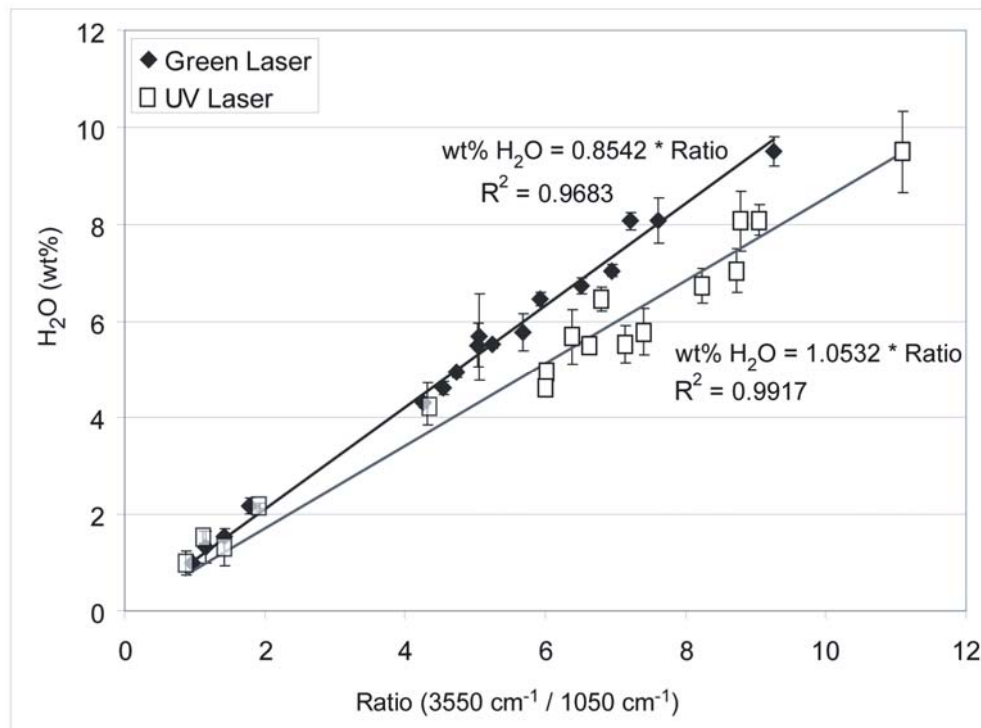


Figure 4.4. Relationship between the amount of water in hydrous glass and the ratio between the water peak area at 3550  $\text{cm}^{-1}$  and the T-O-T peak area band centered at 1050  $\text{cm}^{-1}$ . Each data point represents the average of at least 10 analyses and includes  $2\sigma$  error bars.

Analytical precision was tested by conducting repeated analyses of the same spot on the glass standard containing 4.93 wt% H<sub>2</sub>O. The same spot ( $\pm 10 \mu\text{m}$ ) was also analyzed daily for 3 days to examine variations over time. The calculated standard deviation is  $\pm 0.1$  wt% H<sub>2</sub>O using visible excitation, and  $\pm 0.2$  wt% H<sub>2</sub>O with UV excitation. The slightly higher standard deviation using UV excitation is due to the slightly higher overall background in the UV spectra compared to those obtained with 514 nm excitation.

The calibration results for both the UV and visible excitation are shown in Figure 4.4. The analytical data were fit to straight lines, with both lines constrained to pass through the origin because spectra of a sample with no H<sub>2</sub>O do not show a 3550 cm<sup>-1</sup> peak. The two calibration lines show different slopes as is expected owing to differences in the UV and visible spectra shown in Figures 4.1A and 4.1B. The results confirm the observations of Thomas (2000), Thomas et al. (2002), Chabiron et al. (2004), and Zajacz et al. (2005) that indicate a systematic relationship between H<sub>2</sub>O contents of silicate glasses and Raman intensities. However, the specific relationship between H<sub>2</sub>O content and Raman intensity varies from one instrument to the next, as has been shown previously by Pasteris et al. (1988) for aqueous inclusions. The UV calibration results show more scatter compared to those obtained with the visible laser, owing to the slightly higher background for the UV spectra. This higher background is believed to be instrument derived and not a result of fluorescence from the inclusions. Most of the fluorescence interference associated with visible excitation wavelengths is eliminated in the UV spectra (Fig. 4.2.).

## IV.4. Water loss from melt inclusions

### *IV.4.1 Experimental and analytical techniques*

In order to monitor H<sub>2</sub>O loss from melt inclusions during laboratory heating, melt inclusions with a known initial H<sub>2</sub>O content are required. One potential source is synthetic melt inclusions. Student and Bodnar (1999) trapped synthetic melt inclusions containing 5.5 wt% H<sub>2</sub>O, but the inclusions were small, tabular (rather than equant like most natural melt inclusions) and difficult to synthesize. Additionally, the quartz host surrounding the synthetic inclusions contains a high density of dislocations, allowing H<sub>2</sub>O to move more easily into (or out of) the inclusions compared to natural samples (Vityk et al, 2000).

In this study, natural melt inclusions from the Bishop Tuff in California, USA, were selected to monitor H<sub>2</sub>O loss from inclusions during laboratory heating. The early-erupted plinian phase of the Bishop Tuff contains melt inclusions that show relatively little variation in H<sub>2</sub>O content, with an average of about 5.5 wt% H<sub>2</sub>O (Skirius et al., 1990; Dunbar and Hervig, 1992; Wallace et al., 1999; Anderson et al., 2000; Wallace et al., 2003).

Quartz phenocrysts were separated from the Bishop Tuff by crushing and flotation. Several hundred crystals were loaded into a ≈3 cm long platinum capsule, and the open end was crimped (but not welded). The capsules were placed into a TZM furnace at 800° C and pressurized to 1 kbar using argon gas. Individual run durations were 4 hours, 12 hours, 24 hours, 2 days, 3 days, 7 days, 28 days, 54 days, and 63 days. After each run, the crystals were removed from the capsules and examined to identify quartz crystals containing melt inclusions located in the interior of the crystals and not along visible fractures. Some crystals were polished to expose the inclusions at the surface while others were left unpolished. Inclusions in these latter samples were thus located beneath the crystal surface when analyzed. Five unexposed inclusions were analyzed to determine the H<sub>2</sub>O content. They were then exposed at the surface by polishing and re-analyzed to determine if sample preparation affected the results.

During Raman analysis, the confocal hole was adjusted to include the entire melt inclusion while minimizing the amount of quartz host in the analytical volume. The acquisition time was adjusted to offset the decreased intensity obtained when using smaller confocal hole settings for smaller inclusions. Acquisition times were increased as the inclusion size decreased and resulted in acquisition times ranging from 180 to 360 seconds ( $3 \times 60$  sec to  $3 \times 120$  sec). A beam diameter of 2  $\mu\text{m}$  results in an excitation volume of 6.3 and 12.5  $\mu\text{m}^3$  for focal depths of 2 and 4  $\mu\text{m}$ , respectively, based on different confocal hole settings used in this study.

Table 4.1. Description of Glass Standards used for Raman Calibration

<b>Sample #</b>	<b>Composition</b>	<b>H<sub>2</sub>O wt%</b>	<b>Reference</b>
022881 XII	Na <sub>0.5</sub> K <sub>0.5</sub> AlSi <sub>3</sub> O <sub>8</sub>	7.04	Voigt et al. (1981)
032481 VI	Na <sub>0.25</sub> K <sub>0.75</sub> AlSi <sub>3</sub> O <sub>8</sub>	6.72	Voigt et al. (1981)
032481 VII	Na <sub>0.75</sub> K <sub>0.25</sub> AlSi <sub>3</sub> O <sub>8</sub>	8.08	Voigt et al. (1981)
032481 VIII	Na <sub>0.75</sub> K <sub>0.25</sub> AlSi <sub>3</sub> O <sub>8</sub>	8.06	Voigt et al. (1981)
040281 I	KAlSi <sub>3</sub> O <sub>8</sub>	4.28	Voigt et al. (1981)
040281 II	KAlSi <sub>3</sub> O <sub>8</sub>	4.61	Voigt et al. (1981)
040281 III	KAlSi <sub>3</sub> O <sub>8</sub>	4.93	Voigt et al. (1981)
040281 IV	KAlSi <sub>3</sub> O <sub>8</sub>	5.51	Voigt et al. (1981)
040681 X	NaAlSi <sub>3</sub> O <sub>8</sub>	9.5	Voigt et al. (1981)
041581 II	Na <sub>0.1</sub> K <sub>0.9</sub> AlSi <sub>3</sub> O <sub>8</sub>	6.45	Voigt et al. (1981)
041581 XII	Na <sub>0.1</sub> K <sub>0.9</sub> AlSi <sub>3</sub> O <sub>8</sub>	5.5	Voigt et al. (1981)
Ab 1-0	NaAlSi <sub>3</sub> O <sub>8</sub>	0.98	
Ab 1-5	NaAlSi <sub>3</sub> O <sub>8</sub>	1.53	
Ab 1196 A	NaAlSi <sub>3</sub> O <sub>8</sub>	2.17	
Run 10	See Reference	5.78	Mandeville et al. (2002)
Run 58a	See Reference	5.68	Mandeville et al. (2002)
Run 68	See Reference	2.15	Mandeville et al. (2002)
Run 106	See Reference	1.31	Mandeville et al. (2002)

#### *IV.4.2 Results*

Fourteen unheated melt inclusions from the Bishop Tuff were analyzed using UV excitation and H<sub>2</sub>O contents were calculated using the calibration results presented above. Water contents range from 4.8 – 6.1 wt% (average 5.3 wt%; Fig. 4.5) and are consistent with the range of 4.7 and 6.5 wt% previously reported by other workers (Skirius et al., 1990; Dunbar and Hervig, 1992; Wallace et al., 1999; Anderson et al., 2000; Wallace et al., 2003). No significant differences were observed for inclusions that were analyzed both before and after being exposed at the surface (Table 4.2).

Table 4.2. Results of Raman analysis of melt inclusions in early-erupted Bishop Tuff quartz

<b>Sample Name</b>	<b>3550</b>	<b>850-1250</b>	<b>R</b>	<b>H<sub>2</sub>O wt%</b>
0 A	337573.9	58170.7	5.803	5.0
0 A Polished	890570.0	154420.0	5.767	5.0
0 B	39016.4	6451.9	6.047	5.2
0 B Polished	579864.1	96567.0	6.005	5.2
0 C	76134.1	13303.8	5.723	4.9
0 C Polished	535982.1	93126.4	5.755	4.9
0 D	160291.8	25598.5	6.262	5.4
0 D Polished	961750.6	154387.1	6.229	5.4
0 E	163423.7	24595.0	6.645	5.7
0 E Polished	653694.9	97891.7	6.678	5.7
0 F	87203.7	14946.4	5.834	5.0
0 G	63905.5	11290.9	5.660	4.9
0 H	12456.0	2024.0	6.154	5.3
0 I	20581.8	2723.4	7.557	6.5
0 Average			6.151	5.3
4 A	10239.4	2009.7	5.095	4.4
4 B	58224.0	10655.5	5.464	4.7
4 C	10373.9	1406.5	7.376	6.3
4 D	4572.9	824.3	5.548	4.8
4 E	31936.4	6384.2	5.002	4.3
4 F	9616.5	1561.3	6.159	5.3
4 G	14888.8	1999.9	7.445	6.4
4 H	63867.3	12054.9	5.298	4.6
4 I	87751.2	15372.0	5.709	4.9
4 J	43988.9	8492.5	5.180	4.5
4 K	29820.7	5186.8	5.749	4.9
4 L	35960.0	6653.8	5.404	4.6
4 M	33646.2	6653.8	5.057	4.3
4 N	5811.4	1155.2	5.031	4.3
4 O	91122.6	14280.4	6.381	5.5
4 P	21110.6	3039.0	6.947	6.0
4 Q	11958.9	1776.7	6.731	5.8
4 R	57842.2	8829.3	6.551	5.6
4 S	13592.3	2257.2	6.022	5.2
4 T	11601.9	1854.5	6.256	5.4
4 U	1864.7	349.0	5.343	4.6
4 V	12951.9	2514.7	5.150	4.4
4 Average			5.859	5.0

<b>Sample Name</b>	<b>3550</b>	<b>850-1250</b>	<b>R</b>	<b>H<sub>2</sub>O wt%</b>
12 A	43863.1	7432.6	5.901	5.1
12 B	9772.0	1914.4	5.104	4.4
12 C	174012.7	34677.3	5.018	4.3
12 D	6304.3	927.0	6.801	5.8
12 E	8922.4	1358.5	6.568	5.6
12 F	45032.2	8561.0	5.260	4.5
12 G	22588.3	4325.0	5.223	4.5
12 H	8940.8	1477.9	6.050	5.2
12 I	24582.1	4701.0	5.229	4.5
12 J	8236.0	1297.0	6.350	5.5
12 K	42233.0	6832.0	6.182	5.3
12 L	25212.3	4865.0	5.182	4.5
12 Average			5.739	4.9
24 A	237611.6	48126.5	4.937	4.2
24 B	22023.4	3370.8	6.534	5.6
24 C	37057.6	7600.1	4.876	4.2
24 D	408362.7	74612.3	5.473	4.7
24 E	78983.2	16945.3	4.661	4.0
24 F	24532.5	4953.0	4.953	4.3
24 G	46157.8	10118.0	4.562	3.9
24 H	6728.2	1389.3	4.843	4.2
24 I	10672.7	1902.0	5.611	4.8
24 J	80428.9	17596.7	4.571	3.9
24 K	16431.7	3184.1	5.161	4.4
24 L	127979.6	27474.9	4.658	4.0
24 Average			5.070	4.4
48 A	6084.0	1957.8	3.108	2.7
48 B	2631.7	717.9	3.666	3.2
48 C	4434.2	983.4	4.509	3.9
48 D	6124.4	1894.4	3.233	2.8
48 E	36217.2	11111.4	3.259	2.8
48 F	14861.5	4562.0	3.258	2.8
48 G	49478.3	14472.3	3.419	2.9
48 H	9661.8	1700.9	5.680	4.9
48 I	3882.6	583.7	6.652	5.7
48 J	6517.1	997.3	6.535	5.6
48 K	12760.4	3636.1	3.509	3.0
48 L	23937.5	7537.7	3.176	2.7
48 M	22467.1	4775.3	4.705	4.0
48 Average			4.208	3.6

<b>Sample Name</b>	<b>3550</b>	<b>850-1250</b>	<b>R</b>	<b>H<sub>2</sub>O wt%</b>
168 A	36546.5	20787.1	1.758	1.5
168 B	7413.4	3678.0	2.016	1.7
168 C	58247.0	17997.3	3.236	2.8
168 D	80604.7	19941.2	4.042	3.5
168 E	22385.7	12115.6	1.848	1.6
168 F	19126.3	11005.2	1.738	1.5
168 G	91287.5	42199.1	2.163	1.9
168 H	35470.8	22458.4	1.579	1.4
168 I	84446.3	43043.7	1.962	1.7
168 J	9177.5	3954.0	2.321	2.0
168 K	34648.4	21476.0	1.613	1.4
168 L	102257.1	37266.5	2.744	2.4
168 M	106844.2	37985.7	2.813	2.4
168 N	120460.2	38026.6	3.168	2.7
168 O	35314.7	16734.6	2.110	1.8
168 P	64853.8	26305.7	2.465	2.1
168 Average			2.349	2.0
672 A	67898.3	36798.5	1.845	1.6
672 B	81094.8	28505.4	2.845	2.4
672 C	20433.2	10343.8	1.975	1.7
672 D	73823.3	40029.9	1.844	1.6
672 E	9718.7	13607.7	0.714	0.6
672 F	60957.4	33291.3	1.831	1.6
672 G	29028.8	7554.2	3.843	3.3
672 H	32248.8	8826.5	3.654	3.1
672 Average			2.319	2.0
1296 A	78401.7	51819.6	1.513	1.3
1296 B	50046.9	40717.7	1.229	1.1
1296 C	46741.5	39027.1	1.198	1.0
1296 D	66828.6	37251.1	1.794	1.5
1296 E	76669.1	45049.1	1.702	1.5
1296 F	44399.0	41153.5	1.079	0.9
1296 G	91173.2	34620.3	2.634	2.3
1296 H	25488.1	9376.1	2.718	2.3
1296 I	88910.0	40120.2	2.216	1.9
1296 J	25960.1	23510.6	1.104	0.9
1296 K	40669.5	28456.1	1.429	1.2
1296 L	2999.9	1608.2	1.865	1.6
1296 M	3340.2	3622.0	0.922	0.8
1296 N	5235.1	3622.0	1.445	1.2
1296 O	4760.8	1759.7	2.705	2.3
1296 Average			1.704	1.5

<b>Sample Name</b>	<b>3550</b>	<b>850-1250</b>	<b>R</b>	<b>H<sub>2</sub>O wt%</b>
1512 A	82751.7	47084.8	1.758	1.5
1512 B	92449.4	54674.5	1.691	1.5
1512 C	125377.6	56781.9	2.208	1.9
1512 D	88275.4	51238.8	1.723	1.5
1512 E	66219.5	59381.3	1.115	1.0
1512 F	81017.0	52485.3	1.544	1.3
1512 G	93659.7	55075.3	1.701	1.5
1512 H	68647.9	54556.0	1.258	1.1
1512 I	14000.8	22561.0	0.621	0.5
1512 J	78598.6	58766.8	1.337	1.1
1512 K	54206.9	33533.0	1.617	1.4
1512 L	92358.3	50565.5	1.827	1.6
1512 M	79727.4	51198.4	1.557	1.3
1512 N	30213.7	23218.5	1.301	1.1
1512 O	68454.7	42631.8	1.606	1.4
1512 P	19593.0	23585.7	0.831	0.7
1512 Q	66442.6	49579.3	1.340	1.2
1512 R	67300.5	27443.3	2.452	2.1
1512 S	39650.6	14468.3	2.741	2.4
1512 T	47617.4	15526.7	3.067	2.6
1512 U	76762.0	42574.0	1.803	1.5
<b>1512 Average</b>			<b>1.671</b>	<b>1.4</b>

3550 = Area under the H<sub>2</sub>O peak at approximately 3550 cm<sup>-1</sup>

850-1250 = Area under the T-O-T peak between 850 and 1250 cm<sup>-1</sup>

R = Area under the 3550 cm<sup>-1</sup> peak divided by the area under the 850-1250 cm<sup>-1</sup> peak

Inclusions that were held at temperature for 12 hours or less showed no significant H<sub>2</sub>O loss when compared to unheated inclusions (Fig. 4.5.; Table 4.2). However, some H<sub>2</sub>O loss is evident after 24 hours of heating and melt inclusions lost about 75% of their original H<sub>2</sub>O after 63 days. The range in H<sub>2</sub>O contents at each time interval is similar to the range in H<sub>2</sub>O contents for the early plinian phase of the Bishop Tuff reported by other workers (Fig. 4.5.).

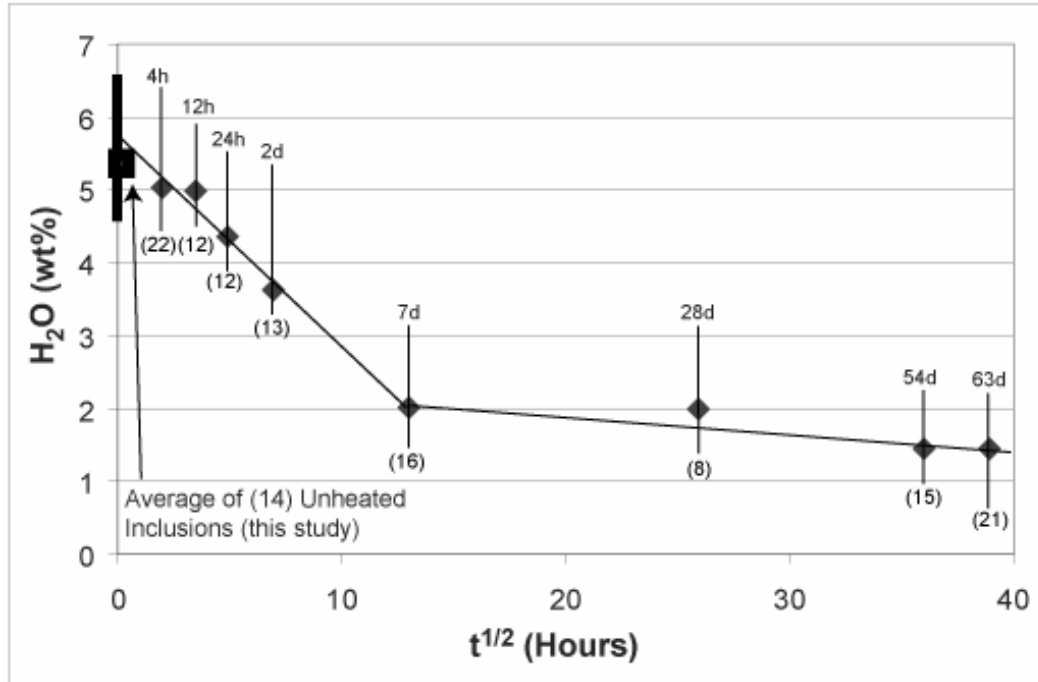


Figure 4.5. Relationship between water content of melt inclusions in quartz from the Bishop Tuff and the amount of time held at 800°C and 1 kbar. Each point represents the average of the measurements in each sample set. The thick line on the y axis is the range of water contents derived from previous studies. The vertical line through each data point represents the minimum and maximum values measured in that sample suite. The value in parentheses directly below the vertical line is the number of inclusions analyzed and the text above the line is the length of time in either hours (h) or days (d). The two lines drawn through all the samples represent the best fit linear equations to describe the different behaviors observed for the water loss.

Water lost to the surrounding crystal should result in the creation of a “vacuum” bubble or expansion of a pre-existing bubble in order to accommodate the volume lost by  $H_2O$  leaving the inclusion (A. Anderson, pers. comm.). The volume change associated with  $H_2O$  loss can be calculated using mass balance constraints the partial molar volumes of  $H_2O$  and the melt. The molecular weight of  $H_2O$  is 18.0 g/mol, the molecular weight of the melt was assumed to be 186.374 g/mol for a typical granitic composition, the melt density was assumed to be 2.23 g/cm<sup>3</sup> and the partial molar volume of  $H_2O$  in the melt was assumed to be 17.0 cm<sup>3</sup>/mol (Student and Bodnar, 1996; Lange, 1994). We assumed 100 g of melt inside the inclusion for simplicity. The volume is defined as:

$$V_{MI} = M_{MI} / \rho_{melt}. \quad (4.1)$$

This results in an inclusion volume of 44.84 cm<sup>3</sup>. A MI with 5 wt % H<sub>2</sub>O contains 5 g H<sub>2</sub>O and 95 g melt. The number of moles of H<sub>2</sub>O is equal to:

$$\text{Moles}_{H_2O} = X \text{ g H}_2\text{O} \times 1 \text{ mol H}_2\text{O} / 18.02 \text{ g H}_2\text{O}. \quad (4.2)$$

$$\text{Moles}_{H_2O} = 5 \text{ g H}_2\text{O} \times 1 \text{ mol H}_2\text{O} / 18.02 \text{ g H}_2\text{O} = 0.2778 \text{ moles H}_2\text{O}$$

The number of moles of melt in the inclusion is:

$$\text{Moles}_{melt} = Y \text{ g melt} \times 1 \text{ mol} / 186.374 \text{ g/mol}. \quad (4.3)$$

$$\text{Moles}_{melt} = 95 \text{ g melt} \times 1 \text{ mol} / 186.374 \text{ g/mol} = 0.5097 \text{ moles melt}$$

The total number of moles in the inclusion is the sum of (4.2) and (4.3), or 0.7875 moles.

The total molar volume of the inclusion is:

$$V_{molar} = V_{Total} / \text{Moles}_{Total} \quad (4.4)$$

and using the values for the total number of moles and the total volume listed above results in a total molar volume of 56.94 cm<sup>3</sup>/mol. This value can then be used to calculate the partial molar volume of melt in the inclusion according to:

$$V_{molar} = (\text{moles}_{melt}) \times (\overline{V}_{melt}) + (\text{moles}_{H_2O}) \times (\overline{V}_{H_2O}). \quad (4.5)$$

$$56.94 \text{ cm}^3/\text{mol} = (0.5097 \text{ moles}) \times (\overline{V}_{melt}) + (0.2778 \text{ moles}) \times (17.0 \text{ cm}^3/\text{mol})$$

results in a partial molar volume of the melt of 102.45 cm<sup>3</sup>/mol.

If we assume the same inclusion (now containing 96 g) has lost 4 g of H<sub>2</sub>O and only has 1 g H<sub>2</sub>O left, substituting 1 g H<sub>2</sub>O into equation (4.2) results in 0.0556 moles H<sub>2</sub>O, and substituting 95 g melt into equation (4.3) results in 0.5097 moles melt for a total number of moles of 0.5653 in the inclusion. Inserting these two values into equation (4.5) and assuming the same partial molar volumes for the melt and for the H<sub>2</sub>O, results

in a total molar volume of  $53.16 \text{ cm}^3/\text{mol}$ . Inserting this value into equation (4.4) along with the total number of moles (0.5653) results in a total volume for the inclusion of  $30.04 \text{ cm}^3$ , which is 67.0% of the original volume ( $44.84 \text{ cm}^3$ ).

A decrease in the  $\text{H}_2\text{O}$  content from 5 wt% to 1 wt% (which approximately mimics the  $\text{H}_2\text{O}$  loss from the Bishop Tuff melt inclusions after 54 days of heating, Fig. 4.5) should result in a volumetric change of approximately 33.0%. For a  $30 \mu\text{m}$  diameter spherical melt inclusion this represents a volume of  $4665 \mu\text{m}^3$ . If the entire volume decrease is accommodated by a spherical bubble, the bubble will have a diameter of  $20.73 \mu\text{m}$  which is approximately 69% of the diameter of the inclusion.

To test this hypothesis, photomicrographs of melt inclusions from three different heating experiments (48 hours, 168 hours, and 1296 hours) were examined using image analysis software to measure the area percentage of the inclusion occupied by the vapor bubble as a proxy for the volume percentage. Each inclusion was photographed at either 50X or 100X magnification and a  $100 \mu\text{m}$  scale bar was used to calibrate the software. The inclusion area was determined by outlining the inclusion using a polygonal selection tool with a measure option. The area of the bubble was estimated by using an ellipse tool combined with the measure option. The proportion of the inclusion occupied by the bubble was then calculated.

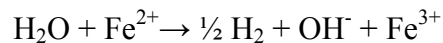
The observed results do not match the 33.0% volume loss predicted by the calculation. The proportion of the MI occupied by the bubble for the 54 day experiment (which best matches the values used in the calculation) show a range in bubble ratios from 0.2% to 9.3%, with an average of 2.8%. The results for shorter experiments (48 hours and 7 days) show a smaller range in bubble ratios with the 48 hour samples showing negligible bubble formation. The results indicate that bubbles are larger for inclusions held at elevated temperature for longer time periods. However, they do not approach the size (bubble proportion) predicted by the calculation above.

One possible explanation for the large range in bubble size is that the calculation does not account for the initial presence of a bubble of some size. The wide range of observed bubble sizes could also indicate that less than 4 g of  $\text{H}_2\text{O}$  was lost. The range of  $\text{H}_2\text{O}$  contents for 54 day experiments ranges from about 0.9 to 2.5 wt%. However, the

difference between the calculated bubble size and the observed sizes remains unexplained.

After a few hundred hours of heating, the rate of H<sub>2</sub>O loss appears to decrease (Fig. 4.5). The decreasing rate of H<sub>2</sub>O loss suggests a change in either the speciation or the mechanism of H<sub>2</sub>O loss from the inclusion with time. For low H<sub>2</sub>O content rhyolitic melts, H<sub>2</sub>O is present mostly as OH, whereas molecular H<sub>2</sub>O becomes more important at higher H<sub>2</sub>O contents (Tomozawa, 1985; Chekhmir et al., 1989; Stolper, 1989; Silver et al., 1990; Zhang et al., 1991). For the observed H<sub>2</sub>O contents in Bishop Tuff melt inclusions, H<sub>2</sub>O should be present mostly as molecular H<sub>2</sub>O. NMR and IR spectroscopy suggest that OH groups in the melt are structurally bonded to Si or Al (i.e. Wu, 1980; Schmidt et al., 2001). These observations suggest that the initial loss of H<sub>2</sub>O from the inclusions involves molecular H<sub>2</sub>O. The most important driving force for H<sub>2</sub>O loss is a H<sub>2</sub>O activity (or fugacity) gradient between the inclusion and surrounding quartz host. Two models that are consistent with these results can explain H<sub>2</sub>O loss from the Bishop Tuff melt inclusions.

One model involves the dissociation of molecular H<sub>2</sub>O according to the reaction



The charge balance would most likely be offset by oxidation of Fe in the melt but could be accomplished by oxidation of other metals in the melt. Hydrogen diffuses rapidly through quartz and into and out of inclusions at temperatures higher than 400-500° C (Mavrogenes and Bodnar, 1994), while OH<sup>-</sup> is expected to diffuse more slowly due to its larger molecular size. Massare et al. (2002) explained the formation of iron oxides in melt inclusions during heating to be the result of an increase in the oxidation state of the melt as a result of this process.

A second interpretation of the observed H<sub>2</sub>O loss is that molecular H<sub>2</sub>O diffuses out of inclusions along either preexisting or strain-induced dislocations in the host quartz. As H<sub>2</sub>O diffuses out of the inclusion along dislocations, hydrolytic weakening and plastic deformation occur which facilitates the formation and growth of additional dislocations (Kronenberg et al., 1986; Gerretsen et al., 1989; Cordier et al., 1994). This behavior has been documented for H<sub>2</sub>O loss from aqueous fluid inclusions during reequilibration (Bakker and Jansen, 1990; Vityk et al., 2000). In quartz molecular H<sub>2</sub>O diffuses more

rapidly than hydroxyl groups (Farver and Yund, 1991), suggesting that the decrease in the rate of H<sub>2</sub>O loss from the melt inclusions after a few hundred hours of heating represents a change from a molecular-H<sub>2</sub>O dominated mechanism to one in which OH is the dominant species. Additionally, charged species typically have slower diffusion rates compared to uncharged species, regardless of size (Fortier and Giletti, 1989; Yund and Snow, 1989; Farver and Yund, 1991).

Another possible explanation is that molecular H<sub>2</sub>O is lost along microcracks that form at the quartz  $\alpha$ - $\beta$  transition at 573° C (at 1 atm pressure, with the temperature of the phase transition increasing  $\approx 25^\circ\text{C}$  per kbar) as has been shown for fluid inclusions (Bodnar et al., 1989). The fracturing that occurs around inclusions when quartz passes through the  $\alpha$ - $\beta$  transition is a result of the large pressure differential between the inclusion and the surrounding medium. Thus, fracturing is reduced if the external pressure is at or above the pressure in the inclusion. By heating the Bishop Tuff melt inclusions at 1 kbar, the pressure differential, and thus the likelihood of fracturing and H<sub>2</sub>O loss, is less than would be expected if the samples were heated at 1 atm. Finally, hydrogen could be lost as HF or other similar species, but this is unlikely for the Bishop Tuff inclusions based on the low concentration of F in the MI (Dunbar and Hervig, 1992; Anderson et al., 2000).

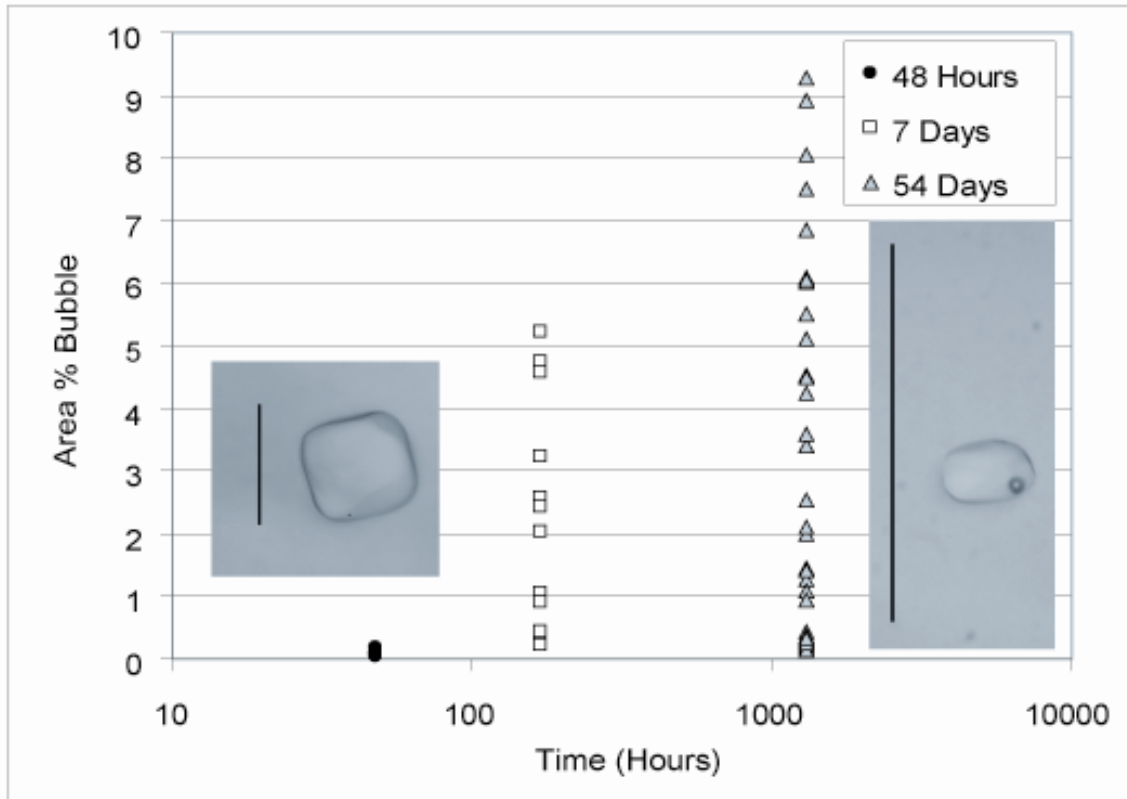


Figure 4.6. Relationship between ratio of the bubble area to the total area of the melt inclusion and amount of time the inclusion was held at 800°C and 1 kbar.

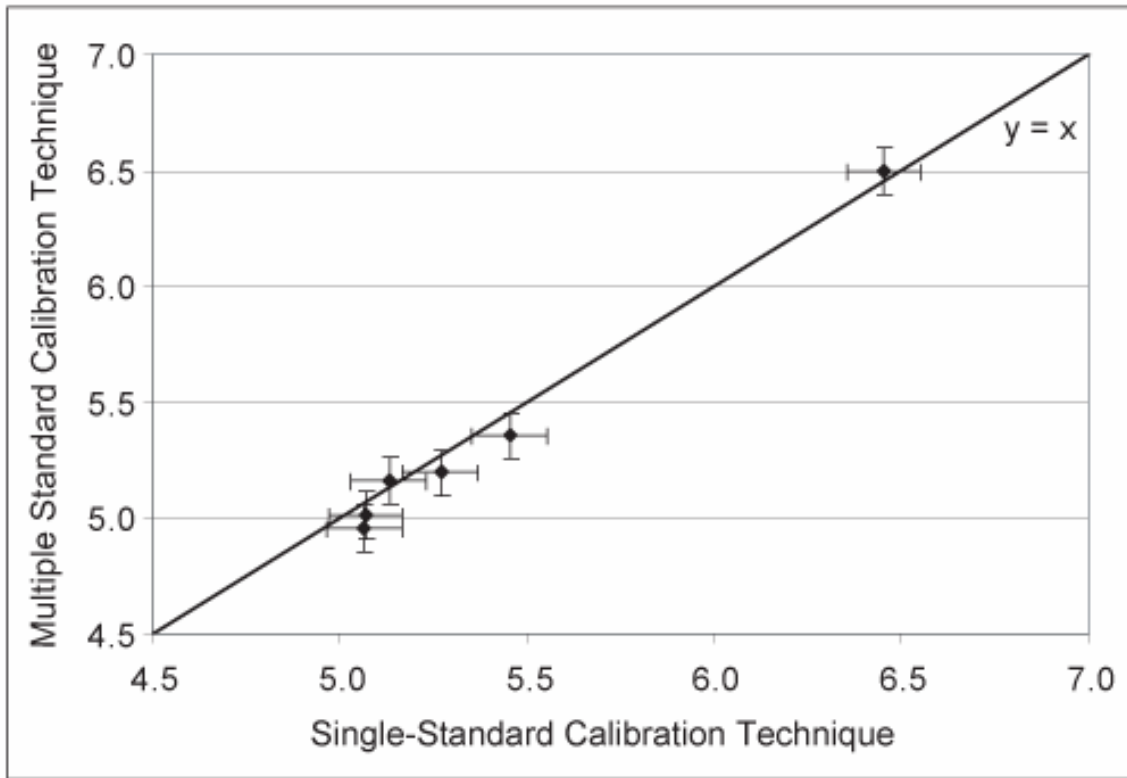


Figure 4.7. Comparison between the single-standard technique used by Thomas et al. (2006) & Di Muro et al. (2006), and the multiple standard calibration technique used in section 3 above. A 1:1 line is plotted for comparison.

## IV.5. Conclusions

Laser Raman spectroscopy provides a simple, nondestructive technique to determine H<sub>2</sub>O contents of silicate glasses, including melt inclusions as small as 5-10 μm. In this study, we have documented the use of ultraviolet (244 nm) excitation to minimize fluorescence. Results indicate that UV Raman excitation produces data of similar quality to that obtained using visible Raman excitation, but results in a different calibration curve. The UV-Raman technique can be used to determine H<sub>2</sub>O contents of fluorescent glasses and melt inclusions that cannot be analyzed using visible wavelength Raman spectroscopy.

While this manuscript was in review, Thomas et al. (2006), and Di Muro et al. (2006) both published results describing a technique for determining H<sub>2</sub>O contents of melt inclusions based on comparison of peak ratios for the unknown and a single standard of known H<sub>2</sub>O content. The H<sub>2</sub>O peak area ratio (3100-3750 cm<sup>-1</sup>) for the standard and unknown equals the ratio of the H<sub>2</sub>O content of the standard and unknown. Several unheated melt inclusions that had been analyzed previously in this study using the technique described in section 3 above were reanalyzed using UV Raman to confirm the applicability of the newer method. The results shown in Figure 7 indicate a good 1:1 correlation between these two techniques suggesting that the single-standard technique can also be applied when using a UV excitation source.

The UV-Raman technique was used to monitor H<sub>2</sub>O loss from melt inclusions in the Bishop Tuff that were held at 800°C and 1 kbar for periods of time ranging from 4 hours to 63 days. Our results suggest that significant H<sub>2</sub>O is not lost during heating experiments of 12 hours or less. However, as much as 75% of the H<sub>2</sub>O in melt inclusions was lost when held at temperature for several hundred hours. The rate of H<sub>2</sub>O loss decreases with time, consistent with a mechanism that involves loss of molecular H<sub>2</sub>O initially, followed by OH<sup>-</sup> as the H<sub>2</sub>O content of the inclusion decreases.

## IV.6. Acknowledgements

The authors would like to thank Charles Farley for technical assistance with the Raman microprobe. Beth Glusica assisted with Raman analyses. Jake Lowenstern provided useful suggestions on melt inclusion techniques, Larry Anovitz clarified our understanding of the behavior of H<sub>2</sub>O in silicate glasses, and Don Rimstidt for refining our interpretation of the diffusion mechanism. Special thanks to Fred Anderson, who introduced us to the Bishop Tuff and helped us to better understand the process of H<sub>2</sub>O loss from melt inclusions. We are indebted to Rainer Thomas and Jean Dubessy for their constructive reviews that significantly improved this manuscript. Partial funding for this project was provided by NSF grants EAR-0337094 and EAR-0322119 to RJB.

Sample preparation, heating experiments, calibration of Laser Raman Spectrometer, collection and processing of Laser Raman spectra using a green laser source have been carried out by Tristan Azbej and Matthew J. Severs. Calibration of Laser Raman Spectrometer, collection and processing of Laser Raman spectra using an ultraviolet excitation source have been carried out by Matthew J. Severs.

## IV.7. References Cited

- Anderson, A.T., Jr., Davis, A.M., Lu, F., 2000. Evolution of Bishop Tuff rhyolitic magma based on melt and magnetite inclusions and zoned phenocrysts. *Journal of Petrology* 41, 449-473.
- Bakker, R.J., Jansen, J.B.H., 1990. Preferential water leakage from fluid inclusions by means of mobile dislocations. *Nature* 345, 58-60.
- Bodnar, R.J., 1995. Fluid inclusion evidence for a magmatic source for metals in porphyry copper deposits. In: Thompson, J. F. H. (Ed.), *Mineralogical Association of Canada Short Course Volume 23, Magmas, Fluids and Ore Deposits*, 139-152.
- Bodnar, R.J., 2003a. Introduction to fluid inclusions. In: Samson, I., Anderson, A., & Marshall, D. (Eds.), *Fluid Inclusions: Analysis and Interpretation*. Mineral. Assoc. Canada, Short Course 32, 1-8.

- Bodnar, R.J., 2003b. Reequilibration of fluid inclusions. In: Samson, I., Anderson, A., & Marshall, D. (Eds.), *Fluid Inclusions: Analysis and Interpretation*. Mineral. Assoc. Canada, Short Course 32, 213-230.
- Bodnar, R.J., Student, J.J., 2006. Melt inclusions in plutonic rocks: Petrography and microthermometry. In: Webster, J.D. (Ed.), *Melt Inclusions in Plutonic Rocks*. Mineral. Assoc. Canada, Short Course 36, 1-26.
- Bodnar, R.J., Binns, P.R., Hall, D.L., 1989. Synthetic fluid inclusions – VI. Quantitative evaluation of the decrepitation behavior of fluid inclusions in quartz at one atmosphere confining pressure. *Journal of Metamorphic Geology* 7, 229-242.
- Burnham, C.W., 1979. Magmas and hydrothermal fluids. In: Barnes, H.L. (Ed.), *Geochemistry of Hydrothermal Ore Deposits* 1st Ed., pp. 71-136. John Wiley & Sons Ltd., New York.
- Burnham, C.W., 1997. Magmas and hydrothermal fluids. In: Barnes, H.L. (Ed.), *Geochemistry of Hydrothermal Ore Deposits* 3rd Ed., pp. 63-123. John Wiley & Sons Ltd., New York.
- Chabiron, A., Pironon, J., Massare, D., 2004. Characterization of water in synthetic rhyolitic glasses and natural melt inclusions by Raman spectroscopy. *Contributions to Mineralogy and Petrology* 146, 485-492.
- Chekhmir, A.S., Epel’baum, M.B., Simakin, A.G., 1989. Transport of water in magmatic melts. *Geochemistry International* 10, 125-127.
- Cordier, P., Doukhan, J-C., Ramboz, C., 1994. Influence of dislocations on water leakage from fluid inclusions in quartz: A quantitative reappraisal. *European Journal of Mineralogy* 6, 745-752.
- Danyushevsky, L.V., Della-Pasqua, F.N., Sokolov, S., 2000. Re-equilibration of melt inclusions trapped by magnesian olivine phenocrysts from subduction-related magmas: petrologic implications. *Contributions to Mineralogy and Petrology* 138, 68-83.
- Di Muro, A., Villemant, B., Montagnac, G., Scaillet, B., Reynard, B., 2006, Quantification of water content and speciation in natural silicic glasses (phonolite, dacite, rhyolite) by confocal microRaman spectroscopy. *Geochimica et Cosmochimica Acta*, in press.

- Dunbar, N.W., Hervig, R.L., 1992. Petrogenesis and volatile stratigraphy of the Bishop Tuff: Evidence from melt inclusion analysis. *Journal of Geophysical Research* 97, 15,129-15,150.
- Farver, J.R., Yund, R.A., 1991. Oxygen diffusion in quartz: Dependence of temperature and water fugacity. *Chemical Geology* 90, 55-70.
- Fortier, S.M., Giletti, B.J., 1989. An empirical model for predicting diffusion coefficients in silicate minerals. *Science* 245, 1481-1484.
- Gerretsen, J., Paterson, M.S., McLaren, A.C., 1989. The uptake and solubility of water in quartz at elevated pressures and temperature. *Physics and Chemistry of Minerals* 16, 334-342.
- Holtz, F., Beny, J-M., Mysen, B.O., Pichavant, M. 1996. High-temperature Raman spectroscopy of silicate and aluminosilicate hydrous glasses: Implications for water speciation. *Chemical Geology* 128, 25-39.
- Keresztury, G., 2002. Raman-spectroscopy: Theory. In: Chalmers, J.M., Griffiths, P.R. (Eds.), *Handbook of Vibrational Spectroscopy* 1, p. 71-87. John Wiley & Sons Ltd., Chichester, England.
- Kronenberg, A.K., Kirby, S.H., Aines, R.D., Rossman, G.R., 1986. Solubility and diffusional uptake of hydrogen in quartz: Implications for hydrolytic weakening. *Journal of Geophysical Research* 91, 12723-12744.
- Lange, R.A., 1994. The effect of H<sub>2</sub>O, CO<sub>2</sub>, and F on the density and viscosity of silicate melts. In: Carroll, M.R., & Holloway, J.R. (Eds.), *Reviews in Mineralogy* 30, pp. 331-369. Mineralogical Society of America, Washington, DC.
- Long, D.A., 2002. *The Raman effect: A unified treatment of the theory of Raman scattering by molecules*. John Wiley & Sons Ltd., Chichester, England.
- Lowenstern, J.B., 1995. Applications of silicate melt inclusions to the study of magmatic volatiles. In: Thompson, J. F. H. (Ed.), *Magmas, Fluids, and Ore Deposits, Short Course 23*, p. 71-101. Mineralogical Association of Canada, Victoria.
- Mandeville C.W., Webster, J.D., Rutherford, M.J., Taylor, B.E., Timbal, A., Faure, K., 2002. Determination of extinction coefficients for infrared absorption bands of H<sub>2</sub>O in andesitic glasses. *American Mineralogist* 87, 813-821.

- Massare, D., Metrich, N., Clocchiatti, R., 2002. High-temperature experiments on silicate melt inclusions in olivine at 1 atm: inferences on temperature of homogenization and H<sub>2</sub>O concentrations. *Chemical Geology* 183, 87-98.
- Massare, D., Metrich, N., Thellier, B., Clocchiatti, R., 1998. Evidence of H<sub>2</sub>O loss in melt inclusions after a series of heating stage experiments. *Terra Abstracts* 10, 39.
- Matson, D.W., Sharma, S.K., Philpotts, J.A., 1983. The structure of high-silica alkali-silicate glasses – A Raman-spectroscopic investigation. *Journal of Non-Crystalline Solids* 58, 323-352.
- Mavrogenes, J.A., Bodnar, R.J., 1994. Hydrogen movement into and out of fluid inclusions in quartz: Experimental evidence and geologic implications. *Geochimica et Cosmochimica Acta* 58, 141-148.
- McMillan, P.F., 1994. Water solubility and speciation models. In: Carroll, M.R., & Holloway, J.R. (Eds.), *Reviews in Mineralogy* 30, pp. 131-156. Mineralogical Society of America, Washington, DC.
- McMillan, P.F., Piriou, B., Navrotsky, A., 1982. A Raman-spectroscopic study of glasses along the joins silica-calcium aluminate, silica-sodium aluminate, and silica-potassium aluminate. *Geochimica et Cosmochimica Acta* 46, 2021-2037.
- McMillan, P.F., Wolf, G.H., 1995. Vibrational spectroscopy of silicate liquids. In: Stebbins, J., McMillan, P.F., & Dingwell, D.B. (Eds.), *Reviews in Mineralogy* 32, p. 247-315. Mineralogical Society of America, Washington, DC.
- McMillan, P.F., Wolf, G.H., Poe, B.T., 1992. Vibrational spectroscopy of silicate liquids and glasses. *Chemical Geology* 96, 351-366.
- Mysen, B.O., 1997. Aluminosilicate melts: Structure, composition and temperature. *Contributions to Mineralogy and Petrology* 127, 104-118.
- Mysen, B.O., 1999. Structure and properties of magmatic liquids: From haplobasalt to haploandesite. *Geochimica et Cosmochimica Acta* 63, 104-118.
- Pasteris, J.D., Wopenka, B., Seitz, J.C., 1988. Practical aspects of quantitative laser Raman microprobe spectroscopy for the study of fluid inclusions. *Geochimica et Cosmochimica Acta* 52, 979-988.
- Qin, Z., Lu, F., Anderson, A.T., Jr., 1992. Diffusive reequilibration of melt and fluid inclusions. *American Mineralogist* 77, 565-576.

- Roedder, E., 1984. Fluid Inclusions. Reviews in Mineralogy 12. Mineralogical Society of America, Washington, D.C.
- Schmidt, B.C., Behrens, H., Riemer, T., Kappes, R., Dupree, R., 2001. Quantitative determination of water speciation in aluminosilicate glasses: A comparative NMR and IR spectroscopic study. *Chemical Geology* 174, 195-208.
- Seifert, F.A., Mysen, B.O., Virgo, D., 1981. Structural similarity of glasses and melts relevant to petrological processes. *Geochimica et Cosmochimica Acta* 45, 1879-1884.
- Sharma, S.K., Cooney, T.F., Wang, Z.F., vanderLaan, S., 1997. Raman band assignments of silicate and germanate glasses using high-pressure and high-temperature spectral data. *Journal of Raman Spectroscopy* 28, 697-709.
- Silver, L.A., Ihinger, P.D., Stolper, E.M., 1990. The influence of bulk composition on the speciation of water in silicate glasses. *Contributions to Mineralogy and Petrology* 104, 142-162.
- Skirius, C.M., Peterson, J.W., Anderson, A.T., Jr., 1990. Homogenizing rhyolitic glass inclusions from the Bishop Tuff. *American Mineralogist* 75, 1381-1398.
- Smith, E., and Dent, G., 2005. *Modern Raman spectroscopy: A practical approach*. John Wiley & Sons, Ltd. Chichester, England.
- Sparks, R.S.J., Barclay, J., Jaupart, C., Mader, H.M., Phillips, J.C., 1994. Physical aspects of magmatic degassing I. Experimental and theoretical constraints on vesiculation. In: Carroll, M.R., & Holloway, J.R. (Eds.), *Reviews in Mineralogy* 30, pp. 413-445. Mineralogical Society of America, Washington, DC.
- Stolper, E.M., 1989. Temperature dependence of the speciation of water in rhyolitic melts and glasses. *American Mineralogist* 74, 1247-1257.
- Student, J.J., Bodnar, R.J., 1996. Melt inclusion microthermometry: Petrologic constraints from the H<sub>2</sub>O-saturated haplogranite system. *Petrology* 4, 291-306.
- Student, J.J., Bodnar, R.J., 1999. Synthetic fluid inclusions XIV: Coexisting silicate melt and fluid inclusions in the haplogranite-H<sub>2</sub>O-NaCl-KCl system. *Journal of Petrology* 40, 1509-1525.

- Student, J.J., Bodnar, R.J., 2004. Silicate melt inclusions in porphyry copper deposits: Identification and homogenization behavior. *Canadian Mineralogist*, 42, 1563-1600.
- Thomas, J.B., Bodnar, R.J., Farley, C., 2002. A further test of the Raman technique for determining water contents of silicate glasses. In: Kontak, D.J., & Anderson, A.J. (Eds.), 8th Biennial Pan-American Conference on the Research on Fluid Inclusions, Program with Abstracts, Nova Scotia Department of Natural Resources, p. 105.
- Thomas, R., 2000. Determination of water contents of granite melt inclusions by confocal laser Raman microprobe spectroscopy. *American Mineralogist* 85, 868-872.
- Thomas, R., 2002a. Determination of water contents in melt inclusions by laser Raman spectroscopy. In: De Vivo, B., & Bodnar, R.J. (Eds.), Proceedings from the Workshop – Short Course on volcanic systems, geochemical and geophysical monitoring – Melt inclusions: methods, applications and problems. Sept. 26-30 in Napoli, Italy, pp. 211-216.
- Thomas, R., 2002b. Determination of the H<sub>3</sub>BO<sub>3</sub> concentration in fluid and melt inclusions in granite pegmatites by laser Raman microprobe spectroscopy. *American Mineralogist* 87, 56-68.
- Thomas, R., Kamenetsky, V.S., Davidson, P., 2006. Laser Raman spectroscopic measurements of water in unexposed glass inclusions. *American Mineralogist* 91, 467-470.
- Tomozawa, M., 1985. Concentration dependence of the diffusion coefficient of water in SiO<sub>2</sub> glass. *Journal of American Ceramics Society* 68, C251-C252.
- Vityk M.O., Bodnar R.J., Doukhan, J-C., 2000. Synthetic fluid inclusions: XV. TEM investigation of plastic flow associated with re-equilibration of synthetic fluid inclusions in natural quartz. *Contributions to Mineralogy and Petrology* 139, 285-297.
- Voigt D.E., Bodnar R.J., Blencoe J.G., 1981. Water solubility in melts of alkali feldspar composition at 5 kbar and 950°C. *EOS*, 62, 428.
- Wallace, P.J., Anderson, A.T., Jr., Davis, A.M., 1999. Gradients in H<sub>2</sub>O, CO<sub>2</sub>, and exsolved gas in a large-volume silicic magma system: Interpreting the record

- preserved in melt inclusions from the Bishop Tuff. *Journal of Geophysical Reviews* 104, 20097-20122.
- Wallace, P.J., Dufek, J., Anderson, A.T., Jr., Zhang, Y., 2003. Cooling rates of Plinian fall and pyroclastic-flow deposits in the Bishop Tuff: Inferences from water speciation in quartz-hosted glass inclusions. *Bulletin of Volcanology* 65, 105-123.
- Wang, Z.F., Cooney, T.F., Sharma, S.K., 1993. High-temperature structural investigation of  $(\text{Na}_2\text{O})_{0.5}(\text{Fe}_2\text{O}_3)_{0.3}\text{SiO}_2$  and  $\text{Na}_2\text{O}(\text{FeO})_3\text{SiO}_2$  melts and glasses. *Contributions to Mineralogy and Petrology* 115, 112-122.
- Wu, C.K., 1980. Nature of incorporated water in hydrated silicate glasses. *Journal of the American Ceramic Society* 63, 453-457.
- Yund, R.A., Snow, E., 1989. Effects of hydrogen fugacity and confining pressure on the interdiffusion rate of NaSi-CaAl in plagioclase. *Journal of Geophysical Research* 94, 10662-10668.
- Zajacz, Z., Halter, W., Malfait, W.J., Bachmann, O., Bodnar, R.J., Hirschmann, M.M., Mandeville, C.W., Morizet, Y., Müntener, O., Ulmer, P., Webster, J.D., 2005. A composition-independent quantitative determination of the water content in silicate glasses and silicate melt inclusions by confocal Raman-spectroscopy. *Contributions to Mineralogy and Petrology* 150, 631-642.
- Zhang, Y., Stolper, E.M., Wasserburg, G.J., 1991. Diffusion of water in rhyolitic glasses. *Geochimica et Cosmochimica Acta* 55, 441-456.

## **CHAPTER V. Genesis of carbonate aggregates in lamprophyres from the northeastern Transdanubian Central Range, Hungary: Magmatic or hydrothermal origin?**

### **V.1. Introduction**

An igneous rock is said to have an ocellar texture if the “phenocrysts” (ocelli) consist of aggregates of smaller crystals arranged radially or tangentially around larger, generally euhedral crystals to produce a rounded eyelike appearance (e.g. Phillpotts, 1990). Ocelli of globular, carbonate or felsic silicate aggregates are common features of lamprophyres and some alkali basalts (e.g. Phillpotts, 1990; Rock, 1991). For decades ocelli in igneous rocks were interpreted to be the products of silicate–carbonate or silicate–silicate liquid immiscibility or, rarely, as amygdales or vesicles filled by late stage minerals (e.g. Phillpotts and Hodgson, 1968; Ferguson and Currie, 1971; Hamilton et al., 1979; Cooper, 1979; Foley, 1984; Nédli and Tóth, 2003; Vichi et al, 2005). Ocelli are not the only occurrence of carbonate minerals in lamprophyres: carbonates are also found as pseudomorphs after olivine, melilite or other minerals, as intergrowths with talc, garnet, etc., and as late veins (Rock, 1991). Rock (1991) classifies primary and secondary carbonates based on stable isotopic composition of lamprophyres from locations around the world.

Carbonate and silicate ocelli have been described in Late Cretaceous lamprophyre dikes in the Transdanubian Central Range (TCR) in Northwest Hungary (e.g. Horváth et al., 1983; Szabó et al., 1993). The ocelli have been interpreted to be the result of liquid immiscibility in volatile-rich mafic melts (Kubovics et al., 1990). Based on the stable isotopic composition, Demény et al. (1994) showed that the ocelli from TCR lamprophyre dikes represent a transition between primary igneous and sedimentary carbonate. They interpreted the isotopic composition of the aggregates to be the result of hydrothermal fluids, suggesting a genetic model inconsistent with melt immiscibility.

Later detailed petrographic, geochemical and fluid inclusion studies of carbonate aggregates (including ocelli) from the TCR lamprophyres (Azbej, 2002; Azbej et al., 2003) called into question an origin by melt immiscibility or by simple mixing of different fluids. Because the term “ocelli” has genetic implications, we will use the more general term ‘carbonate aggregates’ to describe these features.

The goal of this study is to constrain the genesis of the various types of carbonate aggregates observed in the TCR lamprophyres. Petrographic, cathodoluminescence and electron microprobe analyses of the carbonate aggregates and fluid inclusion microthermometry provide information related to the origin of carbonate aggregates, as well as the late-stage evolution of the TCR lamprophyres.

## **V.2. Geological Background and Lamprophyre Petrology**

During the 1980s, unusual alkaline mafic lamprophyre dikes were recognized in quarries in the NE Transdanubian Central Range, Hungary (Horváth and Ódor, 1984; Kubovics et al., 1989), and in several boreholes (Horváth et al., 1983; Szabó, 1985; Kubovics and Szabó, 1988; Kubovics et al., 1989) (Fig. 5.1). These rocks are Late Cretaceous in age (Horváth et al., 1983; Embey-Isztin et al., 1989, Dunkl, 1989) and occur as dikes or dike swarms and show consistent petrographic and geochemical features including panidiomorphic granular texture, high color index, ocelli content, high volatile and incompatible element abundances and similar ages (Szabó et al. 1993). Clinopyroxene and olivine occur as phenocrysts in the lamprophyres, and many of the olivine grains are altered. The groundmass is characterized by a framework of clinopyroxene and mica microphenocrysts among carbonate, feldspar, apatite and glass. Multiple generations of carbonate-filled veins are also present. Based on modal composition, most of the dike-rocks are classified as monchiquite, but camptonite and alnoite also occur (Embey-Isztin et al., 1989; Kubovics and Szabó, 1988; Kubovics et al., 1989; Szabó et al., 1993). Some dikes contain many upper mantle to crustal xenoliths and xenocrysts (Szabó, 1985; Kubovics et al., 1985; 1989). The dikes are emplaced into Carboniferous granites, Upper Permian sandstones, Triassic carbonates and andesites.

Some carbonatite-like dikes classified as beforite are found in the St-1 borehole (Horváth et al., 1983). The St-1 samples are composed of dolomite (occurring as carbonate aggregates), phlogopite and plagioclase as dominant phases (Horváth et al., 1983). Another carbonatite-like dike containing mostly calcite and phlogopite has been described in the Ad-2 borehole (Szabó et al., 1993).

Geochemical characteristics suggest that the lamprophyric melt was intruded into an intra-plate extensional tectonic zone (Kázmér and Szabó, 1989). Accordingly, lamprophyres are typical of Alpine nappe units located at the outer edge of the accretionary wedge. During the Cretaceous these Alpine nappe units were part of a continental basement far away from the inferred Penninic subduction zone (Kázmér and Szabó, 1989; Kubovics et al., 1989). The most likely origin of the parental lamprophyric melt is through a small degree of partial melting of metasomatized lithospheric mantle (Szabó, 1985; Szabó et al., 1993).

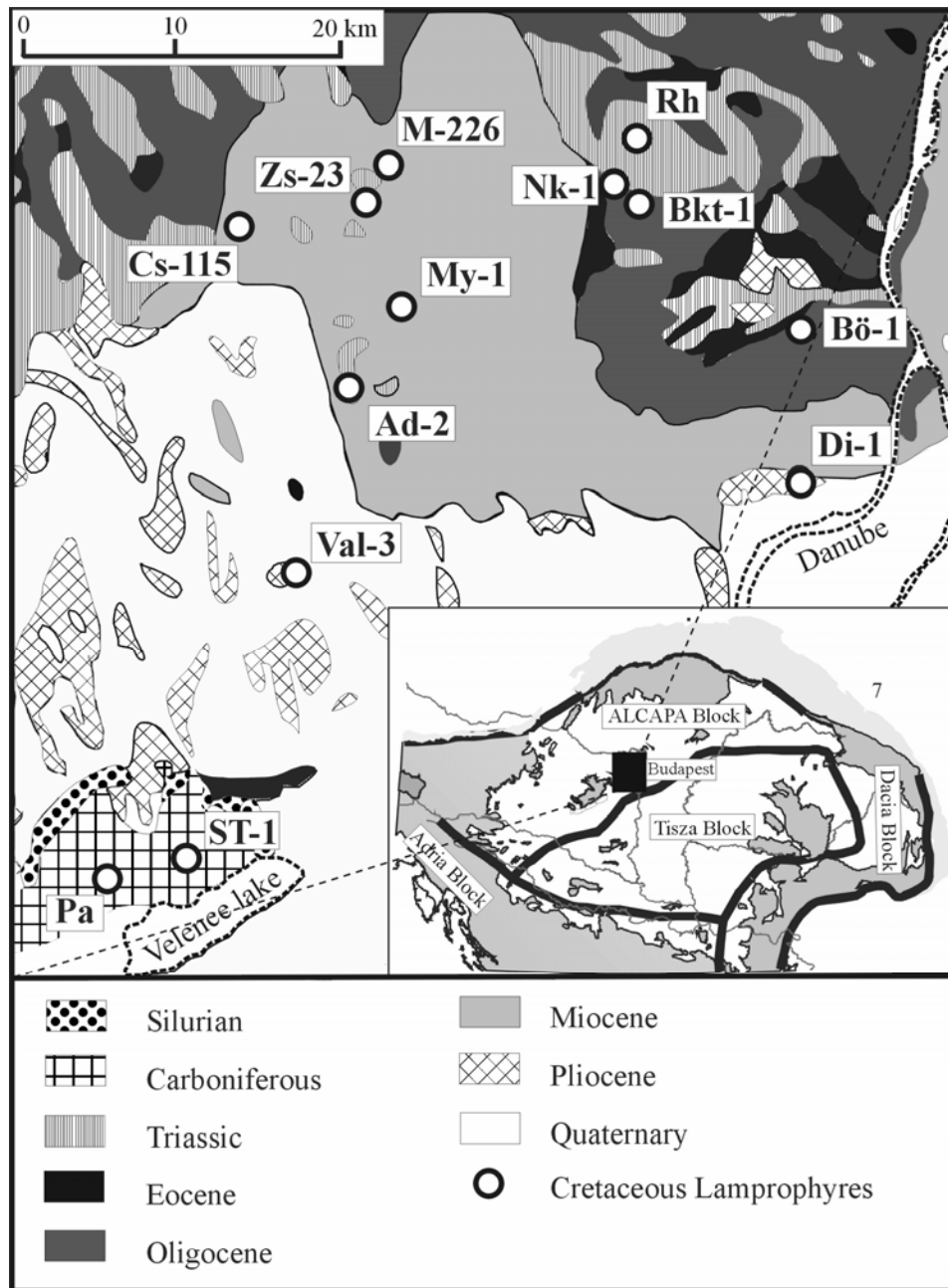


Figure. 5.1. Geological map of the northeastern Transdanubian Central Range (TCR). Black circles show locations of lamprophyres in outcrop and drill holes (from Szabó et al., 1993). Fluid inclusion and chemical data on host phases were obtained from outcrop samples Pá and Rh, and drill core samples Ad-2, Bkt-1, Bö-1, My-1, St-1, Vál-3. inset map shows the Carpathian-Pannonian Region and the study area (black box).

### V.3. Samples Studied and Analytical Methods

Samples were collected from 11 dikes exposed in 2 surface outcrops (4 representative samples: Pá/1, Pá/2, Rh/121, Rh/1012) and 6 boreholes (nine representative samples: Ad-2/II, Ad-2/III, Ad-2/VIII, Ad-2/X, Bkt-1/6, Bö-1/16, My-1/1, St-1/1 Vál-3/2) (Fig. 5.1.). In addition, data from 6 samples collected by Demény et al. (1994) (Ad-2, Bkt-1, Bö-1, Pá, Rh, St-1) have been incorporated into this present study.

Electron microprobe analyses were carried out on a JEOL Superprobe JXA-8600 WDS at the Department of Earth Sciences, University of Florence and on a Cameca SX-50 at the Department of Geosciences at Virginia Tech. The accelerating voltage was 15 kV, with a 10 nA sample current. Mineral analyses were performed using a beam diameter of 10 µm. Counting times were 20 seconds for all elements. Natural mineral standards were employed, and the correction method of Bence and Albee (1968) was applied at the University of Florence, and the ZAF technique was used at Virginia Tech. Backscattered electron images were collected using a JEOL Superprobe 733, equipped with an INCA Energy 200 EDS, at the Institute for Geochemical Research of the Hungarian Academy of Sciences using an accelerating voltage of 20 kV with a 3 nA sample current.

Microthermometric analyses were carried out on a Linkam THMS 600 stage at Virginia Tech. Cathodoluminescence studies were carried on a Technosyn 8200 MK II cold cathodoluminescence microscope at Virginia Tech using a sample current of 600 nA and an accelerating voltage of 10 kV.

#### **V.4. Petrography**

Szabó et al. (1993) reported ocelli from the TCR lamprophyres that contained calcite and dolomite, radial and acicular micas, sanidine, analcime, and oxide minerals, but these authors did not subdivide the ocelli into different types based on textures. In the present study, three textural groups of carbonate aggregates were distinguished. The volume of carbonate aggregates in the lamprophyres varies from about 1 to 45 %.

The temporal classification of inclusions in the TCR lamprophyres was determined based on petrographic characteristics of the inclusions (Goldstein and Reynolds, 1994; Bodnar, 2003a). Inclusions that occur along fractures cross-cutting mineral grains were classified as secondary. Inclusions that appeared to be isolated and not along obvious fractures were interpreted to be primary. While some carbonates in Type-III aggregates are chemically zoned (c.f., Fig. 5.2E, F), growth zones decorated by primary inclusions were not observed.

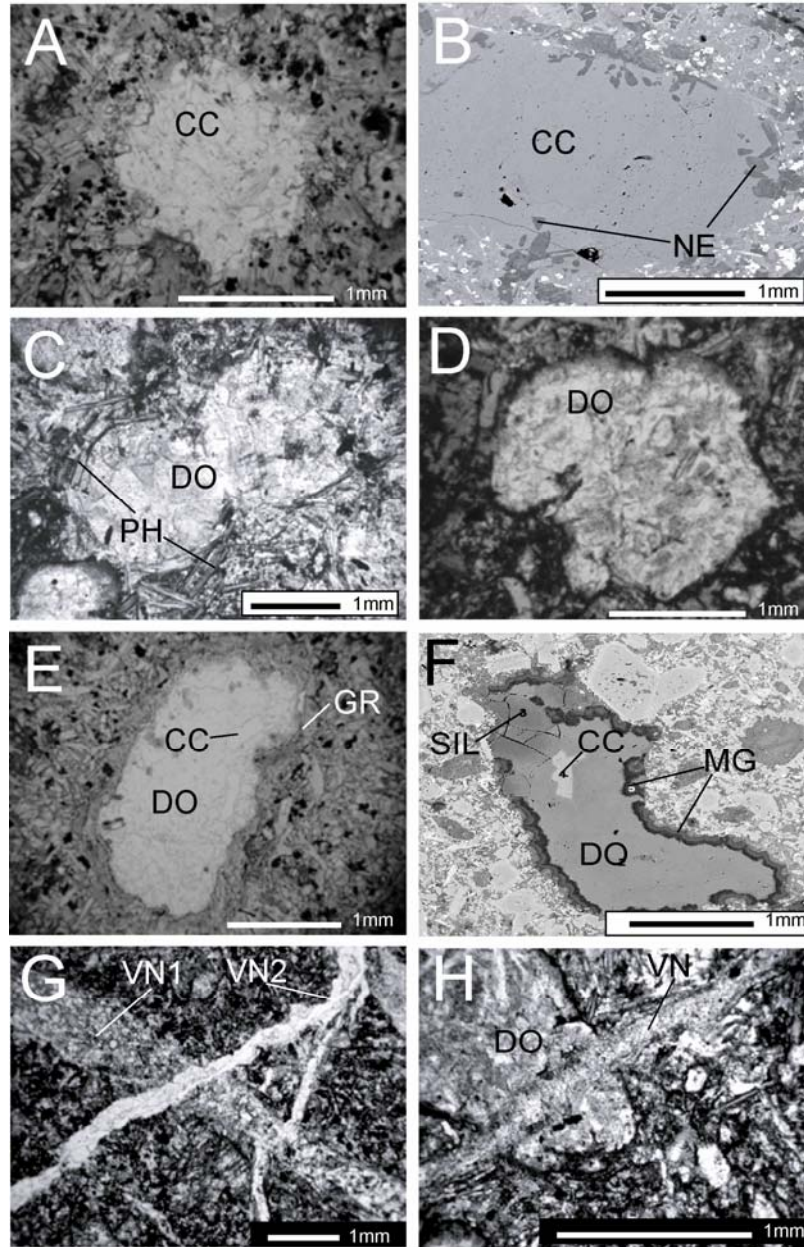


Figure. 5.2. Photomicrographs (A, C, D, E, H) and BSE images (B, F) of carbonate aggregates in the TCR lamprophyres. (A) Type-I aggregate containing calcite (CC) in sample St-1/1 (plane-polarized light). (B) Type-I silicate-bearing aggregate containing calcite (CC), dolomite (DO) and nepheline (NE) in sample My-1/1. (C) Type-I aggregate containing dolomite (DO) surrounded by tangentially aligned phlogopites (PH) in sample St-1/1 (plane-polarized light). (D) Type-II aggregate containing dolomite (DO) in sample St-1/1 (plane-polarized light). (E) Type-III aggregate containing calcite (CC) and dolomite (DO) with glassy rim (GR) in sample Bö-1/16 (plane-polarized light). (F) Mineralogically zoned Type-III aggregate containing calcite (CC), dolomite (DO), magnesite (MG) and Al-silicate (SIL) in sample Rh/1012. (G) Two generations of cross-cutting carbonate veins (VN1, VN2) in sample Ad2-II. (H) Carbonate vein (VN) cross cutting a Type-II dolomite-aggregate (DO) in sample St-1.

Type-I aggregates have petrographic features characteristic of typical ocelli (Fig. 5.2A) and show a globular shape and are approximately 0.2 to 4.0 mm in diameter. In addition to carbonate minerals, silicates (nepheline, analcime, sanidine) and rarely chalcedony are present either as anhedral phases occurring in the interior, or as elongated subhedral phases intersecting the rim of the aggregates (Fig. 5.2B). In some samples phlogopite flakes occur tangentially at the rim of the carbonate aggregates (Fig. 5.2C). The carbonate minerals contain primary fluid inclusions.

Type-II aggregates are found mostly in samples from the St-1 and rarely Ad-2 dikes. The size varies from 0.2 to 3.5 mm in diameter. Their shapes and sizes are similar to those of olivine phenocrysts in the TCR lamprophyres (Fig. 5.2D). Type-II aggregates contain minor chalcedony and primary fluid inclusions. Some thin sections reveal multiple generations of carbonate veins intersecting each other and Type-I and Type-II carbonate aggregates, forming a network (Fig. 5.2G-H).

Type-III aggregates are irregular to polygonal in shape (Fig. 5.2E-F), and vary between 0.1 and 3.0 mm in diameter. In addition to the dominant carbonate phases, clay minerals sometimes occur near the rim (Fig. 5.2F). Cathodoluminescence and SEM images reveal chemical zonation in these aggregates (Fig. 5.2F) in contrast to the relatively homogenous patterns observed in Type-I and Type-II aggregates (Azbej, 2002). Type-III carbonate aggregates contain secondary fluid inclusions.

## **V.5. Chemical Composition of Carbonate Aggregates**

Several carbonate aggregates in each of seventeen samples from eight sample localities (Fig. 5.1, Fig. 5.3a-b; Table 5.1.a-b) have been analyzed. Type-I aggregates consist of calcite, dolomite and minor magnesite (Table 5.1a) and show no compositional or petrographic zoning or evidence of exsolution. Type-II aggregates are composed of ferroan dolomite with FeO of 0.5 to 9.1 wt% and SrO up to 1.7 wt% (Table 5.1b). A diagnostic characteristic of Type-III aggregates is their zoned texture (Fig. 5.2E-F). Based on electron microprobe traverses, a trend from calcite → dolomite → magnesite or

from dolomite → magnesite is observed from the core to the rim in several Type-III aggregates. The thickness of individual zones is on the order of 100  $\mu\text{m}$ . Sometimes ankerite is also observed at the rims. Similar compositional zonation has been reported from the Rh sampling locality by Demény et al. (1994) where a carbonate aggregate with calcite core and dolomite rim was found. Demény et al. (1994) also mention zoned aggregates containing dolomite and magnesite from lamprophyres in the Ad-2 borehole.

All aggregates have relatively high trace and minor element concentration compared to the composition of the Triassic carbonate wall-rocks presented by Balog et al. (1999). Carbonate veins have been analyzed and compared to the composition of carbonates in coexisting aggregates (Table 5.1c). In each of the samples the composition of veins showed similar variation as of the aggregate carbonates. The composition of vein filling carbonates varies from predominantly calcitic (e.g. Ad-2) to ankeritic (Bo-1/16, St-1) (Table 5.1c).

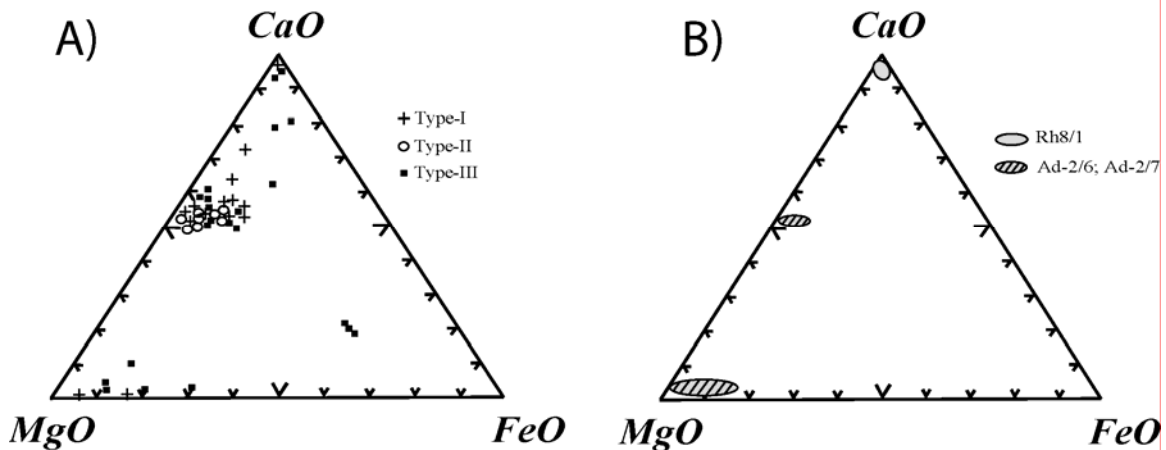


Figure 5.3. Ternary CaO–MgO–FeO diagrams showing compositions of carbonate phases in aggregates from the TCR lamprophyres. (A) Type- I, Type-II and Type–III aggregates in samples from outcrops of Pa, Rh and drilling cores of Ad-2, Bkt-1, Bö-1, My-1, St-1, Vál-3. (B) Composition of carbonates in samples of Ad-2/6, Ad-2/7 and Rh/8 after Demény et al. (1994).

Table 5.1a. Average composition of carbonate minerals in Type-I aggregates from the TCR lamprophyres.

Aggregate type	Type-I																	
	Ad-2/III/3		Bkt1/6		My-1/1		My-1/4		Pa1/1		Pa1/2		St-1/1		St-1/2		Val3/2	
Sample	Dolomite	Magnesite	Calcite	Calcite	Calcite	Dolomite	Mg- Calcite	Calcite	Calcite	Calcite	Calcite	Fe- Dolomite	Dolomite	Dolomite	Dolomite	Dolomite	Dolomite	Dolomite
CaO	29.4	0.11	54.8	55.4	34.4	34.4	40.0	55.0	54.2	55.0	55.0	31.9	28.7	29.6	28.8	28.8	28.8	28.8
MgO	21.2	46.0	0.12	0.05	13.5	13.5	9.99	0.56	0.14	0.21	0.21	15.7	18.8	18.9	20.3	20.3	20.3	20.3
FeO	0.49	3.13	0.15	0.12	3.92	3.92	3.34	b.d.	0.10	0.19	0.19	6.01	4.04	4.06	1.14	1.14	1.14	1.14
MnO	0.13	0.16	b.d.	0.02	0.15	0.15	0.35	b.d.	0.16	0.11	0.11	0.61	0.31	0.19	0.61	0.61	0.61	0.61
SiO	0.11*	b.d.	0.36	0.35	0.47	0.47	0.73	0.45	0.24	0.75	0.20	0.20	1.01	0.24	2.05	2.05	2.05	2.05
BaO	0.10*	0.12*	0.09*	0.10	b.d.	b.d.	b.d.	b.d.	0.13*	0.09*	0.10	0.10	0.09*	b.d.	0.10*	0.10*	0.10*	0.10*
Total	51.2	49.4	55.4	56.0	52.5	52.5	54.4	56.0	54.8	56.2	54.5	54.5	52.8	53.0	52.9	52.9	52.9	52.9
Calc. CO <sub>2</sub>	46.6	49.6	43.3	43.7	44.5	44.5	44.9	44.0	42.9	43.9	46.3	46.3	46.1	46.6	46.7	46.7	46.7	46.7
Calc. Total	98.0	99.0	98.7	99.7	97.0	97.0	99.3	100.0	97.8	100.1	100.8	100.8	98.9	99.5	99.6	99.6	99.6	99.6
CaCO <sub>3</sub> mol%	54.1	0.31	99.0	99.0	63.7	63.7	72.1	98.1	98.8	97.9	97.9	56.7	52.1	53.4	52.0	52.0	52.0	52.0
MgCO <sub>3</sub> mol%	44.7	89.3	0.13	0.12	28.7	28.7	20.7	1.13	0.29	0.43	32.1	32.1	39.2	39.2	42.0	42.0	42.0	42.0
FeCO <sub>3</sub> mol%	0.83	10.1	0.07	0.21	6.65	6.65	5.52	0.03	0.17	0.31	9.81	9.81	6.69	6.73	1.89	1.89	1.89	1.89
MnCO <sub>3</sub> mol%	0.21	0.25	-	0.03	0.26	0.26	0.58	-	0.26	0.19	1.00	1.00	0.52	0.32	1.02	1.02	1.02	1.02
# of measurements	7	2	3	4	1	1	1	2	5	3	3	4	7	3	3	3	3	3

\* Highest concentration measured (not average) for a given trace element in the sample

b.d. Below detection limit

Calc. CO<sub>2</sub> Calculated CO<sub>2</sub> wt%

Calc. Total Total wt% oxides (including CO<sub>2</sub>)

Table 5.1b. Average composition of carbonate minerals in Type-II and -III aggregates from the TCR lamprophyres.

\* Highest concentration measured (not average) for a given trace element in the sample

Aggregate Type	Type-II			Type-III								
	<u>Ad-2/X</u>	<u>St-1/3</u>	<u>St-1/4</u>	<u>Ad-2/IIb</u>	<u>BoI-16/1</u>		<u>BoI-16/2</u>		<u>BoI-16/3</u>	<u>Rh1012/1</u>	<u>Rh1012/3</u>	
Carbonate Phase	Dolomite	Dolomite	Fe-Dolomite	Dolomite	Calcite	Dolomite	Mg-Calcite	Fe-Dolomite	Ankerite	Calcite	Fe-Dolomite	Magnesite
Aggregate Zone	Not zoned	Not zoned	Not zoned	core	core	rim	core	rim	rim	core	rim	rim
CaO	28.8	29.4	29.6	30.7	54.7	11.2	43.9	28.9	1.34	53.2	31.8	1.22
MgO	18.9	17.2	17.4	18.6	0.19	12.0	4.19	16.5	32.8	1.15	18.0	40.7
FeO	5.04	5.78	6.34	3.99	0.11	33.9	6.65	6.69	18.0	0.98	2.54	7.10
MnO	0.17	0.16	0.20	0.09	0.09*	0.63	0.38	0.16	b.d.	0.53	0.47	0.18
SrO	0.29	0.08*	0.10*	0.15	0.95	0.14	0.35	0.10	b.d.	b.d.	0.12*	0.09*
BaO	b.d.	0.09*	b.d.	0.08*	b.d.	b.d.	0.10	b.d.	b.d.	b.d.	0.09*	b.d.
Total	53.3	52.6	53.6	53.5	55.9	57.9	55.6	52.3	52.1	55.8	52.7	49.2
Calc. CO <sub>2</sub>	46.6	45.6	46.3	47.0	43.6	43.1	43.4	45.0	47.9	43.9	46.4	49.9
Calc. Total	99.9	98.3	99.9	100.5	99.6	101.0	99.0	97.3	100.0	99.8	99.3	99.2
CaCO <sub>3</sub> mol%	51.7	53.7	53.3	55.0	98.0	19.8	81.0	53.4	2.62	95.1	57.5	2.24
MgCO <sub>3</sub> mol%	39.0	36.2	35.9	38.1	0.40	24.3	6.90	34.8	68.8	2.36	37.3	85.5
FeCO <sub>3</sub> mol%	8.66	9.67	10.4	6.51	0.18	54.7	11.5	11.4	28.6	1.61	4.21	11.9
MnCO <sub>3</sub> mol%	0.27	0.27	0.33	0.14	0.14	0.97	0.63	0.25	-	0.87	0.78	0.29
# of measurements	2	9	5	4	4	3	2	6	1	3	3	4

*b.d.* Below detection limit

*Calc. CO<sub>2</sub>* Calculated CO<sub>2</sub> wt%

*Calc. Total* Total wt% oxides (including CO<sub>2</sub>)

Table 5.1c. Average composition of carbonate minerals in veins from the TCR lamprophyres.

Sample	Ad-2/II	Bo-1-16	St-1/5
Carbonate Phase	Calcite	Ankerite	Fe-Dolomite
CaO	54.2	3.07	28.5
MgO	0.71	32.3	9.83
FeO	1.51	16.4	16.7
MnO	0.18	0.24	0.11
SrO	0.12*	0.13*	0.12
BaO	0.10*	0.10*	b.d.
Total	56.5	52.0	55.2
Calc. CO <sub>2</sub>	42.8	47.7	43.3
Calc. Total	99.3	99.8	98.5
CaCO <sub>3</sub> mol%	95.9	5.04	51.5
MgCO <sub>3</sub> mol%	1.74	73.6	24.7
FeCO <sub>3</sub> mol%	2.09	21.0	23.6
MnCO <sub>3</sub> mol%	0.25	0.31	0.15
# of measurements	3	7	2

\* Highest concentration measured (not average) for a given trace element in the sample

*b.d.* Below detection limit

*Calc. CO<sub>2</sub>* Calculated CO<sub>2</sub> wt%

*Calc. Total* Total wt% oxides (including CO<sub>2</sub>)

## V.6. Microthermometric Analyses

The formation temperature of carbonate aggregates in the TCR lamprophyres was estimated based on microthermometric analyses of fluid inclusions and chemical compositions of coexisting silicate phases in predominantly carbonate aggregates. According to Boettcher et al. (1980), the water-saturated solidus of magmatic carbonate is above 565°C at pressures less than 5 kbars. Thus, carbonates of hydrothermal origin would be expected to precipitate below 565°C.

Primary fluid inclusions in Types-I and I aggregates and secondary inclusions in Type-III carbonates were analyzed. The carbonate veins did not contain fluid inclusions suitable for microthermometric analysis. Fluid inclusions in Types-I and -II aggregates are scattered randomly in the host mineral, and show no alignment along fracture planes

or growth zones. These inclusions are interpreted to be of primary origin based on mode of occurrence. The inclusions vary from  $<2\ \mu\text{m}$  to about  $14\ \mu\text{m}$ , contain vapor and liquid at room temperature and have irregular to regular negative-crystal shape.

Type-III aggregates contain secondary fluid inclusions along roughly planar, sometimes branching, healed fractures that do not extend to the rim of the aggregates. The inclusions are  $<4\ \mu\text{m}$ , contain liquid and vapor at room temperature, and have an irregular shape. The Type-III aggregates also contain a few randomly distributed inclusions which would be classified as primary based on their occurrence. However, the homogenization temperature and salinity of these inclusions is similar to that of the obviously secondary inclusions. We interpret these randomly distributed inclusions to be either secondary inclusions or primary inclusions that have reequilibrated and/or refilled. This interpretation is based on the assumption that any primary inclusions in the carbonate that were trapped when it was originally precipitated at depth would have reequilibrated when they were entrained into the hot lamprophyric magma during transport to the near-surface (Bodnar, 2003b).

Homogenization temperatures range from  $77$  to  $204^\circ\text{C}$  (Fig. 5.4a-c) and are consistent with data reported by Demény et al. (1994) on primary fluid inclusions in carbonate ocelli from some TCR lamprophyre dikes. However, our data show a wider temperature range (Fig. 5.4a). Fluid inclusions in Types-I and -II carbonates span the entire temperature range mentioned above (Fig. 5.4a-b) whereas fluid inclusions in Type-III carbonates vary within a narrow range and are never higher than  $104^\circ\text{C}$  (Fig. 5.4c).

First melting occurs at about  $-21^\circ\text{C}$ , near the  $\text{H}_2\text{O}$ - $\text{NaCl}$  eutectic temperature ( $-21.2^\circ\text{C}$ ; Bodnar, 1992). No evidence of gases was observed. Final ice melting temperatures in the three aggregate types overlap and vary between  $-0.2^\circ\text{C}$  and  $-15.0^\circ\text{C}$ , with most between  $-2.4^\circ\text{C}$  and  $-9.6^\circ\text{C}$  (Table 5.2). Based on the observed first melting temperatures the inclusions are modeled using the  $\text{H}_2\text{O}$ - $\text{NaCl}$  system. Salinities of primary fluid inclusions in Types-I and -II aggregates range from  $4.0$  to  $13.6\ \text{NaCl}_{\text{equiv. wt\%}}$  (Bodnar, 1992), ignoring the extreme data (Table 5.2). Final melting temperatures of secondary inclusions in Type-III aggregates average  $-1.8^\circ\text{C}$ , corresponding to an average salinity of  $2.8\ \text{NaCl}_{\text{equiv. wt\%}}$ .

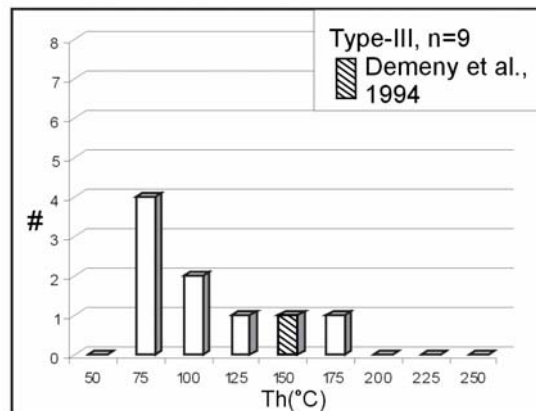
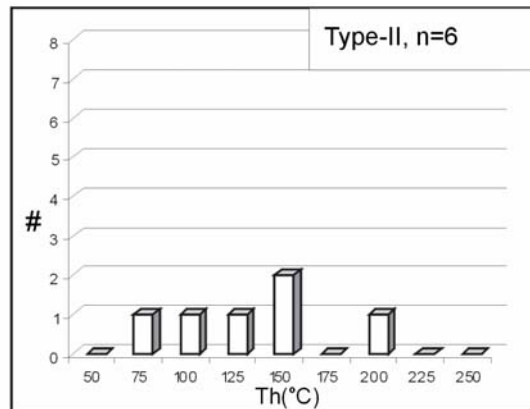
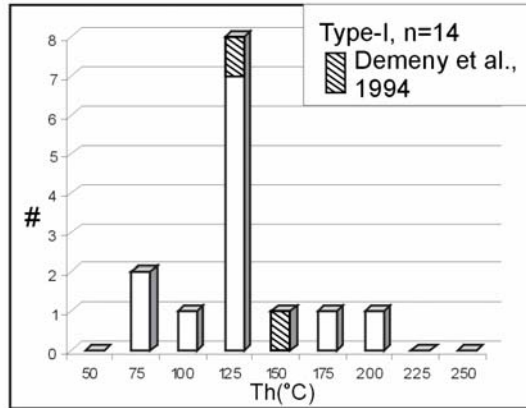


Figure 5.4. Homogenization temperatures of fluid inclusions hosted in carbonate aggregates in TCR lamprophyres sorted according the aggregate type. Data for Type-I and Type-II aggregates include results from Demény et al. (1994)

Table 5.2. Average ice-melting temperatures and salinities of fluid inclusions in carbonate aggregates from the TCR lamprophyres.

Aggregate Type	Sample	Average $T_h$ (°C)	StDev	Average $T_m$ (°C)	Salinity (NaCl <sub>equi</sub> wt%)	StDev
Type-I	St-1/4a	141	2.2	-9.6	13.6	n/a
	St-1/4b	n/a	n/a	-7.3	10.9	n/a
	My-1/1	204	4.3	-3.3	5.4	1.5
	Pa-1/1	102	33.1	n/a	n/a	n/a
	Bkt1/6	130	49.3	-0.2	0.3	n/a
Type-II	St-1/1c	111	22.6	-1.0	1.7	2.6
	St-1/3	128	29.7	-1.0	1.7	4.1
Type-III	St-1/6	106	15.1	n/a	n/a	n/a
	My-1/2	158	36.1	-2.43	4.1	2.6
	Rh-121/3	90	6.9	-0.2	0.3	n/a

$T_h$  Homogenization temperature  
 $StDev$  Standard deviation of measurements  
 $T_m$  Final melting temperature of ice

## V.7. Discussion

### V.7.1. Geothermometry

The formation temperature of carbonates was estimated using the method of Hamilton (1961) for nepheline in equilibrium with carbonates. This method is based on experimentally determined limits of NaAlSiO<sub>4</sub>-KAlSiO<sub>4</sub>-SiO<sub>2</sub>-H<sub>2</sub>O solid-solution in nepheline at temperatures between 500 and 775°C, using the K/Na and Si/Al cation ratios of nepheline in equilibrium with silicate melt (Hamilton and MacKenzie, 1960). Experiments at 1 and 2 kbars show that the effect of pressure on the solid-solution boundary is negligible (Hamilton, 1961). This method was applied to the Type-I aggregates that show textural evidence of coeval crystallization of nepheline and carbonate (Fig. 5.2B). Two analyzed nephelines contain 73.8 and 82.4 mole% nepheline end-member (NaAlSiO<sub>4</sub>), 26.2 and 17.6 mole% kalsilite (KAlSiO<sub>4</sub>), and 1.9 and 3.5 mole% SiO<sub>2</sub>, respectively, and suggest a temperature of formation <500°C. This temperature is assumed to also apply to the contemporaneous carbonate in the aggregates.

### V.7.2. Genesis of the carbonate aggregates

The genesis of Types-II and -III carbonate aggregates can be readily established on the basis of the evidence presented here (Table 5.3). Petrographic and geochemical characteristics of Type-III carbonates support their xenolithic - xenocrystic origin. Their polygonal, irregular shape (Fig. 5.2E-F) is consistent with their origin as fragments from the conduits of the intruding lamprophyre melt. The other distinctive geochemical feature of the Type-III aggregates is that they contain Mg- and Fe-rich carbonate phases at the rims, and Ca-rich carbonate cores (Fig. 5.2E-F).

The geological setting and petrographic and geochemical features of zoned silicate phases (clinopyroxenes, mica) from lamprophyres indicate an extremely rapid cooling rate for the dike rocks (Szabó et al., 1993). According to Fisler and Cygan (1999), distinct carbonate compositional zoning on a scale of 100's of micrometers, such as observed in Type-III carbonate aggregates, is unlikely to be reset by chemical

diffusion during rapid cooling (1000 °C/m.y.) of melts in contact with carbonates. Thus, we can exclude chemical diffusion for the origin of compositional zoning observed in Type-III aggregates (Fig. 5.2E-F). The compositional zonation in Type-III aggregates (Fig. 5.2E-F; Table 5.2) is best explained by reaction between the solid carbonate wall rock and hot lamprophyre melt, resulting in rapid melting and crystallization of the rims of carbonate xenoliths.

The preceding interpretation is consistent with phase equilibria in lamprophyre melts, which have liquidus temperatures  $\approx 1200^{\circ}\text{C}$  at lower crustal conditions (Nemec, 1977; Esperanca and Holloway, 1987). Most lamprophyre melts are almost completely crystallized after cooling to 250 to 450 °C below the liquidus temperature (Nemec 1977; Montel and Weisbrod, 1986). Thus, melts interacting with carbonate (limestone and/or dolomite) wallrocks in the upper crust must have been at least 750°C. Following entrainment of wall rock fragments, lamprophyric melts rise quickly towards the surface (Rock, 1991; Szabó et al., 1993) and cool rapidly, leaving little time for complete assimilation of the larger carbonate aggregates. Thus, only the rims of Type-III aggregates show evidence of interaction with the host melts.

The occurrence of Al-silicates such as those observed at the contact between some Type-III carbonate aggregates and the lamprophyre groundmass (Fig. 5.2F) have been interpreted as the product of partial assimilation of limestone by alkaline and mafic magmas (e.g. Joesten, 1977; Baker and Black, 1980; Joesten et al., 1994; Owens, 2000). The secondary fluid inclusions are likely to represent hydrothermal fluids related to the late-stage crystallization of the lamprophyre, or to fluids infiltrating the dikes after their complete crystallization.

The shape and size of Type-II carbonate is similar to that of unaltered or partially altered olivine phenocrysts in the lamprophyres (Fig. 5.2D) and appears to be metasomatic carbonatization products after olivine phenocrysts. This is consistent with observations of Rock (1991) who described widespread late-stage or subsolidus autometasomatic alteration of primary minerals in lamprophyres due to their high volatile content. However, primary fluid inclusions in Type-II aggregates are at variance with the proposed gradual carbonatization of olivine. The olivine must have been completely

altered and removed to provide space for precipitation of later carbonate phases by hydrothermal fluids, some of which were trapped to produce primary fluid inclusions.

Based on the tectonic and stratigraphic settings of the lamprophyre dike swarms, late stage, secondary process associated with formation of Type-II carbonate aggregates occurred in the upper crust (Kubovics and Szabo, 1988). Thus, the carbonate aggregates are likely to have formed at pressures lower than 5 kbars. Based on the isochores for aqueous (H<sub>2</sub>O-NaCl) fluid inclusions with salinities between 5 and 10 wt% and homogenization temperatures below 200°C (Fig. 5.5, Table 5.2), the formation temperature of these fluid inclusions would have been under 500°C if the pressure was lower than 5 kbars (Fig. 5.5). A notable feature is that Type-II aggregates occur exclusively in the St-1 and Ad-2 lamprophyre sample where the abundance of Type-I aggregates with a similar composition is high (Table 5.1a-b), as well. This suggests that the source of fluids responsible for the genesis of Types-I and -II carbonates might be the same. This is supported by their similar composition (Fig. 5.3., Table 5.1a-b) and by the fact that there is a network of carbonate veins connecting Types-I and -II aggregates (Fig. 5.2G-H).

Petrographic and geochemical features of Type-I aggregates are similar to those of aggregates that have been interpreted to be ocelli (e.g. Phillipotts and Hodgson, 1968; Ferguson and Currie, 1971). However, most of these authors explained the genesis of globular aggregates in alkali mafic rocks as solidified droplets of carbonate melt that separated from a silicate melt. Formation of the carbonate phases in the ocelli of TCR lamprophyres, however, cannot be explained by immiscibility during crystallization of the felsic melt. However, the vugs that now contain carbonate could have been formed during such a process.

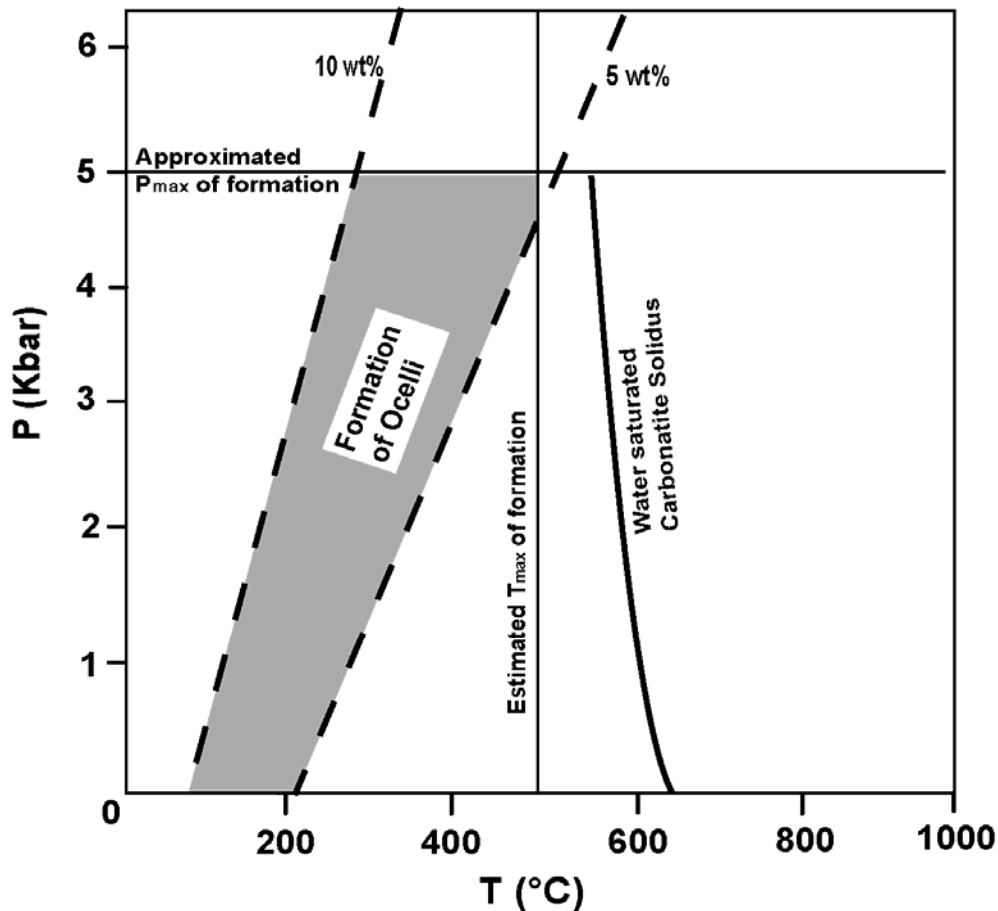


Figure 5.5. Estimates of P-T formation conditions for carbonate aggregates in the TCR lamprophyres. The shaded field shows the pressure – temperature of formation for Type-I carbonate aggregates, defined by the isochores (dashed lines) for lowest and highest measured homogenization temperatures and lowest and highest calculated salinity. The vertical solid line shows the estimated maximum temperature of formation and the horizontal line shows the assumed maximum pressure of formation. The double sub-vertical line shows the water-saturated carbonatite solidus from Boettcher et al. (1980).

Primary fluid inclusions in Types I- and –II aggregates show homogenization temperatures lower than 204°C (Fig. 4). Assuming a formation pressure of <5 kbars for the lamprophyres, the formation temperature of the primary inclusions would have been lower than the water -saturated carbonate solidus (Fig. 5). This conclusion is also supported by the estimated temperature range (lower than 500°C) for the formation of

silicate phases in the ocelli rims that show textural evidence for coeval crystallization with the carbonate phases (Fig. 5.2B). Most likely Type-I ocelli formed by the following process. First, gas bubbles exsolved from the volatile-rich, late stage melts to produce vesicles in the magma after much of the groundmass had crystallized (Foley, 1984; Andronikov and Foley, 2001). The commonly occurring tangential alignment of phlogopites around aggregates (Fig. 5.2C) was caused by expansion of gas bubbles in a partially crystallized magma (Phillips, 1973). External fluids responsible for the precipitation of Type-I carbonate aggregates were transported through the fracture system now preserved as carbonate-filled veins. The important role of externally-derived fluids in the formation of the aggregates is also supported by the mixed magmatic-meteoritic isotopic composition of the carbonate aggregates reported by Demeny et al. (1994).

Based on the petrographic and geochemical characteristics of Type-I carbonates, one cannot exclude the possibility that they represent recrystallized magmatic carbonates. This also implies that the fluid inclusions do not provide information on the formation of the carbonate aggregates, but rather that the inclusions represent fluids that were present during recrystallization. Among the most diagnostic tests recrystallization has occurred is the presence of geochemical patterns that overprint original compositional zoning (Goldstein, 2003). CL and BSE imaging show homogenous cathodoluminescence textures in Type I aggregates. Such textures are usually not associated with recrystallization, but cannot be used to conclusively rule out that recrystallization has occurred.

Results of integrated petrographic, geochemical and fluid inclusion studies suggest that ocelli previously interpreted as products of carbonate-silicate melt immiscibility might be better interpreted as the products of hydrothermal processes.

## V.8. Conclusions

Late Cretaceous lamprophyres from the Transdanubian Central Range (Hungary) contain carbonate aggregates that have been classified into three distinct groups (Table 5.3). *Type-I aggregates* are globular shape, contain primary and secondary aqueous fluid inclusions, lack major element zonation, and show tangentially aligned mica at the contact with the host rock. Based on microthermometric analyses and geothermometric calculations, these aggregates precipitated from aqueous hydrothermal solutions to fill vesicles in the crystallized (or partially crystallized) melt. This observation is inconsistent with previous models that explain the genesis of such features by silicate–carbonate melt immiscibility.

*Type-II carbonate aggregates* also host primary and secondary fluid inclusions but show polygonal shape and lack of oriented sheet silicates at their rims. Type-II aggregates form from hydrothermal fluids, similar to Type-I aggregates, except that the carbonate phases precipitated in spaces previously occupied by olivine phenocrysts.

*Type-III aggregates* have irregular shape, distinct compositional zoning (increasing Mg-, and Fe-content in the carbonate phases towards the rims), contain secondary fluid inclusions, and contain Al-silicates (clay minerals) at the contact with the lamprophyre host, instead of a shell of oriented mica as in the Type-I. These aggregates show signs of reaction with the hot lamprophyric melt and are interpreted to represent xenoliths and xenocrysts from the wall rock of the magma conduits.

Table 5.3. Summary of petrographic, geochemical and microthermometric characteristics of different carbonate aggregate types in the TCR lamprophyres.

Aggregate Type	Petrography	Microthermometry	Carbonate Composition	Proposed Origin	Samples
Type-I	Globular shape, Tangentially oriented mica and amphibole at rim	Primary FIs Th between 77 and 204°C	Dolomite, Calcite, Magnesite	Hydrothermal filling of vesicles or recrystallization of ocelli	Ad-2/III, Bkt1/6, My-1, Pa1, St-1, Val-3
Type-II	Polygonal Shape, Olivine pseudomorphs, No Mica or amphibole rim	Primary FIs Th between 95 and 172°C	Dolomite	Pseudomorphs after olivine	Ad-2/X, St-1
Type-III	Irregular shape, No mica or amphibole rim, Al-silicates at rim	Secondary FIs Th $\leq$ 104°C	Compositional zonation: Calcite, Dolomite, Magnesite, $\pm$ Ankerite	Carbonate xenoliths and xenocrysts	Ad-2/II, Bo1-16, Rh/1012, Rh8, Bkt1/6

## V.9. Acknowledgements

This manuscript has benefited greatly from help of Enikő Bali, Kálmán Török and others at the Lithosphere Fluid Research Laboratory at Eötvös University, Budapest and the Fluids Research Laboratory at Virginia Tech. A. H. Rankin and F. Wall are thanked for their critical comments on an earlier version of this manuscript. Editorial comments of Benedetto De Vivo are also appreciated.

Financial support for this work was provided by TET Hungarian-American Foundation to Csaba Szabó and Robert Bodnar (17/MO/01) and by Pro Renovanda Culturae Hungariae Foundation to Tristan Azbej and by a grant from the U.S. National Science Foundation to R Bodnar (NSF Grant EAR-0125918).

## V.10. References

- Andronikov AV, Foley SF (2001) Trace element and Nd-Sr isotopic composition of ultramafic lamprophyres from the East Antarctic Beaver Lake area. *Chem. Geol.* 175: 291-305.
- Azbej T (2002) Petrographic and geochemical study on carbonates in lamprophyres (in Hungarian). M.Sc. Thesis. Eötvös University, Budapest. 102 pp.
- Azbej T, Szabó Cs, Bodnar RJ, Dobosi G (2003) A new interpretation of the genesis of carbonate aggregates from lamprophyres in Hungary: Are ocelli of magmatic or hydrothermal origin? *Acta Mineral. Petrogr. Abstr. Ser., Szeged. Abstract Series* 2. 12.
- Baker CK, Black PM (1980) Assimilation and metamorphism at a basalt-limestone contact, Tokatoka, New Zealand. *Min. Mag.* 43: 797-807.
- Balog A, Read JF, Haas J (1999) Climate-controlled early Dolomite, late Triassic cyclic platform carbonates, Hungary. *J. Sed. Res.* 69: 1, 267-282.
- Bence AE, Albee AL (1968). Empirical correction factors for the electron microanalysis of silicates and oxides. *J. Geol.* 76: 382-403.

- Bodnar RJ (1992) Revised equation and table for determining the freezing point depression of H<sub>2</sub>O-NaCl solutions. *Geochim. Cosmochim. Acta* 57: 638-684.
- Bodnar RJ (2003a). Introduction to fluid inclusions. In Samson I, Anderson A, Marshall D (eds) *Fluid Inclusions: Analysis and Interpretation*. Mineral. Assoc. Canada, Short Course 32, 1-8.
- Bodnar RJ (2003b) Reequilibration of fluid inclusions. In Samson I, Anderson A, Marshall D (eds) *Fluid Inclusions: Analysis and Interpretation*. Mineral. Assoc. Canada, Short Course 213-230.
- Boettcher AL, Robertson JK, Wyllie PJ (1980) Studies in synthetic carbonatite systems; solidus relationships for CaO-MgO-CO<sub>2</sub>-H<sub>2</sub>O to 40 kbar and CaO-MgO-SiO<sub>2</sub>-CO<sub>2</sub>-H<sub>2</sub>O to 10kbar. *J Geophys. Res.* 85, 12.
- Cooper AF (1979) Petrology of ocellar lamprophyres from western Otago, New Zealand. *J. Petrol.* 20: 139-163.
- Demény A, Fórizs I, Molnár F (1994) Stable isotope and chemical compositions of carbonate ocelli and veins in Mesozoic lamprophyres of Hungary. *Eur. J. Mineral.* 6: 679-690.
- Dunkl I (1989) Application of fission track methods in geochronological methods (in Hungarian). Ph.D. Thesis, Eötvös University, Budapest. 178 pp.
- Embey-Isztin A, Dobosi G, Noske-Fazekas G, Árvai-Sós E (1989) Petrology of a new basalt occurrence in Hungary. *Mineral. Petrol.* 40: 183-196.
- Esperanca S, Holloway JR (1987) On the origin of some mica-lamprophyres; experimental evidence from a mafic minette. *Contrib. Mineral. Petrol.* 95: 207-216.
- Ferguson J, Currie KL (1971) Evidence of liquid immiscibility in alkaline ultrabasic dikes at Callender Bay, Ontario. *J. Petrol.* 12: 561-585.
- Fisler DK, Cygan RT (1999) Diffusion of Ca and Mg in calcite. *Am. Min.* 84: 1392-1399.
- Foley SF (1984) Liquid immiscibility and melt segregation in alkaline lamprophyres from Labrador. *Lithos* 17: 17-137.
- Gittins J (1979) Problems inherent in the application of calcite-dolomite geothermometry to carbonatites. *Contrib. Miner. Petrol.* 6: 1-4.

- Goldstein RH, Reynolds TJ (1994) Systematics of fluid inclusions in diagenetic minerals. SEPM Short Course 31, 199 pp.
- Hamilton DL (1961) Nephelines as crystallization temperature indicators. *J. Geol.* 69, 321-329.
- Hamilton DL, MacKenzie WS (1960) Nepheline solid solution in the system  $\text{NaAlSiO}_4\text{-KAlSiO}_4\text{-SiO}_2\text{-H}_2\text{O}$ . *Jour. Petrology.* 1: 56-72.
- Hamilton DL, Freenstone IC, Dawson JB, Donaldson CH (1979) Origin of carbonatites by liquid immiscibility. *Nature* 279: 52-54.
- Horváth I, Ódor L (1984) Alkaline ultrabasic rocks and associated silicocarbonatites in the NE part of the Transdanubian Mts. (Hungary). *Miner. Slov.* 16: 115-119.
- Horváth I, Daridáné TM, Ódor L (1983) Magnesite bearing dolomitic carbonatite dike rocks from the Velence Mountains (in Hungarian). *Magy. Áll. Földt. Int. Évi Jel.* 1981-ről, 41-44.
- Joesten R (1977) Mineralogical and chemical evolution of contaminated igneous rocks at a gabbro-limestone contact, Christmas Mountains, Big Bend region, Texas. *Geol. Soc. Amer. Bull.* 88: 1515–1529.
- Joesten R, Hill J, Van-Horn SR (1994) Limestone assimilation and clinopyroxene production along the contacts of a 9 meter alkali olivine basalt dike, Killala Bay, Ireland. *Geol. Soc. Am. Abstracts with Programs.* 26. 476.
- Kázmér M, Szabó Cs (1989) Late Cretaceous lamprophyre dikes in the hinterland of the Alpine deformation front. EUG-V, Strasbourg, Terra abstract, 177.
- Kubovics I, Szabó Cs (1988) Geochemical, Petrologic and Mineralogical study on alkali mafic and ultramafic dike rocks from Alesutdoboz-2 drill hole (in Hungarian). *Magy. Áll. Földt. Int. Évk.* LXV, 335-356.
- Kubovics I, Gál-Sólymos K, Szabó Cs (1985) Petrology and geochemistry of ultramafic xenoliths in mafic rocks of Hungary and Burgenland (Austria). *Geol. Carpathica* 36: 433-450.
- Kubovics I, Szabó Cs, Gál-Sólymos K (1989) A new occurrence of lamprophyre in the Buda Mountains, Hungary. *Acta Geol. Hung.* 32: 149-168.

- Kubovics I, Szabó Cs, Harangi Sz, Józsa S (1990) Petrology and petrochemistry of Mesozoic magmatic suites in Hungary and the adjacent areas - an overview. *Acta Geodaet. Geophys. Mont. Hung.* 25: 345-371.
- Lucchini F, Simboli G, Zenatti A, Barbieri M, Nicoletti M, Petrucciani C (1983) Petrochimica a dati radiometrici K/Ar e Rb/Sr dei filoni basici di Corvara in Badia e dei lamprofiri di Val Fiscalina (Dolomiti Orientali). Revisione classificativa ed implicazioni genetiche nel quadro del magmatismo filoniano delle Alpi (in Italian). *Miner. Petrog. Acta.* 27: 233-249.
- Montel JM, Weisbrod A (1986) Characteristics and evolution of "vaugneritic magmas"; an analytical and experimental approach, on the example of the Cevennes Medianes (French Massif Central). *Bulletin de Mineralogie* 109: 575-587.
- Nédli Zs, Tóth T (2003) Petrography and mineral chemistry of rhönite in ocelli of alkali basalt from Villány Mts., SW-Hungary. *Acta Miner.-Petrogr.* 44: 51-56.
- Nemec D (1977) Differentiation of lamprophyre magma. *Krystalinikum* 13: 73-87.
- Owens BE (2000) High-temperature contact metamorphism of calc-silicate xenoliths in the Kiglapait Intrusion, Labrador. *Am. Min.* 85: 1595-1605.
- Phillips WJ (1973) Interpretation of crystalline spheroidal structures in igneous rocks. *Lithos* 6: 235-244.
- Philpotts AR (1990) Principles of igneous and metamorphic petrology. Prentice Hall. 498 pp.
- Philpotts AR, Hodgson CJ (1968) Role of liquid immiscibility in alkaline rock genesis. XXIII. *Inter. Geol. Congr.* 2, 175-188.
- Rock NMS (1991) Lamprophyres. Blackie and Son, Glasgow-London-New York, 285 pp.
- Slavkay M (1979) Dalsie vyskyty ultrabázických efuzív v chocskom a kríznanskom príkore pri Banskej Bystirici (in Slovakian). *Mineral. Slov.* 11: 239-245.
- Szabó Cs (1985) Xenoliths from Cretaceous lamprophyre of Alcsútdoboz-2. borehole, Transdanubian Central Mountains, Hungary. *Acta Miner.-Petrogr.* 27: 39-50.
- Szabó Cs, Kubovics I, Molnár Zs (1993) Alkaline lamprophyre and related dike rocks in NE Transdanubia, Hungary: The Alcsútdoboz-2 (AD-2) borehole. *Miner. Petrol.* 47: 127-148.

Vichi G, Stoppa F, Wall F (2005) The carbonate fraction in carbonatitic Italian lamprophyres. *Lithos.* 85: 1-4, 154-170.